



HAL
open science

Textural-based methods for image superresolution : Application to Satellite-derived Sea Surface Temperature imagery

Brahim Boussidi

► **To cite this version:**

Brahim Boussidi. Textural-based methods for image superresolution : Application to Satellite-derived Sea Surface Temperature imagery. Image Processing [eess.IV]. Ecole Nationale Supérieure des Télécommunications de Bretagne - ENSTB, 2016. English. NNT : 2016TELB0404 . tel-01593247

HAL Id: tel-01593247

<https://theses.hal.science/tel-01593247>

Submitted on 26 Sep 2017

HAL is a multi-disciplinary open access archive for the deposit and dissemination of scientific research documents, whether they are published or not. The documents may come from teaching and research institutions in France or abroad, or from public or private research centers.

L'archive ouverte pluridisciplinaire **HAL**, est destinée au dépôt et à la diffusion de documents scientifiques de niveau recherche, publiés ou non, émanant des établissements d'enseignement et de recherche français ou étrangers, des laboratoires publics ou privés.

UNIVERSITE BRETAGNE LOIRE

THÈSE / Télécom Bretagne
sous le sceau de l'Université Bretagne Loire
pour obtenir le grade de Docteur de Télécom Bretagne

En accréditation conjointe avec l'Ecole Doctorale Sicma
Mention : Sciences et Technologies de l'Information et de la Communication

présentée par

Brahim Boussidi

préparée dans le département Signal et Communications
Laboratoire Labsticc

Textural-based methods for image super-resolution: Application to Satellite-derived Sea Surface Temperature imagery

Thèse soutenue le 18 octobre 2016
Devant le jury composé de :

Xavier Carton
Professeur, Université de Bretagne Occidentale / président

Yannick Berthoumieu
Professeur, IMS - Enseirb-Matmeca - Bordeaux / rapporteur

Yann Gousseau
Professeur, Télécom ParisTech / rapporteur

Peter Cornillon
Professeur, University of Rhode Island / examinateur

Bertrand Chapron
Chercheur, Ifremer - Plouzané / examinateur

Ronan Fablet
Professeur, Télécom Bretagne / directeur de thèse

Hervé Roquet
Ingénieur, Météo France-CMS - Lannion / invité

Sous le sceau de l'Université Bretagne Loire

Télécom Bretagne

En accréditation conjointe avec l'Ecole Doctorale Sicma

Textural-based methods for image superresolution: Application to Satellite-derived Sea Surface Temperature imagery

Thèse de Doctorat

Mention : Sciences et Technologies de l'information et de la Communication

Présentée par: M. Brahim BOUSSIDI

Département: Signal et Communications

Laboratoire: Lab-STICC Pôle: CID /TOMS

Directeur de thèse: M. Ronan Fablet

Soutenue le 18 Octobre 2016

Jury :

M. Yann Gousseau	Professeur	Télécom ParisTech	(Rapporteur)
M. Yannick Berthoumieu	Professeur	IMS Université de Bordeaux	(Rapporteur)
M. Ronan Fablet	Professeur	IMT Atlantique	(Directeur de thèse)
M. Xavier Carton	Professeur	Université de Bretagne Occidentale	(Examineur)
M. Peter Cornillon	Professeur	University of Rhode Island (USA)	(Examineur)
M. Bertrand Chapron	Chercheur	Ifremer	(Examineur)
M. Hervé Rouquet	Ingénieur	Météo France	(invité)

Remerciements

Je remercie en premier lieu mon directeur de thèse Ronan Fablet pour son soutien et son enthousiasme au cours de cette thèse.

Mes remerciements vont également à l'ensemble des membres du jury, le président Xavier Carton, les rapporteurs Yann Gousseau, Yannick Berthoumieu et les examinateurs Peter Cornillon et Hervé Roquet.

Merci bien sûr à Bertrand Chapron pour son enthousiasme, ses conseils et ses encouragements.

Je remercie également Pierre Tandeo, Clément le Goff et Sileye Ba pour les divers échanges et discussions.

Je tiens tout particulièrement à remercier Samir Saoudi, le chef du département Signal et communications de Télécom Bretagne, ainsi que l'ensemble du personnel du département.

Merci aux amis et copains rencontrés à Télécom Bretagne tout au long de cette thèse.

Je remercie enfin ma famille pour son soutien et sa patience durant ces années. Merci à mes parents, mes deux soeurs Aicha et Fatima et mon frère Moustapha.

List of Figures

1.1	Probability of occurrences of clear-sky pixels during 2004 in (a) Modis L3 data (b) AMSR-E	19
1.2	Example of satellite-derived SST snapshots acquired by MODIS ((a) and (c)) and AMSR-E ((b) and (d)) on Aqua platform in the Malvinas region. The snapshots of the first row were acquired on Aug. 25, 2010 and depict a cloud-free scenario. By contrast, the snapshots second row images were acquired 3 days later under a heavily cloudy conditions.	20
1.3	(a) The sparsity structure of the matrices involved in the inference and the synthesis of textures using the SPDE and equivalent approaches comparing with (b) the dense matrices using the classical covariance-based method. Even using the covariance tapering [1] to approximate the likelihood (1.2), the resulting matrices are relatively less sparse than (a).	23
1.4	Illustration of the Exemplar-based super-resolution as considered in this thesis.	24
2.1	Spot noise associated with the Gaussian kernel with different values of n . A stationary texture is obtained as n increase.	31
2.2	Differences between the outcomes of the RPN and the ADSN associated with a Gaussian spot (a). (b) RPN outcome and (c) ADSN simulation. The Fourier modulus of the various simulations are represented in (d) and (e) and. Let us point out that the modulus of the ADSN is the pointwise multiplication of the modulus of RPN by a white Rayleigh noise.	34
2.3	Example of correlated texture-like satellite images provided by the multispectral LANDSAT 7 ETM sensor and sampled respectively with channels 2,3,4 (first row). The outcome of the trivariate RPN algorithm is displayed in the second row. Independent simulations using the univariate RPN model of the three image are shown in the third row. The trivariate model aims at reproducing the autocorrelations and cross correlations of the three texture samples.	39
2.4	Comparison between the autocorrelation and cross-correlations obtained from (a) the input texture sample, (b) from the trivariate RPN outcome and (c) from images depicted in (Fig.2.3 third row).	39
2.5	Example of the outcome of the trivariate ADSN algorithm. The input images (first row) are texture-like satellite snapshots provided by LANDSAT 8 and taken respectively from channels 1,2 and 5.	41

2.6	Demonstration of the capability of the trivariate ADSN model to produce the correlation and cross correlation of the sample vector images. (a) sample-based kernels (b) Outcomes of the MASN algorithm.	42
2.7	Difference between the MRPN and MADSN processes. The Fourier modulus of the first component of the vector image simulated using (a) the MRPN and (b) MADSN algorithm. The modulus of the MADSN is the pointwise multiplication of the modulus of MRPN by (c) a white Rayleigh noise.	43
2.8	(a) Isotropic Matérn covariance function obtained from model (2.59), (b) Realizations of random field with the covariance function shown in (a)	45
2.9	Anisotropic Matérn covariance function obtained by applying the transformation (2.63) to the covariance function shown in Fig.2.8(a) with $R = 1/2$ and $\theta = \pi/4$, (b) A realization of random field with the given covariance function.	46
2.10	Texture synthesis using non-stationary SPDEs for different geometrical patterns: (a) rotational and (b) hyperbolic orientation field using a constant parameters for α , κ , σ and R . The texture in (c) is obtained by (smoothly) jointly varying κ and σ parameters of an isotropic covariance model.	48
3.1	Example of texture synthesis by phase randomization [2]. (a) The original sample (b) synthesized texture using the RPN algorithm	51
3.2	Failure example of texture synthesis by phase randomization. (a) The original texture (b) synthesized using the RPN algorithm	52
3.3	Super-resolution of canvas texture: (a) Original image (ground truth). (b) LR image. (c) Bicubic interpolated result. (d) Super-resolution enhanced image obtained using the cascade model with phase randomization. (e) Result obtained without considering cascading. (f) Super-resolution image obtained using phase constraints.	54
3.4	Quantitative comparison of results obtained in Fig.3.3. (a) The probability density functions of the marginal cross-scale component of the generated images compared with the ground truth. (b) The spectra of cross-scale components (coarser-to-fine scale).	55
3.5	The same as Fig.3.3 for the stone texture.	55
3.6	The same as Fig.3.4 for the stone texture example.	56
3.7	Super-resolution of tree bark texture: the first row depicts the ground truth image and the blurred versions using various box filters of size $2^n \times 2^n$ with n ranging from 1 to 3 (from left to right). The super-resolution results are illustrated in the second row for various enlargement factors ranging from $\times 2$ to $\times 8$ (from right to left).	56
3.8	Outcome of the RPN algorithm	57
3.9	The same as Fig.3.4 for the example depicted in Fig.3.7	57

4.1	Upper panel: Brightness temperature snapshot provided by the infrared TIRS sensor on board Landsat8. Lower panel: The power spectral density of the selected study area.	64
4.2	Illustration of the Schramm-Loewner evolution idea. The conformal mapping g_t , which satisfies Loewner's equation, maps the upper half plane without the curve up to time t , $H \setminus \gamma([0, t])$, onto the whole upper half plane.	65
4.3	Illustration of the an iteration of the slit map algorithm. The portion of the curve between z_0 and z_1 is approximated by a vertical slit (red segment). The algorithm consists of transforming the vertical slit to the abscissa axis. This elementary transformation is iterated for the whole curve.	66
4.4	SLE-based characterization of the level lines of a Gaussian Gaussian Free Field: (a) realization of the 2D Gaussian Free Field simulated using the spectral method [3] (b) A selected level line of from the simulated snapshot, theoretically proven to resort a realization of a SLE(4) process ($\kappa = 4$) (c) Statistics of the extracted driving functions: variance of the driving functions as a function of the Loewner time. The diffusion coefficient κ is given by the slope of this curve. .	67
4.5	Statistics and the diffusive behavior of the extracted driving functions from an ensemble of BT level lines. (a) The variance of ξ_t against the Loewner time. (b) The probability density of ξ_t for $t = 10^4, 4 \times 10^4$.	68
4.6	The gradient magnitude field of the selected study region with the two selected level lines	69
4.7	Results of the SLE-based analysis of the two selected level lines in Fig.4.6. (a) Level lines transformed to the upper half plane and starting from the origin. Inset: the distribution of the along level line BT gradient magnitude. (b) Driving functions corresponding to the considered level lines. (c) Power spectral density of the extracted forcing function. Inset: The probability density of the driving increments rescaled by its variance. (d) The auto-correlation functions of the driving increments with an approximation of the confidence bounds using the Box-Jenkins-Reinsel approach.	70
4.8	Illustration of the gradient-based regime-switching behavior of the driving function. (a) The BT gradient magnitude extracted and segmented from a typical long BT level line. (b) The extracted driving force as function of Loewner time. (c) The moving-window variance of the driving function increments. The variance shows clear dependence on the local gradient magnitude. It increases to reach values between 1.5 and 3 for the low gradient intensities (The two first shaded bar). Conversely, it decreases to zero for large gradients as a result of the existence of a long almost 1D segments.	71

4.9	(a) Spectral analysis of driving functions extracted from a large ensemble of gradient-based homogeneous portions of BT level lines. (b) The distribution of the empirical fitted spectral slopes. The fitting is done using the normalized spectra in the wavelength bandwidth determined by the blue segment.	72
5.1	Destriping of an ocean brightness temperature snapshot obtained by TIRS Landsat 8 on September 11, 2014. The original data are shown in panel (a) while the destriped data are shown in panels (b), (d), (e) and (f) using respectively our method, [4] with Haar wavelet, [4] with Daubechies-4 and using a variational approach proposed by [5].	77
5.2	The Haar filter. (a) Scaling function (low-pass filter) and (b) Wavelet function (High-pass filter)	79
5.3	(a) A simulated perfect vertical Gaussian striped sheet. (b) The associated 2D power spectrum. All non-zero values are located near the high frequency part in the horizontal direction (c) The inverted Gaussian function considered as the Fourier filter in our algorithm	80
5.4	Illustration of the destriping of ocean color products: (a) chlorophyll-a concentration obtained by Modis Terra on December 22, 2015 around 06:20 UCT in the Arabian sea region. The destriped data are shown in panel (b). The gradient magnitude of the original image and the destriped image are shown respectively in panel (d) and (e). Comparison of the averaged Fourier power spectrum is illustrated in panel (f).	82
5.5	Illustration of the Destriping of ocean color products: (a) chlorophyll-a concentration obtained by Modis Terra on December 22, 2015 around 06:20 UCT in the Arabian sea region. The destriped data are shown in panel (b). The gradient magnitude of the original image and the destriped image are shown respectively in panel (d) and (e). Comparison of the averaged Fourier power spectrum is illustrated in panel (f).	83
5.6	Destriping results an ocean brightness temperature snapshot using different values of the variance related to the Fourier filter g_α (Eq.5.3) and for different wavelet decomposition levels.	85
5.7	Destriping results of the image shown in Fig.5.1(a) using different method for filling the missing areas before destriping; (a) zero-padding; (b) harmonic inpainting (c) biharmonic inpainting.	86
5.8	(a) Original brightness temperature image from TIRS Landsat 8. (b) Destriped image using our method. (c) The removed residual component. (d) Destriped image with [4] using Haar function. (e) [4] using db4. (f) Destriped image with [5]	87

5.9	The method noise of the original image shown in Fig 5.8 associated to (a) Our method (b) [5]. Panel (c) and (d) report respectively the Fourier power spectrum of (a) and (b). The averaged Fourier power spectrum of the obtained results in Fig 5.8 are plotted in (e), the legend inside refers to Fig.5.8	88
5.10	Mean cross-track profiles of the original and destriped images shown in (a) Fig.5.5 compared with the state-of-the-art algorithms.	88
5.11	Illustration of the impact of the striping noise in the detection of thermal fronts from SST snapshots. The magnitude gradient field of a Modis snapshot computed using the Sobel operator using (a) the full image resolution (b) downsampled version at 4km (c) destriped image at the full sensor resolution (d) the destriped image at 4km resolution.	89
5.12	Illustration of the destriped results for SST snapshots derived from Aqua Modis sensor.(a) Original images (b) Destriped images with the proposed algorithm. (c) Gradient magnitude of the original fields. (d) Gradient magnitude of the Destriped images	91
5.13	Illustration of the potential use of the proposed destriping algorithm. The destriped VIIRS SST data are used along with the I-Band BT at 375 m to produce SST product at 375 m.	92
5.14	Power spectral density (PSD) plots for SST snapshots in Fig 5.6. The frequency components related to the periodic stripes in VIIRS 750 m (Black curves) are extremely attenuated. The graphs have been artificially translated for sake of clarity	93
6.1	Spatial locations of collected SST snapshots in the Malvinas region considered as the area of study	98
6.2	Fourier and Wavelet characterization of SST data (a) Snapshot of MODIS SST in the Malvinas region (b) AMSR-E snapshot (c) degraded version of the Modis snapshot to AMSR-E resolution (d) The associated averaged Fourier power spectra (e) Probability density function (PDF) of the horizontal subbands (details) coefficients of the first, second and third levels of the wavelet decomposition of image (a).	99
6.3	Modis SST snapshot (a) and the corresponding Wavelet decomposition at level 4 using db4.	100
6.4	Statistical analysis of a 2D turbulent flow field: (a) example of two-dimensional turbulent flow field (b) Synthesized Gaussian image obtained by imposing the spectrum of (a). Comparison of the power spectra. (inset) Comparison of the PDFs.	101

6.5	Demonstration of the importance of the phase information in the SST images: (a) original SST snapshot provided by Aqua Modis sensor captured on 29-Apr-2010 (b) synthesized image obtained using the inverse Fourier transform by keeping only the phase information (c) image reconstructed by imposing a constant Fourier phase using the same Fourier magnitudes as the original. (d) image obtained by the random phase noise process (RPN) (e) image obtained by using only the phase information from the original image while the magnitude is learned and imposed from another clear-sky SST snapshot captured on 02-May-2010. Remark that the edge information still present in (b) and a realistic image is obtained in (e)	102
6.6	Power Fourier spectra of images reported in Fig.6.3	103
6.7	Autocorrelation function associated to the inter-scale component of Fig.6.2(a)	103
6.8	(a) The lowpass and highpass analysis filters associated to Symlet wavelet (Sym4), also known as Daubechies least asymmetric wavelets. In order to illustrate the difference with the classical Fourier analysis, a simple sine wave is shown in (b).	104
6.9	Illustration of the effect of the pointwise multiplication of the Fourier modulus by a Rayleigh noise. The SST image (top) is corrupt whereas the associated wavelet sub-bands (bottom) are visually robust to this multiplication. Here, we illustrate this effect using the vertical wavelet sub-band at the level 2.	106
6.10	Snapshots of the sea-surface temperature (SST) anomaly in a $250km \times 250km$ subregion of the Equatorial Pacific. (a) The low-resolution observation, (b) truly observed high-resolution snapshot and (c) the reconstructed image. The second row depicts respectively the gradient magnitude field of the three images.	109
6.11	zooms into subareas of the image considered in Fig.6.10. (a) Low-resolution patches, (b) true High resolution observations and (d) reconstructed patches.	110
6.12	Quantitative results showing the Effectiveness of the proposed method. (a) Fourier power spectra. (b) Marginal PDF of the magnitude of SST gradient fields illustrated in Fig.6.10 (second row). (d) Marginal PDF of the inter-scale components.	111
6.13	(First row) The three 'ground truth' detail subbands at Level 3 (horizontal, vertical, and diagonal, respectively). (b) The reconstructed detail subbands (Second row).	112
6.14	The same as Fig.6.13 for level 1.	112
6.15	The spectra (first row) and the cross-spectra (second row) of the detail subbands at Level 1 for the original SST snapshot (black) and the reconstructed field (red).	113
6.16	The same as Fig.6.15 for the Level 3.	113

6.17	Synthesis result when dropping the cross-spectral constraints. (a) The low-resolution image, (b) the original high resolution image, (c) the constructed image using our approach and (c) the image synthesized by an independent simulation of the model (6.8) for each sub-band. (e) to (g) represent, respectively, the inter-scale component for the tree images in the middle.	116
6.18	Application of our super-resolution scheme on a low-resolution satellite-based image: (a) low-resolution image and (b) the associated magnitude gradient field. Second row shows, respectively, the original high resolution image provided by Modis sensor along with the magnitude of its gradient field and the associated inter-scale component. In the same order, the third row reports the result obtained using our method. Results obtained with the uncorrelated stationary Gaussian model for the wavelet sub-bands without imposing the phase constraint is shown in the fourth row.	117
6.19	Zoomed-in comparisons of the results obtained in 6.18 (a) LR patch, (b) original high resolution patch, (c) proposed model (d) model with no cross-spectral and phase constraints (Fig.6.18(i))	118
6.20	Averaged Fourier power spectra estimated from images in 6.18 and from corresponding super resolved versions for various enlargement factors ranging from $\times 2$ to $\times 16$	119
6.21	Two different line transects of images in 6.18. For interpretation of the references to color in this figure caption, the reader is referred to 6.20	119

Acronyms

AMSR-E	Advanced Microwave Scanning Radiometer - Earth Observing System
AMSR2	Advanced Microwave Scanning Radiometer
AVHRR	Advanced Very High Resolution Radiometer
CWT	Complex Wavelet Transform
DWT	Discrete Wavelet Transform
ESA	European Space Agency
FFT	Fast Fourier Transform
JAXA	Japan Aerospace Exploration Agency
MODIS	Moderate-Resolution Imaging Spectroradiometer
NASA	National Aeronautics and Space Administration
NOAA	National Oceanic and Atmospheric Administration
PDF	Probability Density Function
RSS	Remote Sensing System
SLE	Schramm (Stochastic) Loewner evolution
SPDE	Stochastic Partial Differential Equation
SST	Sea Surface Temperature
SWT	Stationary Wavelet Transform
UWT	Undecimated Wavelet Transform
VIIRS	Visible Infrared Imaging Radiometer Suite

Notations

 $\vec{x} = (x_1, x_2)$ t ∂_x $\vec{\nabla} = (\partial_x, \partial_y)$ $\Delta = (\partial_x^2 + \partial_y^2)$ $\|\cdot\|$ \mathcal{W} \mathcal{F} \mathcal{F}^{-1} \mathcal{Cov} \mathcal{S}

Spatial location

Time variable

Partial derivative in x direction

Gradient operator

Laplacian operator

Norme

Gaussian White Noise

Direct Fourier transform

Inverse Fourier transform

Covariance function

Fourier Spectrum

Contents

List of Figures	ii
Résumé en Français	3
1 Introduction and Context	17
1.1 Considered SST data and related issues	18
1.2 Sample-based texture analysis and synthesis	21
1.3 The use of systems of texture-based models as a priors in image super-resolution	23
1.4 Outline of the thesis	24
1.5 Publications	25
I Stochastic partial differential equations (SPDE) and Texture synthesis	27
2 Texture synthesis using univariate and multivariate sample-based stochastic models.	29
2.1 Introduction	29
2.1.1 The texture synthesis problem	29
2.1.2 Previous work (Parametric and non-parametric approaches)	30
2.1.3 Contribution of the Chapter	31
2.2 Shot (Spot) noise model	31
2.3 ADSN	32
2.4 Random phase noise model (RPN)	33
2.5 Multivariate extension	35
2.5.1 Multivariate RPN	35
2.5.2 Multivariate ADSN	38
2.5.3 Differences between the MRPN and MADSN	42
2.6 Parametric representations and associated SPDE-based formulations	42
2.7 Conclusion	47
3 Superresolution of Textured images using stochastic models and a Novel Fourier domain constraint Phase	49
3.1 Introduction	50
3.2 Fourier magnitude and phase in stochastic textured images	51
3.3 Exemplar-based Super-resolution algorithm	51
3.3.1 Problem formulation	51
3.3.2 A model for textured image	52
3.3.3 Superresolution procedure	53
3.4 Illustrations	54

3.5	Concluding discussion	58
II	Application to reconstruction of high resolved textured images from remote sensing observations	59
4	SST-derived geometrical characterization of ocean surface dynamics using Schramm-Loewner Evolution	61
4.1	Introduction	61
4.2	Materials and Methods	63
4.2.1	Sea surface temperature Data	63
4.2.2	Schramm-Loewner Evolution and geometrical features of turbulent processes	63
4.2.3	SLE-based analysis of SST level-lines	66
4.3	Results	68
4.4	Discussion	71
5	Removing Striping Noise from Cloudy Level 2 Sea Surface Temperature and Ocean Color Datasets	75
5.1	Introduction	75
5.2	Problem statement	76
5.3	Proposed destriping approach: THE UWT-Fourier based destriping scheme	78
5.4	Experimental Results	81
5.5	Conclusion	90
6	Superresolution of low-resolution satellite SST images using phase-constrained and cascaded multivariate Gaussian models	95
6.1	Introduction	95
6.2	SST data and Elementary statistics	97
6.2.1	Wavelet Decomposition and Marginal Statistics	98
6.2.2	Joint Statistics of the Wavelet Coefficients: inter-scale and across-scale Dependencies	100
6.3	Multivariate texture-based models for the Wavelet Coefficients of SST images	104
6.3.1	Cascaded Gaussian random field models on Wavelet Trees	105
6.4	Super-resolution model	107
6.5	Numerical resolution	108
6.6	Results and Discussion	108
6.7	Conclusion	115
7	Conclusion and discussion	121
	Bibliography	125

Résumé en Français

La caractérisation des dynamiques de sous-mésoéchelle (<10km) à la surface de l'océan et leurs impacts sur les processus océaniques globales sont des enjeux scientifiques majeurs. L'utilisation des données d'observation "directes", recueillies in situ, pose des difficultés et des limitations multiples pour aborder ce type de problématique. Les principales difficultés sont liées notamment à la couverture spatiale très peu dense des dites données. L'observation des océans repose désormais sur l'utilisation d'une multitude d'outils. Depuis une vingtaine d'années, des mesures de caractéristiques physiques de la surface des océans sont disponibles à partir d'instruments embarqués sur des satellites. Ces satellites sont soit défilants soit stationnaires. Avec des échantillonnages spatiaux et temporels différents, des techniques de mesures parfois différentes, l'ensemble de ces observations est devenu essentiel pour la description de la dynamique océanique. Le développement de ces instruments a été accompagné par des avancées importantes des algorithmes de traitement des données collectées.

Dans le cas des observations de la température de surface (SST), les capteurs infrarouges fournissent des observations de haute-résolution (~1-10km) mais sont généralement associées à un taux très élevé de données manquantes du fait de la présence des nuages. À l'inverse, les capteurs micro-ondes sont peu sensibles à la présence des nuages mais représentent des résolutions spatiales très faibles (~25-50 km). À titre d'exemple, les figures 1(a-b) et 1(c-d) comparent des observations de SST acquises simultanément par un capteur infrarouge et micro-onde dans la région du Gulf-Stream le 31 Octobre et 07 Novembre 2006 respectivement. Dans cet exemple, les images haute-résolution (~1km) ont été acquises par MODIS et les images basse-résolution (~50km) par AMSR-E. Notons que ces deux capteurs sont embarqués sur la plateforme AQUA. On remarque clairement dans la deuxième situation (Fig.1c), un taux très élevé de données manquantes dans l'image acquise par MODIS à cause de la couverture nuageuse.

Toutefois, l'imagerie satellitaire haute-résolution de la température de surface de l'océan (SST) mettent en évidence de nombreuses structures dites de petites échelles de 1-100 km à la surface de l'océan : tourbillons, filaments, méandres, fronts (Fig.2).

L'utilisation de ces données est devenue cruciale pour la compréhension et la caractérisation des dynamiques de l'océan aux petites échelles, dynamiques qui jouent un rôle primordial dans la compréhension des dynamiques globales et également du forçage opéré par les dynamiques physiques sur les dynamiques biochimiques et écologiques des systèmes marins. La capacité à tirer pleinement partie des différentes modalités d'observation disponibles pour produire des champs d'observation haute-résolution constitue un enjeu majeur, mais reste un problème ouvert. Les principales limitations sont: 1) la présence d'artefacts d'acquisition dans les données de SST haute-résolution et 2) la capacité de reconstruction à partir de données partiellement observées. Dans ce contexte générale, nous proposons 4 contributions

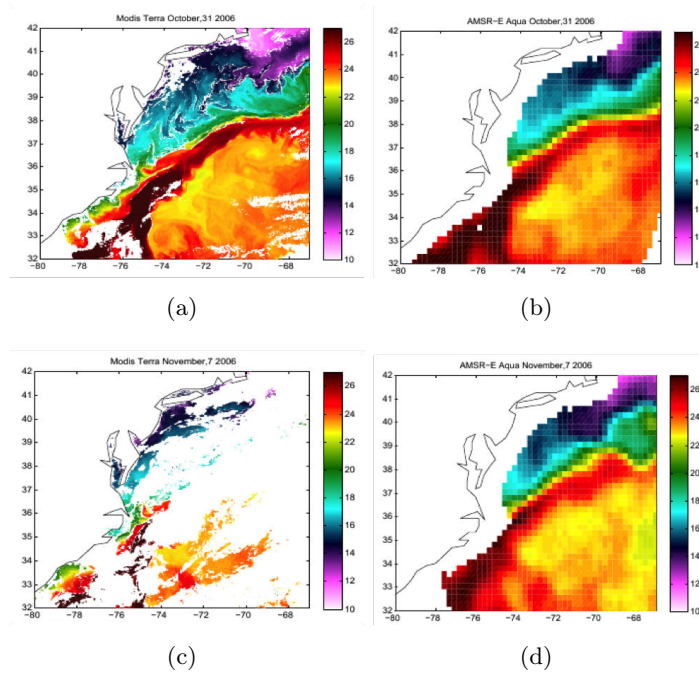


Figure 1: Comparaison de données SST haute et basse résolution pour la zone Gulf Stream (a)-(c) MODIS, (b)-(d) AMSR-E

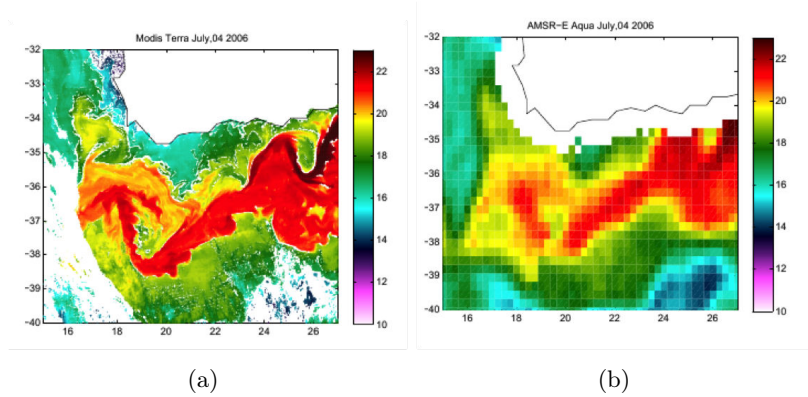


Figure 2: SST MODIS (a) et AMSR-E (b) pour la zone du courant des Aiguilles .

principales: 1) le prétraitement d'artéfacts géométriques dans les observations satellitaires haute-résolution de SST par une approche conjointe Fourier-Ondelette, (2) la modélisation stochastiques des variabilités inter-échelles de champs 2D de SST, (3) la super-résolution stochastique appliquées aux images de SST et (4) la caractérisation de la variabilité géométrique dans les observations satellitaires de SST par des processus de type marche aléatoire.

Dans ce qui suit, nous présentons une synthèse des contributions majeurs de cette thèse. Ce résumé est organisé comme suit. La première section présente l'algorithme développé pour le destriping d'images satellitaires haute-résolution. Dans la deuxième section, nous présentons la méthode proposée pour la reconstruction stochastique de champs de SST haute-résolution à partir d'images basse-résolution. Une caractérisation spatiale de ces observations est proposée dans la dernière section à travers une analyse des lignes de niveaux de champs de SST haute-résolution en utilisant des processus SLE.

Algorithme de filtrage pour le destriping d'images satellitaires

Les satellites d'observation infrarouge de la surface de l'océan font l'acquisition d'images par l'intermédiaire de barrettes de détecteurs, formant une ligne de l'image; l'avancement du satellite dans une direction orthogonale à ces barrettes permettent à chaque détecteur de former une colonne de l'image. En pratique, les détecteurs possèdent certains défauts, ce qui peut produire sur l'image un effet de rayures (stripes). Ces artefacts sont visibles sur les images de température (SST) et nécessitent un prétraitement spécifique avant de pouvoir utiliser les images pour des fins scientifiques ou opérationnels. Beaucoup de travaux ont été menés pour proposer des algorithmes de filtrage efficaces permettant d'éliminer ce type d'artefacts. Ces méthodes exploitent des a priori sur la régularité géométrique du bruit à éliminer. On peut notamment citer les méthodes qui se basent sur l'utilisation de filtres passe-bas. Ces méthodes peuvent être implémentées dans le domaine spatial ou fréquentiel (i.e., domaine de Fourier) [6, 7, 8, 9, 10]. Le principal inconvénient de ces approches est de flouter les images, faisant perdre les petits détails ainsi que les contours. Afin de mieux réduire ces artefacts de lissage, les recherches se sont alors tournées vers des décompositions multi-échelles, notamment des décompositions en ondelettes dyadiques [11]. Une adaptation des filtres pass-bas a été conçue pour modifier uniquement les sous-bandes des détails [4, 12] tout en conservant les coefficients d'approximations.

Le but du Chapitre 4 de cette thèse est de poursuivre l'étude et le développement de ces méthodes de débruitage, en particulier en ce qui concerne les algorithmes de filtrage dans le domaine des ondelettes. Nous proposons une méthode de débruitage basée sur un filtrage de Fourier des sous-bandes d'ondelettes. En effet, les méthodes classiques se basent sur l'utilisation des ondelettes dyadiques, ce qui peut causer des artefacts lors de la reconstruction de l'image à partir des coefficients filtrés.

Nous nous pencherons donc sur des algorithmes de décomposition en ondelettes beaucoup plus adaptés à des problématiques de reconstructions. Nous utilisons notamment des décompositions en ondelettes stationnaires. Le choix de l'ondelette adaptée (type et ordre) à l'analyse n'est pas une chose aisée pour arriver à des résultats parfaits. En effet, l'algorithme de l'état de l'art [4] repose sur l'utilisation d'ondelettes possédant un certain nombre de moments nuls, ce qui peut augmenter la complexité calculatoire. Le choix des décompositions en ondelettes stationnaires nous permettra l'utilisation du filtre de Haar à support compact, qui correspond à une ondelette discontinue à un seul moment nul.

Synthèse de textures par simulation de champs Gaussiens aléatoires: Application à la super-résolution stochastique de champs de SST

Champs Gaussiens pour la synthèse de textures multivariées: La synthèse de textures consiste à donner en entrée une image de texture, et ensuite produire une image de sortie qui soit à la fois visuellement similaire et différente pixel à pixel de l'image d'entrée. Dans cette thèse, nous nous sommes intéressés à des méthodes de synthèse par simulation de champs aléatoires Gaussiens. En particulier, nous considérons des méthodes de synthèse simples, rapides et qui permettent de cibler des caractéristiques spectrales et statistiques. Le modèle dit "bruit à phase aléatoire (RPN)" et "Spot noise discret asymptotique (ADSN)" [2] semblent être les bons candidats. Ces deux processus aléatoires se basent sur la définition d'une image appelée "spot" définie comme l'image de synthèse normalisée. La synthèse par ADSN consiste alors à convoluer cette image avec une réalisation de bruit blanc Gaussien. La simulation par RPN consiste à apprendre les amplitudes de la transformée de Fourier de l'image "Spot" et d'associer des phases aléatoires à chacune de ces composantes. La synthèse se fait ensuite par une transformée de Fourier inverse. Nous pouvons facilement montrer que ces méthodes de synthèse préservent les structures du second ordre. Ces modèles peuvent être étendus pour la modélisation et la synthèse de textures multivariées. Étant donné un vecteur de textures, l'objectif est de synthétiser un autre vecteur de textures tout en préservant les structures du second ordre de chaque texture ainsi que les covariances croisées entre textures. Comme applications, on peut citer par exemple la synthèse de textures en couleur, la simulation d'images multispectrales ou, comme considéré dans cette thèse, la modélisation et la simulation des coefficients d'ondelettes. En ce qui concerne l'extension multivariée, l'approche existante dans l'état de l'art [2] consiste à convoluer chaque "spot" séparément avec la même réalisation de bruit blanc Gaussien dans le cas de l'ADSN. Pour le RPN, la synthèse multivariée se fait en ajoutant la même phase aléatoire à chacune des phases originales des textures. Dans cette thèse, nous avons développé une approche qui permet de faire la synthèse de champs multivariés tout en partant de réalisations différentes de bruits blancs. Cette formulation consiste à simuler un

système d'équation, ici illustré pour le cas trivarié

$$\begin{pmatrix} g_1 \\ g_2 \\ g_3 \end{pmatrix} = \begin{pmatrix} f_{11}(h) & 0 & 0 \\ f_{21}(h) & f_{22}(h) & 0 \\ f_{31}(h) & f_{32}(h) & f_{33}(h) \end{pmatrix} * \begin{pmatrix} \mathcal{W}_1 \\ \mathcal{W}_2 \\ \mathcal{W}_3 \end{pmatrix} \quad (1)$$

où $\mathcal{W}_{i=1,\dots,3}$ est un vecteur de bruits blancs Gaussiens et les opérateurs matriciel f_{ij} sont obtenues en ciblant les structures de corrélations et corrélations croisées des images d'apprentissage.

Outre son intérêt applicatif dans la synthèse de textures multivariées partiellement observées, cette approche présente deux avantages majeurs: 1) L'interprétabilité en terme des structures de covariances et covariances croisées, ce qui rend la considération des modèles paramétriques dans ce cas envisageable, 2) la compacité: notre approche se base sur la définition d'opérateurs liés aux structures de covariances et non pas l'image "spot".

Application à la super-résolution d'images satellitaires de SST: La problématique considérée ici est la suivante: étant donné une image basse-résolution, l'objectif est de pouvoir générer une version haute-résolution qui soit visiblement réaliste et qui possède des caractéristiques similaires à celles des images haute-résolution. On s'intéresse à des caractéristiques visuelles, notamment l'augmentation du contenu de texture de manière réaliste, le rehaussement du contraste (i.e., production des gradients forts) et également à des caractéristiques spectrales (i.e., reproduction du spectre de Fourier) et statistiques (i.e., reproduction des histogrammes).

La figure 3 propose une analyse qualitative et quantitative des images haute-résolution par le biais de la composante inter-échelle (i.e., différence entre observation haute et basse-résolution) et du champs des gradients. L'analyse de la composante inter-échelle met en évidence la présence de structures de petites échelles. Ces structures sont caractérisées par une distribution statistique non-Gaussienne. L'analyse du spectre de Fourier montre la concordance du spectre de la composante inter-échelle avec celui de l'image haute-résolution dans les échelles plus petits que ~ 20 km. Ces spectres sont caractérisés par une loi de puissance. En ce qui concerne les champs du gradient, à haute-résolution les structures des gradients sont fines, avec des valeurs élevées comparées à celles des gradients basse-résolution. Les gradients les plus forts dans la haute-résolution restent présents dans la version basse-résolution mais dans une version lissée. Ce dernier point est observé quantitative-ment en analysant les distributions statistiques associées. Notons qu'en comparant l'aspect géométrique de la composante inter-échelle avec le champ des gradients basse-résolution, on remarque une variabilité forte dans les zones de gradients forts qui sont visibles dans la basse résolution. Ce dernier point suggère une dépendance de la variance de la composante inter-échelle aux gradients basse résolution. Une autre caractéristique importante des images haute-résolution est l'information contenue dans la phase de Fourier. Pour illustrer l'importance de cette composante, la figure 4 illustre une simulation d'un champ turbulent qui contient des structures géométriques marquées, en utilisant seulement la structure du second ordre (i.e.,

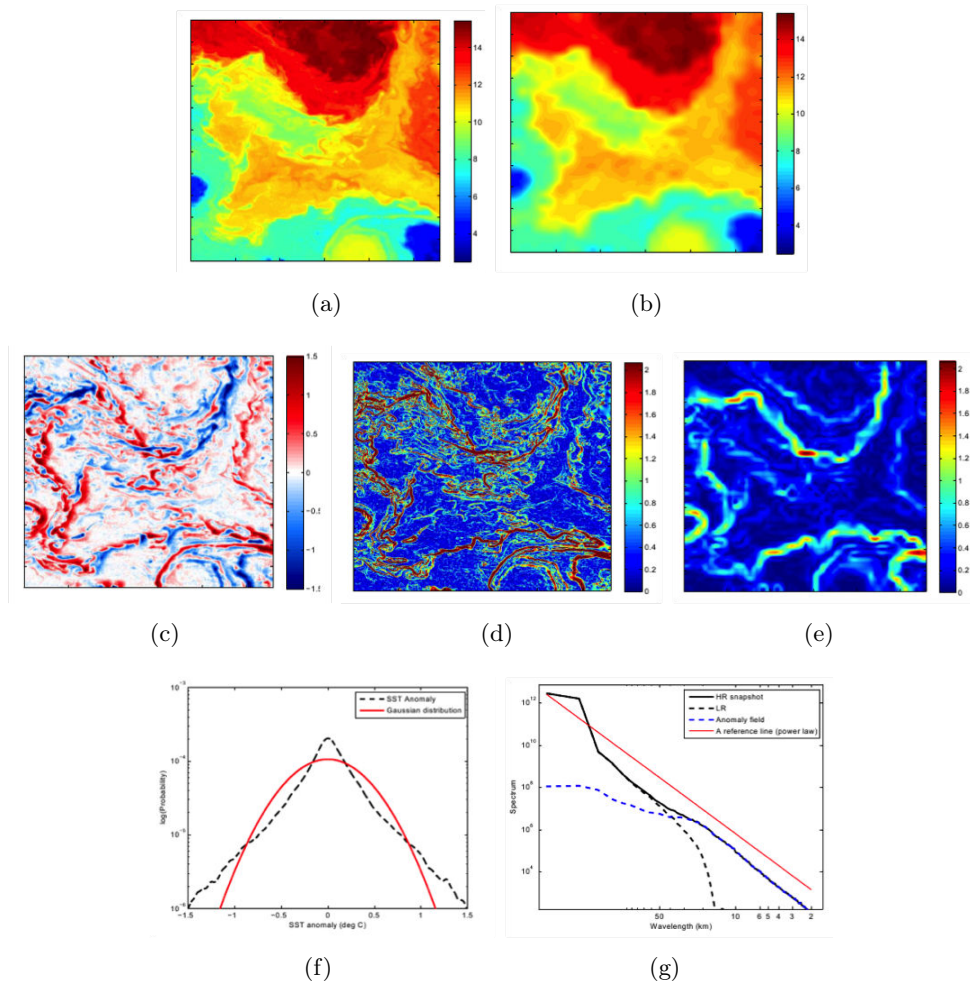


Figure 3: (a) SST MODIS haute-résolution, (b) SST basse-résolution, (c) la composante inter-échelle associée, (d) Gradient de SST MODIS, (e) Gradient de SST basse-résolution, (f) Histogramme marginale normalisée de la composante inter-échelle, (g) spectres de Fourier associés à (a), (b) et (c).

amplitudes de Fourier). Cette simulation montre que l'absence de contrainte sur la phase, on peut obtenir une image qui a le bon spectre, (i.e., la même distribution de la variance selon les échelles que l'image originale), mais cette énergie n'est pas placée aux bons endroits et l'information géométrique (i.e., contours) est complètement détruite. Ces observations empiriques nous ont suggéré l'utilisation de l'information de phase contenue dans la basse-résolution pour la reconstruction des champs inter-échelles. Cela permettra de placer la part d'énergie (ou variance) aux gradients basse-résolution encore visibles.

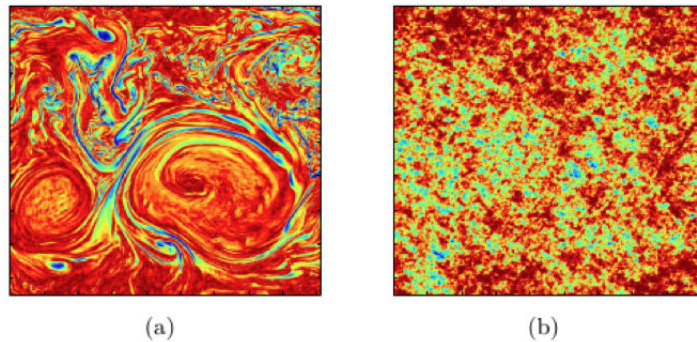


Figure 4: (a) Champ turbulent 2D, (b) synthèse de (a) par apprentissage du spectre avec des phases aléatoires. L'image (b) a exactement le même spectre que l'image (a) mais sans information de phase, l'énergie n'est pas placée aux "bons endroits".

Pour traiter cet enjeu de modélisation inter-échelle, on propose la méthodologie suivante: Tout d'abord, une approche multi-échelle est adoptée. On utilise notamment des décompositions en ondelette stationnaires. Ce choix est motivé par l'importance des facteurs d'échelle recherchés. Dans notre contexte applicatif, ces facteurs sont de l'ordre de 20-32. Le problème de la modélisation inter-échelle est ensuite formulé dans le cadre de la synthèse de texture multivariées avec des contraintes spectrales. Pour pouvoir produire des champs réalistes, notamment les structures géométriques marquées, un conditionnement vis-à-vis la basse-résolution est introduit. Ce conditionnement est explicite en imposant la phase de Fourier de l'image basse-résolution à la composante inter-échelle simulée. Etant donnée une image basse-résolution, le problème de la super-résolution est ensuite posé comme étant la problématique de la simulation de composante inter-échelle. Dans le domaine des ondelettes, étant donnée les coefficients d'approximation (i.e., basse-résolution), le modèle ADSN, appliqué aux coefficients d'ondelettes, est cascadié. Partant des coefficients d'approximation de départ, à chaque niveau de reconstruction, la phase de l'image obtenue au niveau précédent est imposée.

La figure 5 présente des résultats obtenus sur la base d'un champ de température de surface acquis par MODIS. Remarquons que l'image reconstruite présente des caractéristiques similaires à l'image haute-résolution réelle, avec une variabilité plus importante que l'image basse résolution. On constate également que les structures géométriques reconstruites sont cohérentes et présentent des irrégularités

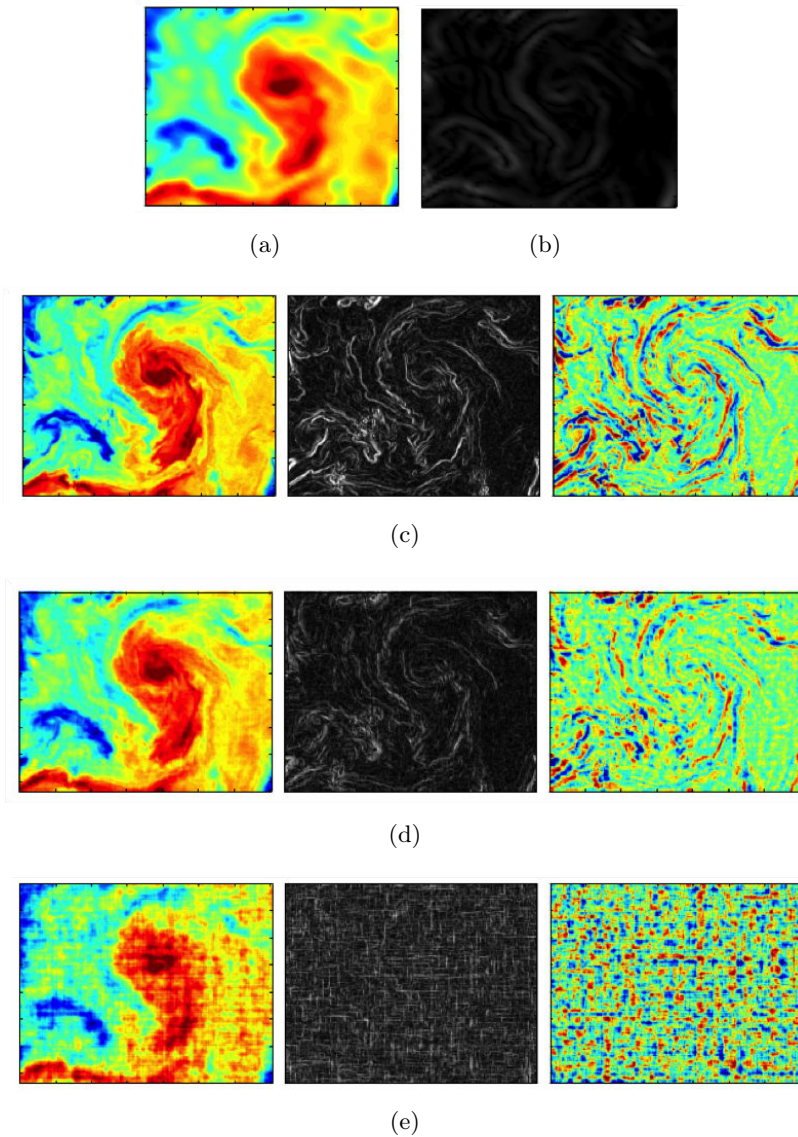


Figure 5: Application à des observations de la température de surface de l'océan (SST). (a) et (b) représentent l'image basse-résolution et son gradient. (d) De gauche à droite: image haute-résolution, gradient haute-résolution et composante inter-échelle. (e) Résultats de reconstruction sans contraintes de phase (même ordre que (d)).

visuellement réalistes.

Caractérisation de la variabilité géométrique dans les observations satellitaires de SST par processus SLE

Le principe général est que les observations satellitaires instantanés (snapshot) d'un traceur géophysique à la surface de l'océan (e.g., SST, Chlorophylle...) contiennent des informations sur les dynamiques sous-jacentes. À titre d'exemple, la figure 6

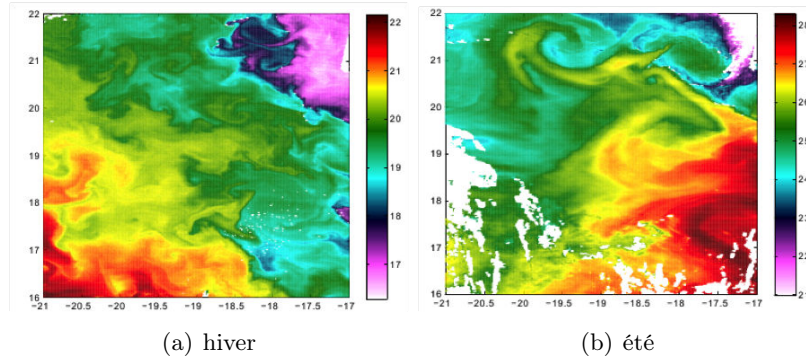


Figure 6: SST MODIS pour la région de Benguela.

illustre deux images de SST dans une zone d'upwelling (la région de Benguela) qui présentent des différences visuellement importantes et dont on peut supposer qu'elles sont liées aux dynamiques sous-jacentes (en particulier, la saisonnalité de l'activité de l'upwelling). La question posée est de savoir quelles sont les caractéristiques de la dynamique qu'on l'on peut extraire de ces images. L'état de l'art propose différents descripteurs classiques. Les figures 7(a) et 7(b) montrent un exemple d'analyse à travers les caractéristiques spectrales et des distributions des intensités du gradient. L'analyse spectrale ne révèle pas de différences avec des pentes spectrales identiques de -3. A contrario, l'observation des distributions des gradients met en évidence des gradients plus fort en été.

Visuellement on note également une géométrie plus irrégulière en hiver, comme illustrée en Fig8(a) par la représentation en lignes de niveaux. La question qu'on s'est posée est de savoir comment décrire quantitativement cette régularité géométrique. Et ensuite d'envisager des modèles de cette régularité géométrique.

Dans cette thèse, on s'est intéressé à des processus de marche aléatoire et plus particulièrement la classe des processus SLE (Stochastic Loewner Evolution) [13]. Ces processus sont décrit par l'équation différentielle stochastique suivante

$$\partial_t g_t(z) = \frac{2}{g_t(z) - \xi(t)}, \quad g_0(z) = z, \quad (2)$$

Cette équation est définie dans le plan complexe et correspond à des itérations de compositions de transformations conformes $g_t(z)$ forcées par un mouvement Brownien $\xi(t)$. Ce mouvement Brownien est caractérisé par une diffusivité κ qui contrôle la

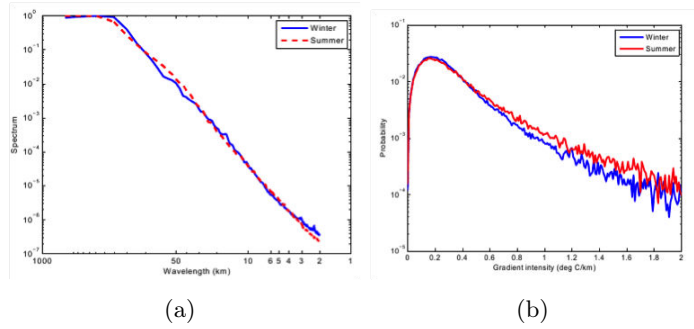


Figure 7: Estimation des spectres de Fourier (a) et les distributions des gradients (b) des images de SST représentées en 6.

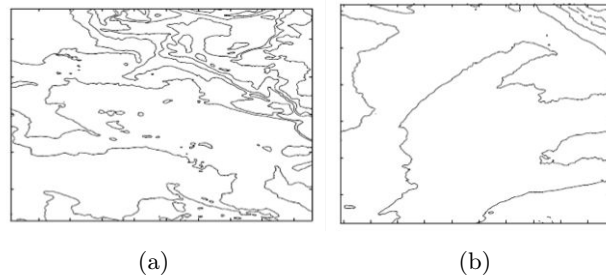


Figure 8: Représentation en lignes de niveaux des images de SST représentées en 6.

régularité géométrique de la courbe. à titre d'exemple, la figure 9 illustre différents niveaux d'irrégularité géométrique en fonction de κ . Typiquement entre des valeurs

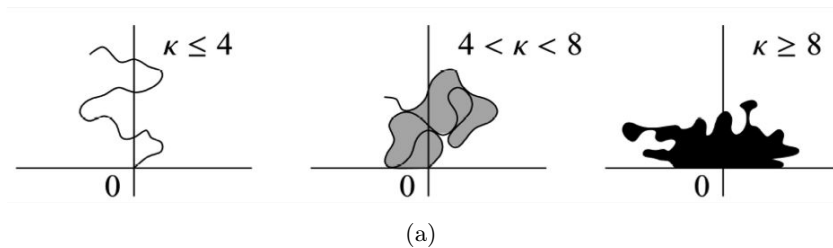


Figure 9: Exemple de régularité géométrique des courbes SLE en fonction de κ . Dessin extrait de [14].

entre 4 et 8 on observe des courbes avec des points doubles, une valeur supérieur à 8 correspond à des courbes qui remplissent tout l'espace. Il est important de noter qu'il est possible d'estimer la fonction directrice à partir d'une courbe observée. Ces processus SLE, associés à des caractéristiques d'invariance conforme, apparaissent naturellement dans plusieurs système physique : Percolation, Turbulence 2D , Modèle d'ising...

L'analyse SLE est un outil qui semble particulièrement adapté à notre problé-

matique et qui offre un cadre théorique générale vis-à-vis d'autres approches plus empiriques comme: L'analyse des "winding angles" ou l'analyse des fonctions de structures. Il a été montré que ces processus apparaissent naturellement dans systèmes de turbulence 2D [15].

La figure 11 illustre un exemple d'analyse SLE réalisé sur un champs de SST LandsAT haute-résolution au large de la côte bretonne (Fig10). L'analyse SLE a été appliquée à l'ensemble des lignes de niveaux de l'image.

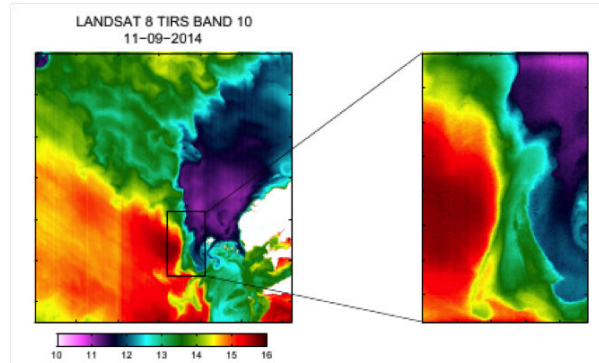


Figure 10: Image satellitaire de température de surface acquise par Landsat TIRS avec un zoom sur une zone d'intérêt.

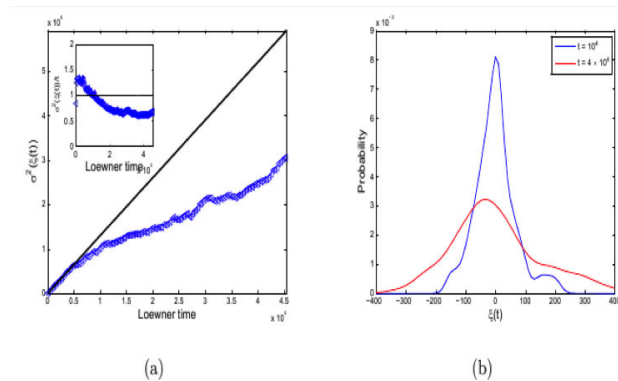


Figure 11: Exemple d'analyse SLE appliquée à l'ensemble des lignes de niveaux de l'image illustrée en figure 10. (a) Variance des fonctions directrices en fonction du (pseudo) temps, (b) la distribution statistique de la fonction directrice à deux instant différents.

La figure 11 illustre les caractéristiques moyennes des fonctions directrices extraites. Nous remarquons que l'évolution de la variance des fonctions directrices en fonction du (pseudo) temps n'est pas linéaire. On note un comportement non-Brownien. Le comportement Brownien correspond à une relation linéaire. De la même manière, la distribution statistique des incréments ne suit pas une loi gaussienne. Cela nous a conduit à explorer des facteurs qui pourraient contraindre les

caractéristiques des fonctions génératrices.

En particulier, il apparaît assez nettement que les lignes de niveaux ne partagent pas les mêmes caractéristiques.

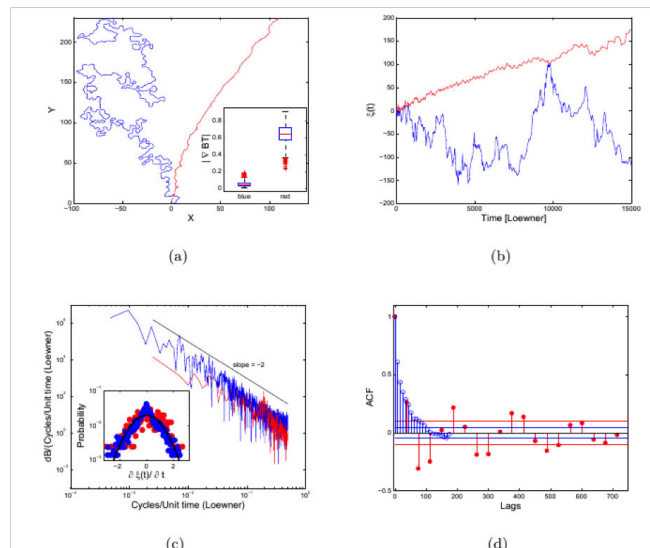


Figure 12: (a) Les deux portions de lignes de niveaux sur lesquelles l’analyse SLE a été effectuée, (b) les fonctions directrices extraites, (c) Spectres de Fourier, (d) la fonction d’autocorrélation des incréments des fonctions directrices.

La figure 12 illustre un exemple d’analyse SLE appliquée sur deux lignes de niveaux particulières avec des niveaux de régularité très différents. L’analyse des fonctions directrices des deux lignes de niveau montre clairement un niveau de variabilité très différent. Par contre, comme illustré en figure 12(c), après normalisation par l’écart type des incréments, les deux courbes présentent des caractéristiques similaires en terme des pentes spectrales des fonctions directrices et en terme des distributions statistiques des incréments. On note que les deux courbes ne correspondent pas aux mêmes niveaux du gradient. Plus largement, on observe visuellement des différences de régularité géométrique entre les zones de fort gradient et les zones de plus faible gradient. Ceci nous amène à explorer un conditionnement des processus SLE par le gradient basse résolution.

Ce type de conditionnement nous a conduit à une analyse des fonctions directrices par classe d’intensité du gradient. On met clairement en évidence l’effet du gradient sur la variance de la fonction génératrice. Avec des variances fortes à gradient faible et inversement pour les gradients forts des variances faibles. Ceci correspond à l’observation empirique d’une régularité géométrique contrôlée par le gradient. Par ailleurs, les fonctions génératrices présentent des caractéristiques spectrales en loi de puissance peu corrélée du gradient.

Nous proposons donc de formaliser les lignes de niveaux d’un champ de SST comme des processus SLE conditionnels dont les fonctions directrices sont des processus Brownian fractionnaires conditionnés par la norme du gradient. En outre,

nos résultats suggèrent de poursuivre l'étude des processus SLE pour caractériser la variabilité des dynamiques superficielles à petites échelles.

Introduction and Context

The development of both satellite-based sensors for the remotely sensed observations of geophysical tracers at ocean surface and the associated processing algorithms has significantly improved over the last twenty years. Among the observed ocean surface variables, Sea Surface Temperature (SST) is recognized as Essential Climate Variables (ECVs). Rather than its temporal evolution, the most important feature of the SST, as well as the other oceanic variables, is how it varies spatially. Its observed spatial distribution is constrained by the spatial resolution of the instrument which the parameter is captured from. This means that the spatial scale of the satellite product determines the physical processes (e.g., eddies, currents...) which can be studied. It is clear that as the resolution of the SST products increases, it will become possible to unveil and study small scale oceanic features (i.e., sub-mesoscales) and the way that it may well be impacting large scale processes (i.e., mesoscales). Notice, that until recently, most models assume that scales smaller than the largest mesoscale eddies were negligible. However, recent numerical and observational studies have demonstrated that the upper ocean is rich in structures and processes at small scales [16, 17, 18]

Satellite-based sensors involve spatial and temporal resolutions, as well as different sensitivities to weather conditions, especially cloud coverage and heavy rainfall. For instance, regarding SST observations, high rates of missing data may occur in high-resolution infrared observations (1kmx1km) unlike low-resolution microwave-based data (25-50 km). In other words, direct observation of the upper ocean at small-scales is very challenging. According to the targeted applications, one may need a realistic reconstruction at high-resolution of the the SST fields in the presence of clouds from only the available low-resolution measurements. Describing and parametrizing these small scale features is very challenging from a statistical point of view. Indeed the modeling has to be sophisticated enough to handle these patterns but computationally tractable to keep the estimation and simulation feasible.

Stochastic methods and statistical learning algorithms have been introduced to address both issues [19]. In this thesis, we focus on two problems: the reconstruction of high-resolution SST fields from low-resolution observations, referred to as SST super-resolution, and the characterization of the turbulence-related geometrical patterns exhibited by SST fields. Our general objective is to identify random models, which can mimic statistical properties exhibited by real observations, and to explore possible parameterization variabilities. It may be noted that, unlike classical reconstruction issues in image processing, the actual reconstruction of the

true high-resolution fields may not be meaningful given the randomness of the processes. As such, SST fields may rather be considered as textural fields and our study relates to texture synthesis and analysis. The intrinsically multi-scale nature of the underlying dynamical processes naturally leads us to consider multi-scale and scale-invariant random processes, namely spectrally-constrained random processes and conformally-invariant random processes. Beyond the theoretical and computational analysis of the considered models, We give more emphasis to parametric representations with a view to making easier their geophysical interpretation.

The introduction is organized as follow: In section 1.1, we present a brief description of the various sources of remotely sensed SST data considered in this thesis. We focus our discussion on their underlying characteristics and challenges. We briefly present our contributions in terms of data characterization and pre-processing. In Section 1.2, we describe the class of Gaussian texture-based models that we use to build stochastic generators that encompass the features of the considered data. We briefly introduce the considered directions for embedding in such models the patterns exhibited by SST data, especially multi-scale patterns. The following section 1.3 further introduce the use of the described models in the super-resolution framework. We finish in Section 1.4 by a description of the proposed work.

1.1 Considered SST data and related issues

In order to provide global coverage of SST with dense spatial and temporal resolutions, in situ measurements from buoys and ships are inadequate. Despite the fact that these (direct) measurements are very accurate, their spatial coverage is sparse, which makes their exploitation limited for the observation submesoscale phenomena at the ocean surface. Earth-observing satellite instruments provide such capability. Satellite-derived sea surface temperature fields are often rich in small-scale structures reflecting very important underlying oceanic processes related to eddies, currents [20]. However, direct observation of the various upper ocean phenomena and processes at fine-scales, using satellite-based instruments, remains challenging for two reasons:

1. Because of the Cloud cover, SST fields obtained using high-resolution infrared sensors [21] are significantly impacted by a high rates of missing data. This is because the black body spectrum of the infrared emission from Earth is almost absorbed by the water vapor and aerosol composing the clouds. The typical resolution of the infrared SST data varies between 1km to 10km, while the temporal sampling varies from a few minutes to several hours. For instance, geostationary sensors (e.g., SEVERI, GOESS...) provide high temporal resolutions but only for regional coverage. By contrast, near polar-orbiting instruments (e.g., VIIRS, MODIS, AVHRR...) provide a global coverage with repeat time from 12 hours to several days.
2. The low-resolution data obtained using micro-wave instruments are insensitive to the cloud cover and can represent an alternative to those obtained by

the infrared sensors to observe ocean parameters even under cloudy-sky conditions. The reason is that the emitted micro-wave signal penetrates clouds. However, the passive microwave signal is affected by other phenomena such as precipitations. Unfortunately, because of the coarser resolution of the associated products, the use of this type of data is limited to the observation of large-scale phenomena (i.e., mesoscale, global fronts...) of the global ocean. As an example of the SST micro-wave sensors, we limit ourselves here to AMSR sensors.

To illustrate the above remarks, we proceed as follows. First, we calculate and compare the probability of occurrences of clear-sky pixels (i.e., missing data statistics) associated to the two types of SST products. To this end, we use one year of daily L3 gridded data obtained respectively from the MODIS-only and AMSR-E-only sensors. Both instruments are on-board the NASA Aqua platform and the spatial resolutions of the considered (processed) products are respectively $4km$ and $25km$. The resulting probability maps are shown in Fig.1.1. Each pixel value of these fields represents the probability that the underlying pixel is cloud-free for MODIS (resp. rain-free for AMSR-E) over one year. It is clear from these probability maps that the micro-wave data are less impacted by gaps. It is worth noting that cloud-free pixels for MODIS are likely localized near coastal areas.

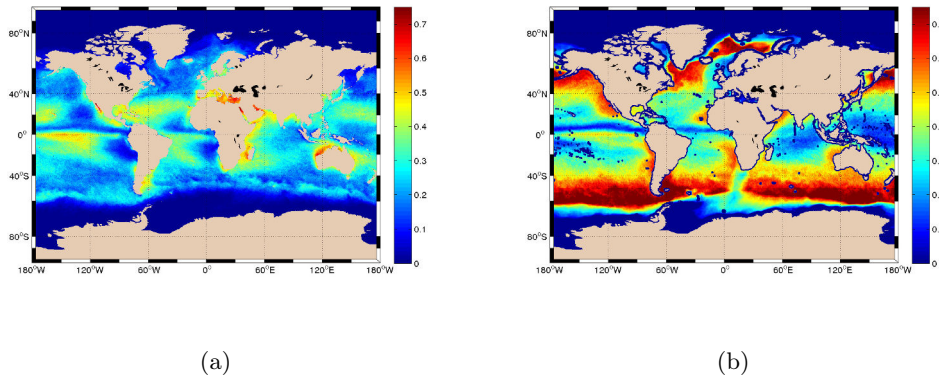


Figure 1.1: Probability of occurrences of clear-sky pixels during 2004 in (a) Modis L3 data (b) AMSR-E

We further illustrate the characteristics of the various type of remotely-sensed SST data from real data in Fig.1.2. In the first example, we show satellite-derived SST snapshots captured simultaneously (and independently) by, respectively, infrared and micro-wave sensors under clear sky conditions. The second example involves a cloudy weather. Whereas more than 75% of data were missing for IR MODIS snapshot (Fig.1.2(c)), the AMASR-E (Fig.1.2(d)) snapshot is unaffected by clouds. The high mission date rates point out the need for super-resolution algorithms with a view to reconstructing realistic high-resolution SST fields from the

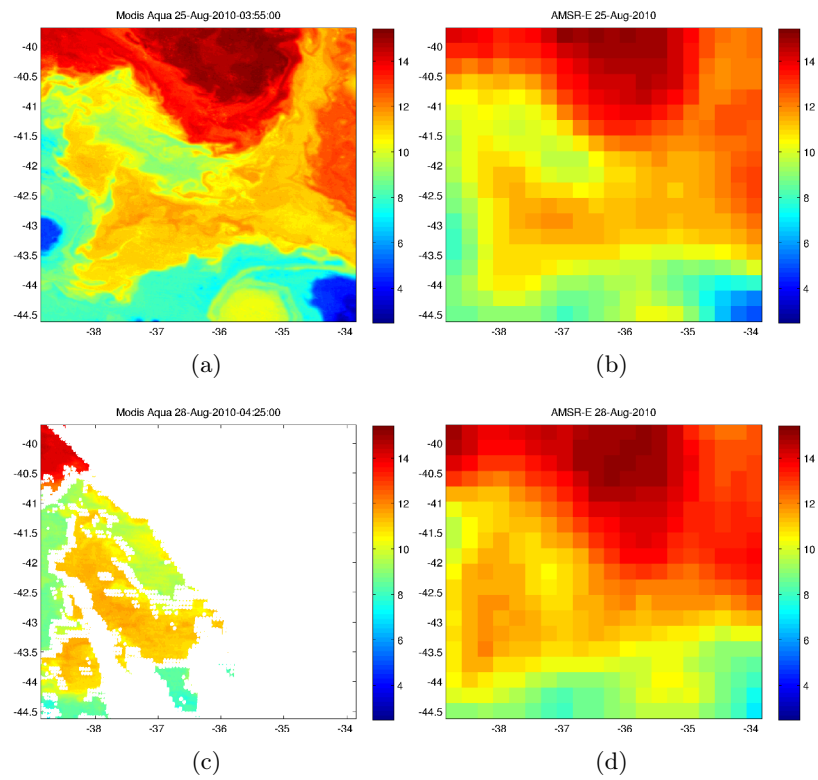


Figure 1.2: Example of satellite-derived SST snapshots acquired by MODIS ((a) and (c)) and AMSR-E ((b) and (d)) on Aqua platform in the Malvinas region. The snapshots of the first row were acquired on Aug. 25, 2010 and depict a cloud-free scenario. By contrast, the snapshots second row images were acquired 3 days later under a heavily cloudy conditions.

observed low-resolution conditions. This is the core of this thesis with an emphasis on the introduction of novel stochastic models, along with their theoretical and computational characterization in Chapters 2 & 3 and on the application to SST field in Chapter 6.

Besides missing data rates, the reported examples stress the remarkable richness of the fine-scale structures observed in real SST fields. As pointed out by Fig.1.2, IR MODIS snapshot reveals such ocean turbulence patterns, which are widely filtered out by AMASR-E snapshots. These fine-scale structures are expected to have a critical role in the geophysical and ecological processes at ocean's surface [22]. A natural question, therefore, is to ask how we can objectively describe and characterize the small-scale heterogeneities of this images. For that purpose, traditional methods based on the spectral analysis, leading to the estimation of the scaling properties, may be considered. Unfortunately, the underlying multi-scale oceanic processes and the related features cannot be characterized by a single scaling exponent (i.e., the slope of the Fourier spectrum) and more sophisticated methods are required. Chapter 4 addresses this issue. We follow some recent attempts to characterize turbulent dynamics based on numerical simulations [15] to focus on the analysis of the geometrical regularity of satellite-derived SST level lines.

Yet another drawback of working with high-resolution infrared datasets is the presence of undesired noise patterns contained in the various products. The super-resolution methods developed in this thesis belong to the family of the learning-based methods which consists on direct sampling image priors from high-resolution fields. Prior to the learning step, we shall need to eliminate or at least reduce the amount of undesired noise patterns. In chapter 5, we deal with the suppression of the striping noise contained in SST L2 products. We propose a combined Fourier-wavelet filtering method and adapt it to the case of gaped datasets. We demonstrate the benefits of the proposed scheme with respect to state-of-the-art methods for different datasets.

1.2 Sample-based texture analysis and synthesis

In what follows, we consider a class of textures associated with geophysical dynamics. Building models and synthesis algorithms for these kind of textures is a challenging problem that has received much attention over the past years. Non-stationary models are often needed since traditional stationary (and isotropic) assumptions appear too restrictive for capturing the complex patterns observed in remotely sensed SST fields. Furthermore, SST fields contain features at various levels of detail, i.e., at different scales. A multiresolution analysis and synthesis seems necessary. A great deal of the potential candidate models is how to manage all the observed scales. Sample-based stochastic texture models have been developed to simulate, in a statistical framework, possible realizations of the considered geophysical fields at given scales. Assuming that the fields are stationary and normally distributed, which is

not a realistic hypothesis in the case of textures associated with turbulent flows, all we need to specify is an appropriate second order function.

For the standard Gaussian Random Field Texture prior models, the prior model is classically specified by covariance functions. A covariance function of an homogeneous (or stationary) RF is defined by a continuous positive definite function that depends on the relative position of pixels.

$$\text{Cov}(X(\vec{x}), X(\vec{y})) = f(\vec{x} - \vec{y}) = f(\vec{h}) \quad (1.1)$$

where X is the RF, \vec{x} and \vec{y} are the spatial locations and $\vec{h} = \vec{x} - \vec{y}$ is the relative position. In the case of isotropic fields, the covariance function only depends on the distance lag between points. As already mentioned, under the Gaussian setting, the covariance function completely defines the stationary field. A variety of classical covariance models, including exponential and Gaussian models, may be considered. Formally, a Gaussian field relates to the following multivariate p.d.f.:

$$p(x|Q, \mu) = (2\pi)^{(n/2)} \det(Q)^{(1/2)} \exp\left(-\frac{1}{2}(x - \mu)^t Q (x - \mu)\right) \quad (1.2)$$

where $Q = \Sigma^{-1}$ is the precision matrix (i.e. the inverse of the covariance matrix Σ). Limitations of the covariance-based methods, related to the so-called 'the big n problem', are known for both the inference and synthesis setting. In fact, as we can see from the likelihood (1.2), the formula involves finding the inverse of the (dense) covariance matrix. As an example, consider the problem of synthesizing a 50×50 pixel random field, it gives rise to the inversion of 2500×2500 pixel matrix. Therefore, this method leads to a huge computational and memory complexity. In this thesis, we deal with high-resolution satellite-based data and we are interested in the simulation of relatively large fields (typically, 512×512 fields for a global scale). Recently, [2] presents another set of approaches based on statistical constraints (i.e., Second order statistics). The various methods were then adapted to the context of texture synthesis with a special focus on the color texture. Both randomization processes can be expressed in the Fourier domain. The proposed corresponding synthesis algorithms are fast and reliable since the corresponding algorithms rely on the Fast Fourier Transforms (FFT). Despite the fact that both models are non-parametric and homogeneous, equivalent parametric formulations can be derived through the selection of appropriate parametric models for the spectrum. Starting from an exemplar image, and assuming that the selected prior theoretical model holds, the parameters can be estimated by fitting empirical spectrum to the considered theoretical model. Moreover, using the fact that both models can be written as convolution product, non-stationary extensions are possible by allowing the convolution operator to spatially vary. To the extent of our knowledge, this extension must be performed in the spatial domain and has no Fourier-based formulation. This leads to relatively more computational and/or memory complexity compared to the standard stationary case, but still more efficient than the covariance-based method described above. In the non-stationary case, the prediction of the statistical features exhibited by realizations of the random model may also be a complex issue.

Another way of pursuing good prior models with fast computations and low memory requirements is through the use of pseudo-differential operators. In this approach, the random image is expressed as a solution of a Stochastic Partial Differential equation (SPDE). The sparsity of the resulting precision matrices makes storage and computation manageable. Recently, [23, 24] studied such operators from a statistical point of view. The considered operator is a Laplacian-like operator of the form $\mathcal{L} = (\kappa - \Delta)^{\alpha/2}$, with κ and α are positive real parameters. The main important results of their contributions are the following: First, they establish the explicit link between the above differential operator and the class of Matérn covariance family. Secondly, they built a link with the class of the (discrete) Gaussian Markov fields. The established Markovian propriety is very useful and leads to very sparse precision matrix. It was followed by some extensions to take into account non-stationarity [25], non-Gaussianity [26] and to generate multivariate fields [27]. Notice that various applications were also considered. In [28], we considered a direct application of the non-homogeneous Matérn SPDE class to the problem of the exemplar-based super-resolution with a focus on satellite-based imagery.

The above-mentioned models do not explicitly address the multi-scale patterns exhibited by natural textures and textures associated to geophysical fields. This is a key contribution from Chapter 2, where we explore such extensions with a focus on cross-spectral constraints.

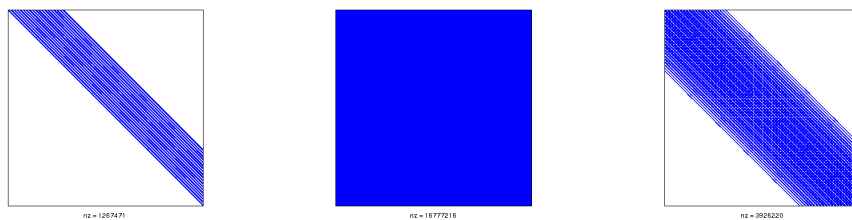


Figure 1.3: (a) The sparsity structure of the matrices involved in the inference and the synthesis of textures using the SPDE and equivalent approaches comparing with (b) the dense matrices using the classical covariance-based method. Even using the covariance tapering [1] to approximate the likelihood (1.2), the resulting matrices are relatively less sparse than (a).

1.3 The use of systems of texture-based models as a priors in image super-resolution

In this thesis, we consider the application of the various stochastic texture-based models developed in Chapter 2 to the super-resolution of textured images. We aim at simulating a high-resolution textured image given a low-resolution sample. Formally, image super-resolution is stated as the conditional sampling of a stochastic model with respect to a low-resolution condition. Our specific interest is in the state-

ment of different image priors to constrain the spectral, statistical and geometrical aspects and proprieties of the reconstructed high-resolution image conditionally to the low-resolution observation. Specifically, we consider the multi-scale stochastic texture-based models and the associated algorithms developed in Chapter 2. Chapters 3 & 6 explore different parameterizations. In Chapter 3, we shall concentrate on the classical univariate models in the spatial domain. In this setting, the first and the second order moments, at various scales, are controlled. Following the ideas from [29], we consider additional constraints on the phase information of the reconstructed fields, the phase being a key feature of the exhibited geometrical patterns. In Chapter 6, we embed the stochastic models from Chapter 2 within a multi-scale wavelet-based representation and focus on real SST fields.

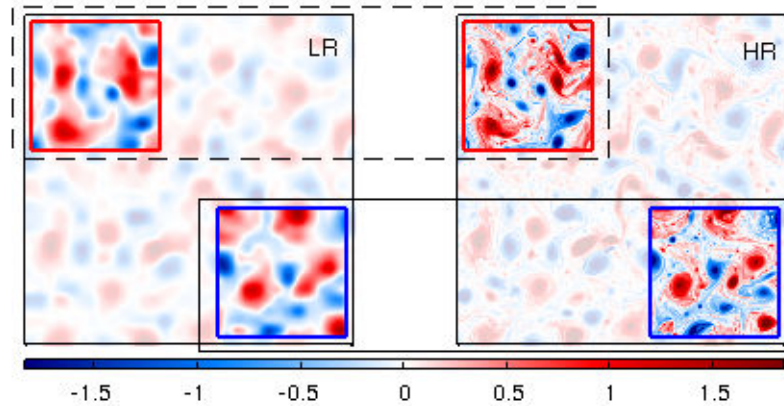


Figure 1.4: Illustration of the Exemplar-based super-resolution as considered in this thesis.

1.4 Outline of the thesis

This thesis is divided in two parts. The first Part is devoted to the theoretical and algorithmic study of considered textural-based models. In Chapter 2, after a brief state-of-the-art of the existing texture models and synthesis methods, we extend the second-order models reviewed by [2] to the multivariate case. Chapter 3 addresses an application to image super-resolution with additional phase-related constraints. The second Part of the manuscript focuses on the modeling and analysis of satellite-derived SST fields with three contributions: the pre-processing of striping noise patterns (Chapter 4), the statistical characterization and modeling of the geometrical patterns of high-resolution SST fields (Chapter 5) and the simulation of high-resolution SST fields conditionally to low-resolution observations (Chapter 6).

1.5 Publications

Journal Papers

Published

- B.Boussidi, R.Fablet, E. Autret, and B. Chapron, "Accroissement stochastique de la résolution spatiale des traceurs géophysiques de l'océan: application aux observations satellitaires de la température de surface de l'océan", *Revue française de photogrammétrie et de télédétection*, no.202, pp. 66-78, March 2013.

- Fabian Schloesser and Peter Cornillon and Kathleen Donohue and Brahim Boussidi and Emily Iskin "Evaluation of thermosalinograph and VIIRS data for the characterization of near-surface temperature fields", *Journal of Atmospheric and Oceanic Technology*

To be Submitted

- B.Boussidi, R.Fablet, and B. Chapron, "SST-derived geometrical characterization of ocean surface dynamics using Schramm-Loewner Evolution", to be submitted at *Geophysical Research Letters* . **Chapter 4**

- B.Boussidi, R.Fablet, and B. Chapron, "Removing striping noise from cloudy Level-2 Sea Surface Temperature datasets", to be submitted at *Remote Sensing of Environment*. **Chapter 5**

- B.Boussidi, R.Fablet, and B. Chapron, "Superresolution of low-resolution satellite SST images using phase-constrained and cascaded multivariate Gaussian models", to be submitted at *IEEE transactions*. **Chapter 6**

Conference Papers

- B.Boussidi, R.Fablet, E. Autret, and B. Chapron, "Stochastic super-resolution of satellite-based Sea Surface Temperature using conditional SPDE models", *IEEE Geoscience and Remote Sensing Symposium*, 2014

- B.Boussidi, R.Fablet, E. Autret, and B. Chapron, "Champs Gaussiens conditionnels pour la modélisation inter-échelle de textures: Application à la super-résolution en télédétection satellitaire de l'océan", *Reconnaissance de Formes et Intelligence Artificielle (RFIA)*, 2014

- R.Fablet, B.Boussidi, E. Autret, and B. Chapron, "Random walk models for geometry-driven image super-resolution", *IEEE International Conference on*

Acoustics, Speech and Signal Processing (ICASSP), 2013

Part I

Stochastic partial differential equations (SPDE) and Texture synthesis

Texture synthesis using univariate and multivariate sample-based stochastic models.

Contents

1.1	Considered SST data and related issues	18
1.2	Sample-based texture analysis and synthesis	21
1.3	The use of systems of texture-based models as a priors in image super-resolution	23
1.4	Outline of the thesis	24
1.5	Publications	25

In this chapter, we explore the mathematical results of two exemplar-based texture models. Namely, random phase noise (RPN) and asymptotic discrete spot noise (ADSN). Both models allow us to synthesize stationary Gaussian textures that does not exhibit macro geometric details. This mathematical and experimental study is completed by two contributions for both categories of texture synthesis models. The RPN and ADSN models are first extended to the multivariate framework. Second, parametric SPDE-based representations are introduced.

2.1 Introduction

2.1.1 The texture synthesis problem

The goal of the Example-based (or sample-based) texture synthesis is to develop an efficient generation procedure to produce new textures from a given input sample. The success of the synthesis procedure is determined by the visual fidelity of the synthesized textures with respect to the given samples and also by the capability of reproducing the textural quantitative characteristics of the original sample (e.g., histograms, spectra, high order statistics...). The process of synthesizing new textures from a sample has received great attention over the last few years in the image processing field and associated applications, including realistic texture rendering in computer graphics, denoising and inpainting of textured images...

In this thesis, we deal with the synthesis of the stochastic gray-scale textures. Using a given (single) model, the more difficult part of the synthesis problem is the

ability to deal with the wide variety of the scale-dependent features exhibited by a given sample. The superposition of all these scales (e.g., Fourier modes, wavelet subbands) gives rise to non-Gaussian scenarios with non-homogeneous anisotropic patterns, what leads to complex parametrization.

2.1.2 Previous work (Parametric and non-parametric approaches)

We restrict ourselves to statistical models and may refer the reader to [30, 31] a wider review of textural models. Broadly speaking, one can divide the texture synthesis methods in two main categories. The first category embed non-parametric methods, among which patch-based methods introduced in [32] are the most popular and efficient. A second category of approaches involve parametric models, and mainly statistical models, including for instance, auto-regressive models, Markov random fields, Gaussian processes....These models requiring learning on large-scale datasets seem less appropriate to our application context.

Parametric models: A variety of parametric models have been introduced for texture synthesis. 2D auto-regressive and Gibbs random fields for instance rely on the explicit modeling of the conditional likelihood of a pixel given some neighborhood. Different local parameterizations may be considered (e.g., co-occurrence-based [33], response to filters [34]). The simulation of textured images generally relates to Gibbs sampling strategy and model calibration resorts to classical statistical criterion (e.g., Maximum Likelihood, Maximum Entropy,...). Other parametric models are associated with specific textural features such as spectral constraints [2] or marginals of wavelet decomposition [35]). It may be noted that parametric models may be stated in the original image domain as well in a transformed domain (Fourier transform, wavelet decomposition,...). In this respect, covariance-related and associated Fourier-based representations will be of particular interest in our study. They are introduced more precisely in the following section. Overall, the main limitation of parametric methods may be their limited capabilities the wide range of textural patterns as they are, by nature, expected to (only) reproduce some predefined specific textural characteristics. Conversely, they provide a compact representations of textures, which may make easier their interpretation.

Non-parametric models: From the early 2000's, non-parametric models, especially patch-based ones, have gained much interest for texture synthesis. They rely on some patch-wise copying scheme to resample a new textured image from an exemplar [36]. Later enhancements and extensions on this idea led to dynamic (or volumetric) texture synthesis as well as application to missing data interpolation for satellite-derived missing data interpolation [37, 38]. It may be noted that patch-based models can be restated as Markov Random Fields [39]. Despite the fact that the synthesis results obtained by this method are visually very satisfactory in the case of very structured texture examples, the resulting textures are almost obtained by a simple juxtaposition of small patches directly sampled from exemplars, which means that these methods have a limited innovation capacity. Besides, such non-parametric schemes offer little interpretation possibilities.

Recently, the combination of parametric and non-parametric frameworks provide new solutions, which may be of interest for future work. We may cite [40, 37] the combination of patch-based models to spectral and marginal features as a mean to better control the textural samples synthesized by patch-based models. The application of deep learning architectures [41] to texture synthesis may also be viewed as an example of a similar strategy, whose benefits for the considered application would require additional analysis.

2.1.3 Contribution of the Chapter

In this paper, we introduce the generalization of the RPN and ADSN models to multivariate case. We develop fast synthesis algorithms for both multivariate random processes. The models allow us to impose spectrum and cross spectrum constraints on the synthesis as demonstrated in the experimentation sections. The approach is compared to the classical method [2] and the benefit of the proposed constraints is demonstrated. One of the rather interesting aspects of the proposed approaches is that they can be written as solution of parametric SPDE equations. That will be of importance in the case of synthesis of partially-observed textures.

The plan of this chapter is as follows. In Section 2.2 we introduce the basic results of the spot noise model. The asymptotic limit of this model, known as ADSN, is presented in 2.3. In section 2.4 we present the RPN model. Both models are extended to the multivariate case in 2.5. SPDE-based formulations and associated possible parametrizations are discussed in 2.6. We present the conclusion of this chapter in Section 2.7.

2.2 Shot (Spot) noise model

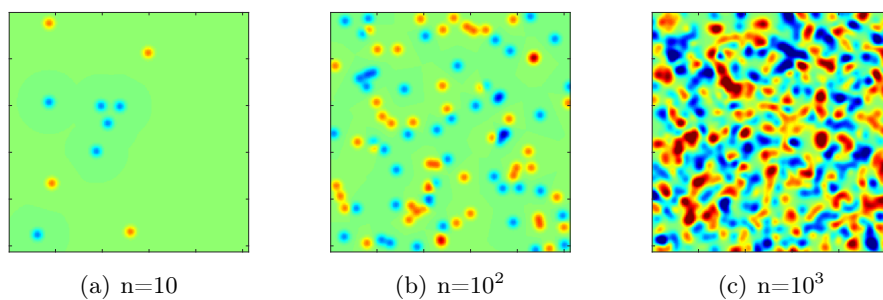


Figure 2.1: Spot noise associated with the Gaussian kernel with different values of n . A stationary texture is obtained as n increases.

The shot noise model is the most elementary strategy to simulate and obtain a 2D stationary (Gaussian) random field. Fundamental results of this model go back to Rice [42]. The idea consists in superposing a large number of identical but shifted copies of an elementary kernel, a deterministic function called spot, whose centers

are randomly (uniformly) chosen over the domain. Formally, the spot noise process is given by

$$X_n(x) = \sum_{i=1}^n h(x - x_i) \quad (2.1)$$

where h is the deterministic spot and the random set $(n, x_{i=1, \dots, n})$ is generally modeled the realization of a Poisson point process on a rectangular domain of intensity $\lambda > 0$. The convergence to a (stationary) Gaussian process as the intensity increases is well known [43]. Fig.2.1 shows several realizations of 2.1 using a Gaussian kernel for different values of n . It may be stressed that the obtained images converge to an homogeneous texture-like image. This limit object, called ADSN, was rigorously defined in [2] and will be studied in the next section. We now consider the spectral representation of the spot noise process. By taking the Fourier transform of 2.1 and exploiting its linearity we obtain

$$\hat{X}_n(k) = \sum_{i=1}^n \hat{h}(k) \exp(-jkx_i) \quad (2.2)$$

$$= \sum_{i=1}^n |\hat{h}(k)| \exp(j(\rho(k) - kx_i)) \quad (2.3)$$

where $\rho(k)$ is the phase of the spot h . Remark that the spatial shift of the original spot does not shift the corresponding Fourier transform at all, but rather multiplies the output by a linear phase.

2.3 ADSN

In this section, we investigate the interesting limit process of the Spot noise model described in the latest section. For this purpose, we proceed as follows. Let us consider an uniform random variable X on Ω and $\mathcal{H}(x) = h(x - X)$, where h is a deterministic spot function. One can verify by a direct computation that the expectation value of $\mathcal{H}(x)$ is $\mathbb{E}(x) = \mu \mathbf{1}_\Omega$, where $\mathbf{1}_\Omega$ is the indicator function over Ω . The autocovariance function is given by

$$Cov_{\mathcal{H}}(x, y) = Cov(\mathcal{H}(x), \mathcal{H}(y)) \quad (2.4)$$

$$= Cov(h(x - X), h(y - X)) \quad (2.5)$$

$$= \mathbb{E}((h(x - X) - m)(h(y - X) - m)) \quad (2.6)$$

$$= \frac{1}{|\Omega|} \sum_{u \in \Omega} (h(x - u) - m)(h(y - u) - m) \quad (2.7)$$

$$= Cov(h(x), h(y)) \quad (2.8)$$

$$= Cov_h(x, y) \quad (2.9)$$

In view of 2.9 the autocovariance function of \mathcal{H} is exactly the same as that of the spot function h . This property is particularly important. One consequence of

the central limit theorem applied to the random sequence $\{\mathcal{H}_n\}_{n \geq 1}$ as $n \rightarrow \infty$ is that $\sqrt{n}(\mathcal{H}_n - m\mu\mathbf{1})$ converge in distribution towards the multi-dimensional normal distribution $\mathcal{N}(0, Cov_h(x, y))$. We can now introduce the ADSN (Asymptotic discrete spot noise) associated with the spot h to be a centered random Gaussian field whose autocovariance function is given by $Cov_h(x, y)$ [2].

In the following, we show that the ADSN associated with the spot h can be simulated by a convolution of a normalized copy of h with a Gaussian white noise whose components are *i.i.d* with distribution $\mathcal{N}(0, 1)$. Let $\mathcal{W}(x, y)$ be a Gaussian white noise with $\mathbb{E}(\mathcal{W}) = 0$ and $\mathbb{E}(\mathcal{W}(u)\mathcal{W}(v)) = \mathbf{1}_{u=v}$. The idea of this construction is that the random field defined by $Y = \tilde{h} * \mathcal{W}$ is a random Gaussian field with the same distribution as the ADSN process associated with the sport h [2]. Since the convolution is a linear operator, it is immediate that Y is Gaussian. In order to properly establish the relationship between the ADSN and the convolution process, we have to prove that $\mathbb{E}(Y) = 0$ and $Cov_Y(x, y) = Cov_h(x, y)$.

In the Fourier domain, the ADSN process is easily defined since the convolution operator is given by a pointwise multiplication. It is known that a Gaussian white noise image has a uniform independent random phase and its Fourier modulus is an uncorrelated Rayleigh noise. Thus the the phase of the obtained ADSN is a uniform random whereas its Fourier modulus is the pointwise multiplication of the Fourier modulus of the spot h by a Rayleigh noise.

2.4 Random phase noise model (RPN)

The random phase noise model has been introduced as a stationary texture synthesis technique by [44]. The idea consists in obtaining a texture from a given Fourier magnitude (e.g., obtained from a texture example or trough parametric model) by setting the phase as (uniform) random [45]. For a given real-valued image u , the associated RPN representation is defined by a random image with the same Fourier module as u and a random phase θ . As the random part θ of the RPN is constrained to be a Fourier phase (angle) of a real-valued image, it must satisfy specific conditions. Begin by recalling that the Fourier transform of a real-valued image involves a complex conjugate symmetry (i.e., $\hat{u}(-k) = \hat{u}^*(k)$). It follows that the phase is an odd function of the frequency. In practice, it is often convenient to simply generate a realization of a Gaussian white noise and then to consider its phases.

Since the RPN is by nature defined in the Fourier domain, it is easy to compare it with the ADSN process. The Fourier modulus of the RPN is by definition equal to the Fourier modulus of the spot h while the Fourier modulus of the ADSN process are the same modulus degraded by a pointwise multiplication by a white Rayleigh noise [2].

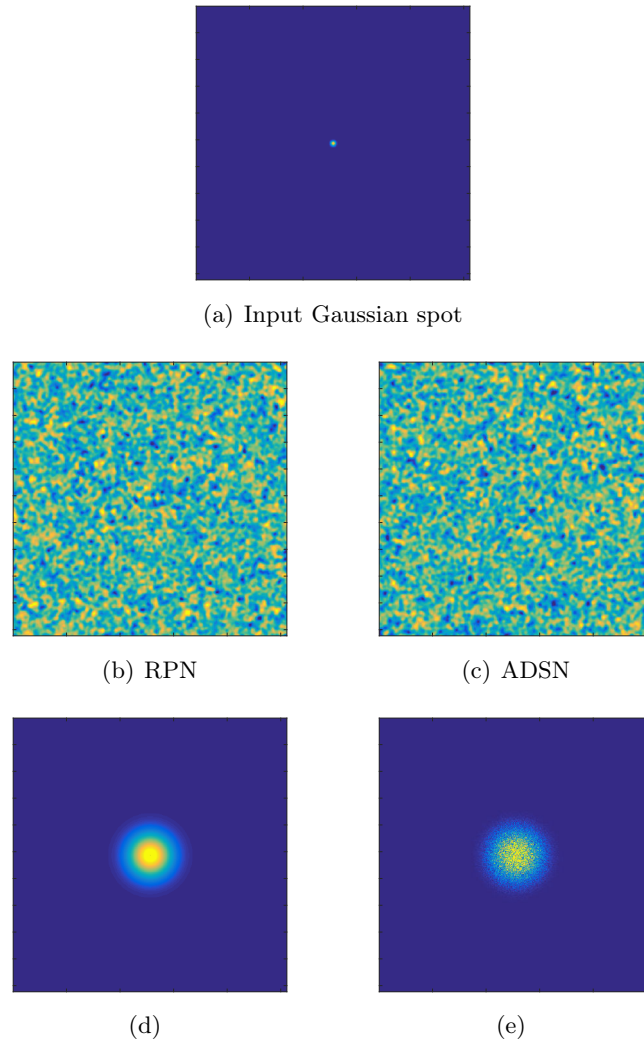


Figure 2.2: Differences between the outcomes of the RPN and the ADSN associated with a Gaussian spot (a). (b) RPN outcome and (c) ADSN simulation. The Fourier modulus of the various simulations are represented in (d) and (e) and. Let us point out that the modulus of the ADSN is the pointwise multiplication of the modulus of RPN by a white Rayleigh noise.

2.5 Multivariate extension

A natural question to ask is whether the models and related results that we have presented in the previous sections extend naturally to the multivariate framework. Such a multivariate framework is of interest for the multivariate (e.g., colour or multispectral) texture simulation, as well as application to multiscale image decomposition as investigated in Chapter 6. Our goal here is to generate a vector of textures while preserving the covariance structure of each image as well as its cross-covariance with all the rest of images.

In the context of color texture synthesis, [2] addresses a multivariate extension of the RPN and ADSN algorithms. The color ADSN process is obtained by convolving each color channel with the same realization of a Gaussian white noise. While the RPN is defined by adding the same random phase to the phase of each color channel of the vector spot. One can easily verify that the covariance and cross-covariance structures for the different color channels are preserved with these two multivariate extensions. Convincing synthesis results are reported for color textures. In [46, 47], a compact formulations are proposed using the so-called "Texton". In our application context to ocean remote sensing data, these two formulations involve a critical limitation. They assume that a multivariate spot image is available. The synthesis procedures cannot straightforwardly extended to partially-observed images. Ocean remote sensing data typically involve missing data and land mask, such that the derivation of reference multivariate spots may be an issue. We also aim at guaranteeing the interpretability of the considered representative in terms of covariance and cross-covariance models. Hence, we follow in this thesis the framework considered in [27] for the multivariate SPDE processes. It relies on a system of equations, and we adapt it to the case of ADSN and RPN processes. The resulting formulation does not impose the same noise for each channel. The associated matrix-valued representation of the system may be parametrized by the covariances and cross-covariances of the sample vector images, which can be derived from partially-observed as well as irregularly-sampled images. Besides these parametric extensions, applications to the joint analysis of multi-source and multi-resolution remote sensing data, with possibly only partially overlapping spatial supports, may also be considered for instance for the interpolation of high-resolution sea surface geophysical fields.

In this section, we explore the proposed multivariate RPN and ADSN models. The texture synthesis algorithms used in Chapter 6 are based on these results.

2.5.1 Multivariate RPN

In this section we analyze the multivariate random phase noise (MRPN). We will use this process as a mean to synthesize multivariate stationary textures with expected spectral properties.

Definition 1. The multivariate RPN associated with a vector-valued image $h = (h_1, h_2, \dots, h_n)$ is a random vector-valued image $g = (g_1, g_2, \dots, g_n)$ obtained using a vector of independent uniform random phase $\theta = (\theta_1, \dots, \theta_n)$ by the following

system

$$\begin{pmatrix} \hat{g}_1(\xi) \\ \hat{g}_2(\xi) \\ \vdots \\ \hat{g}_n(\xi) \end{pmatrix} = \left[\mathcal{L}_{ij}(h) \right]_{1 \leq i, j \leq n} \begin{pmatrix} e^{i\theta_1(\xi)} \\ e^{i\theta_2(\xi)} \\ \vdots \\ e^{i\theta_n(\xi)} \end{pmatrix} \quad (2.10)$$

Such that $\mathcal{S}_g(\xi) = \mathcal{S}_h(\xi)$.

where $\mathcal{L}_{ij}(h)$ are matrix-valued operators which only depend on the vector-valued image h . \mathcal{S}_g and \mathcal{S}_h denote respectively the power spectrum matrix of the vector-valued images h and g .

Under this definition, the MRPN associated with a vector-valued image depends on the spectra and cross-spectra of this vector. This definition embeds the case where $n=1$. Another trivial case consists of identically zero matrix-valued operators for $i \neq j$. In this case, we define the univariate RPN associated to a vector-valued image h as a vector-valued image obtained by replacing the phase of the discrete Fourier transform (DFT) of each component of h by a different realization of random uniform phase.

Theorem 1. (*Simulation of the MRPN*). Let $\mathcal{W} = (\mathcal{W}_1, \dots, \mathcal{W}_n)$ be a vector of independent Gaussian white noise constrained such that their Fourier modulus are set to unity. Let $\mathcal{L}(h) = \{\mathcal{L}_{ij}(h), 1 < i, j \leq n\}$ be matrix-valued operators related to spectra and cross spectra of the vector-valued image h . Under a judicious choice of $\mathcal{L}(h)$, the solution of the following system of equations

$$\begin{pmatrix} \hat{g}_1 \\ \hat{g}_2 \\ \vdots \\ \hat{g}_n \end{pmatrix} = \begin{pmatrix} \mathcal{L}_{11}(h) & \mathcal{L}_{12}(h) & \cdots & \mathcal{L}_{1n}(h) \\ \mathcal{L}_{21}(h) & \mathcal{L}_{22}(h) & \cdots & \mathcal{L}_{2n}(h) \\ \vdots & \vdots & \ddots & \vdots \\ \mathcal{L}_{n1}(h) & \mathcal{L}_{n2}(h) & \cdots & \mathcal{L}_{nn}(h) \end{pmatrix} \begin{pmatrix} \hat{\mathcal{W}}_1 \\ \hat{\mathcal{W}}_2 \\ \vdots \\ \hat{\mathcal{W}}_n \end{pmatrix} \quad (2.11)$$

is the MRPN associated with h .

For the proof of theorem, we will focus on the construction of the trivariate system of RPN i.e., $n=3$. To simplify the system (2.11), we shall consider lower triangular matrix by setting $\mathcal{L}_{12}(h) = \mathcal{L}_{23}(h) = \mathcal{L}_{31}(h) = 0$. In this case, the system of RPNs in the spectral domain becomes

$$\begin{pmatrix} \hat{g}_1 \\ \hat{g}_2 \\ \hat{g}_3 \end{pmatrix} = \begin{pmatrix} \mathcal{L}_{11}(h) & 0 & 0 \\ \mathcal{L}_{21}(h) & \mathcal{L}_{22}(h) & 0 \\ \mathcal{L}_{31}(h) & \mathcal{L}_{32}(h) & \mathcal{L}_{33}(h) \end{pmatrix} \begin{pmatrix} \mathcal{W}_1 \\ \mathcal{W}_2 \\ \mathcal{W}_3 \end{pmatrix} \quad (2.12)$$

and the solution $g = (g_1, g_2, g_3)^T$ (after an inverse Fourier transform) to this system of equations is a trivariate RPN textures. One can make (2.12) on the following compact form

$$\hat{g}(\xi) = \mathcal{L}(h)\hat{\mathcal{W}} \quad (2.13)$$

Our aim is to find a way to compute all the components of $\mathcal{L}(h)$ to directly target the spectral and cross-spectral characteristics of the vector-valued image h . Direct calculations exploiting (2.13) show that

$$\mathcal{S}_g(\xi) = \mathbf{E}(\hat{g}\hat{g}^H) \quad (2.14)$$

$$= \mathcal{L}(h)\mathbf{E}(\hat{\mathcal{W}}\hat{\mathcal{W}}^H)\mathcal{L}(h)^H \quad (2.15)$$

$$= \mathcal{L}(h)\mathcal{S}_{\mathcal{W}}(\xi)\mathcal{L}(h)^H \quad (2.16)$$

where $\mathcal{L}(h)^H$ denotes the Hermitian of the operator matrix $\mathcal{L}(h)$, $\mathcal{S}_{\mathcal{W}}(\xi)$ is the power spectrum of the noise processes. Since this noise processes are mutually independent, $\mathcal{S}_{\mathcal{W}}(\xi)$ is a block diagonal matrix and can be written in a compact form as

$$\mathcal{S}_{\mathcal{W}}(\xi) = \text{diag}(\mathcal{S}_{\mathcal{W}_1}(\xi), \mathcal{S}_{\mathcal{W}_2}(\xi), \mathcal{S}_{\mathcal{W}_3}(\xi)) \quad (2.17)$$

Moreover, the noise processes are white with Fourier modulus equals to unity. A direct computation shows that $\mathcal{S}_{\mathcal{W}_i}(\xi) = \mathbf{1}$ ($\forall i = 1 \dots 3$), where $\mathbf{1}$ is the image whose components are all equal to 1.

We can now develop the system of equations (2.16) taking into account the above observations. We resort to the following matrix-based system

$$\mathcal{S}_g(\xi) = \begin{pmatrix} \mathcal{L}_{11}\mathcal{L}_{11}^* & \mathcal{L}_{11}\mathcal{L}_{21}^* & \mathcal{L}_{11}\mathcal{L}_{31}^* \\ \mathcal{L}_{21}\mathcal{L}_{11}^* & \mathcal{L}_{21}\mathcal{L}_{21}^* + \mathcal{L}_{22}\mathcal{L}_{22}^* & \mathcal{L}_{21}\mathcal{L}_{31}^* + \mathcal{L}_{22}\mathcal{L}_{32}^* \\ \mathcal{L}_{31}\mathcal{L}_{11}^* & \mathcal{L}_{31}\mathcal{L}_{21}^* + \mathcal{L}_{32}\mathcal{L}_{22}^* & \mathcal{L}_{31}\mathcal{L}_{31}^* + \mathcal{L}_{32}\mathcal{L}_{32}^* + \mathcal{L}_{33}\mathcal{L}_{33}^* \end{pmatrix} \quad (2.18)$$

As we have already noted, our goal is to relate each component of the right-hand side of (2.18) to the cross-spectral matrix of the initial vector image h . It is achieved by imposing the following equality

$$\mathcal{S}_g(\xi) = \mathcal{S}_h(\xi) \quad (2.19)$$

This is equivalent to resolve the following system

$$\mathcal{L}_{11}\mathcal{L}_{11}^* = \hat{h}_{11}\hat{h}_{11}^* \quad (2.20)$$

$$\mathcal{L}_{21}\mathcal{L}_{11}^* = \hat{h}_{21}\hat{h}_{21}^* \quad (2.21)$$

$$\mathcal{L}_{31}\mathcal{L}_{11}^* = \hat{h}_{31}\hat{h}_{31}^* \quad (2.22)$$

$$\mathcal{L}_{21}\mathcal{L}_{21}^* + \mathcal{L}_{22}\mathcal{L}_{22}^* = \hat{h}_{22}\hat{h}_{22}^* \quad (2.23)$$

$$\mathcal{L}_{21}\mathcal{L}_{31}^* + \mathcal{L}_{22}\mathcal{L}_{32}^* = \hat{h}_{23}\hat{h}_{23}^* \quad (2.24)$$

$$\mathcal{L}_{31}\mathcal{L}_{31}^* + \mathcal{L}_{32}\mathcal{L}_{32}^* + \mathcal{L}_{33}\mathcal{L}_{33}^* = \hat{h}_{33}\hat{h}_{33}^* \quad (2.25)$$

where $\hat{h}_{ij} = \mathcal{F}(h_{ij})$ is the Fourier transform of the vector-valued image h .

Using (2.21) and proceeding by recursive substitutions, the solutions of this system

of equations is given by

$$\mathcal{L}_{11} = \hat{h}_{11} \tag{2.26}$$

$$\mathcal{L}_{21} = \frac{\hat{h}_{21}\hat{h}_{21}^*}{\hat{h}_{11}} \tag{2.27}$$

$$\mathcal{L}_{31} = \frac{\hat{h}_{31}\hat{h}_{31}^*}{\hat{h}_{11}} \tag{2.28}$$

$$\mathcal{L}_{22}\mathcal{L}_{22}^* = \hat{h}_{22}\hat{h}_{22}^* - \frac{\hat{h}_{21}\hat{h}_{21}^*}{\hat{h}_{11}} \left(\frac{\hat{h}_{21}\hat{h}_{21}^*}{\hat{h}_{11}} \right)^* \tag{2.29}$$

$$\mathcal{L}_{32}^* = \frac{\hat{h}_{23}\hat{h}_{23}^* - \mathcal{L}_{21}\mathcal{L}_{31}^*}{\mathcal{L}_{22}^*} \tag{2.30}$$

$$\mathcal{L}_{33}\mathcal{L}_{33}^* = \hat{h}_{33}\hat{h}_{33}^* - \mathcal{L}_{31}\hat{\mathcal{L}}_{31}^* - \mathcal{L}_{32}\mathcal{L}_{32}^* \tag{2.31}$$

This completes the proof of Theorem 1 for the trivariate case. The extension to greater values of n follows from the same principles.

2.5.2 Multivariate ADSN

Similar arguments to those used above to define and characterize the multivariate RPN can be used to extend the ADSN process to the multivariate case. One of the facts we learned about the (univariate) ADSN process was that if the spot h has the autocovariance of the form $Cov_h(x, y)$ then the associated ADSN process is completely defined by the random Gaussian process $\mathcal{N}(0, Cov_h(x, y))$.

Definition 2. Let $\mathbb{H} = (h_1, h_2, \dots, h_n)$ be a vector of spot functions. The multivariate asymptotic discrete spot noise (MADSN) associated with \mathbb{H} is the multi-normal distribution $\mathcal{N}(0, \mathbb{C}_{\mathbb{H}})$ with

$$\mathbb{C}_{\mathbb{H}} = \begin{pmatrix} \mathbb{C}(h_1, h_1) & \mathbb{C}(h_1, h_2) & \cdots & \mathbb{C}(h_1, h_n) \\ \mathbb{C}(h_2, h_1) & \mathbb{C}(h_2, h_2) & \cdots & \mathbb{C}(h_2, h_n) \\ \vdots & \vdots & \ddots & \vdots \\ \mathbb{C}(h_n, h_1) & \mathbb{C}(h_n, h_2) & \cdots & \mathbb{C}(h_n, h_n) \end{pmatrix} \tag{2.32}$$

By analogy with the univariate ADSN process, the simulation of the MADSN can be obtained by a spatial filtering of a vector of noise images. We show in the subsequent that the MADSN associated with a vector of spots $\mathbb{H} = (h_1, h_2, \dots, h_n)$ can be simulated as a system of convolution processes between normalized spot vector and a vector of realizations of independent Gaussian white noises.

Theorem 2. (*Simulation of MADSN*). Let $\mathcal{W} = (\mathcal{W}_1, \dots, \mathcal{W}_n)^T$ be a vector of independent Gaussian white noises. Let $\bar{\mathbb{H}}$ be the normalized zero-mean copy of \mathbb{H} . Then there exists a family of functions $\{f_{ij}\}_{1 \leq i, j \leq n}$ such that the random multivariate image

$$(f_{ij}\bar{\mathbb{H}})_{1 \leq i, j \leq n} * \mathcal{W} \tag{2.33}$$

is the MADSN associated with \mathbb{H} (i.e., has the same multi-normal distribution defined in (2.32)).

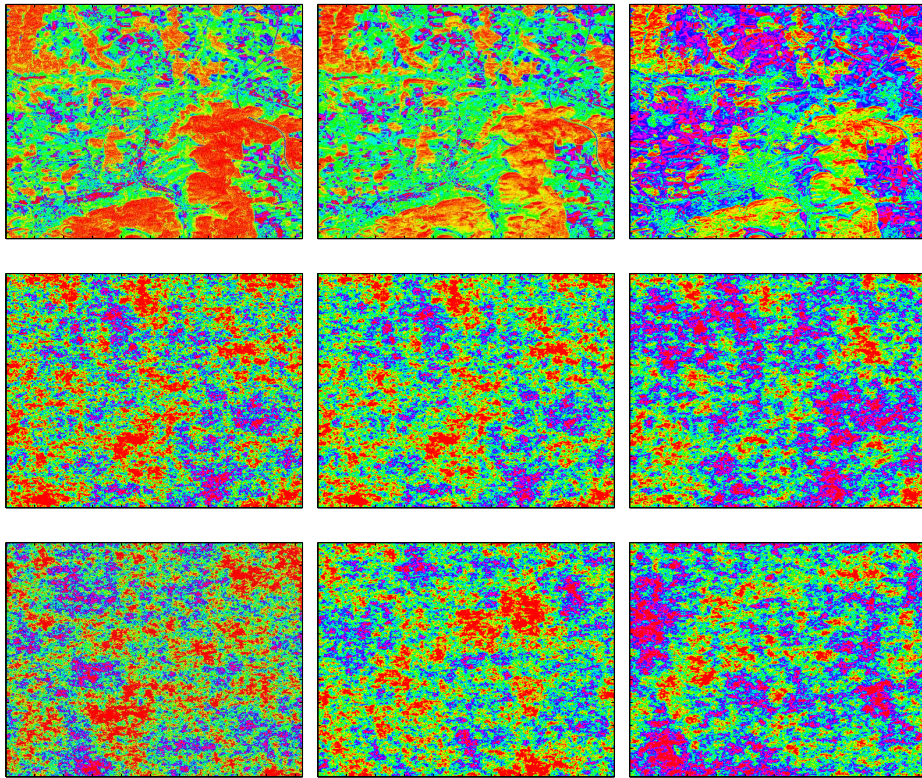


Figure 2.3: Example of correlated texture-like satellite images provided by the multispectral LANDSAT 7 ETM sensor and sampled respectively with channels 2,3,4 (first row). The outcome of the trivariate RPN algorithm is displayed in the second row. Independent simulations using the univariate RPN model of the three image are shown in the third row. The trivariate model aims at reproducing the autocorrelations and cross correlations of the three texture samples.

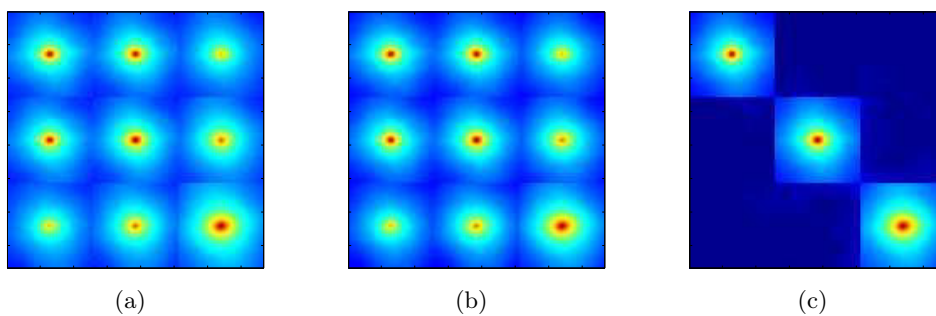


Figure 2.4: Comparison between the autocorrelation and cross-correlations obtained from (a) the input texture sample, (b) from the trivariate RPN outcome and (c) from images depicted in (Fig.2.3 third row).

Proof. We proceed similarly to the MRPN and consider the trivariate case (i.e., $n = 3$) and limit ourselves to a lower triangular block matrices in (2.33). In this case, (2.33) is reduced to

$$\begin{pmatrix} g_1 \\ g_2 \\ g_3 \end{pmatrix} = \begin{pmatrix} f_{11}(h) & 0 & 0 \\ f_{21}(h) & f_{22}(h) & 0 \\ f_{31}(h) & f_{32}(h) & f_{33}(h) \end{pmatrix} * \begin{pmatrix} \mathcal{W}_1 \\ \mathcal{W}_2 \\ \mathcal{W}_3 \end{pmatrix} \quad (2.34)$$

Notice that our goal here is to obtain an explicit representations for the family of functions $\{f_{ij}\}_{1 \leq i, j \leq n}$ so that we have

$$g \sim \mathcal{N}\left(\mathbf{0}, \begin{pmatrix} \mathbb{C}(h_1, h_1) & \mathbb{C}(h_1, h_2) & \mathbb{C}(h_1, h_3) \\ \mathbb{C}(h_2, h_1) & \mathbb{C}(h_2, h_2) & \mathbb{C}(h_2, h_3) \\ \mathbb{C}(h_3, h_1) & \mathbb{C}(h_3, h_2) & \mathbb{C}(h_3, h_3) \end{pmatrix}\right) \quad (2.35)$$

where $\mathbb{C}(h_i, h_j) = h_i * h_j$.

The system (2.34) can be written as

$$\begin{cases} g_1 &= f_{11}(\hat{\mathbb{H}}) * \mathcal{W}_1 \\ g_2 &= f_{21}(\hat{\mathbb{H}}) * \mathcal{W}_1 + f_{22}(\hat{\mathbb{H}}) * \mathcal{W}_2 \\ g_3 &= f_{31}(\hat{\mathbb{H}}) * \mathcal{W}_1 + f_{32}(\hat{\mathbb{H}}) * \mathcal{W}_2 + f_{33}(\hat{\mathbb{H}}) * \mathcal{W}_3 \end{cases} \quad (2.36)$$

We can easily check two properties: i) the vector-valued image g is Gaussian, and ii) $\mathbb{E}(g) = \mathbf{0}$. All this comes from the fact that the noise processes are centered Gaussian processes and from the fact that the convolution product is linear which preserves the Gaussianity. To complete the proof, we need to determine the expression of the covariance structure of g .

$$\mathbb{C}(g_1, g_1) = \mathbb{E}([f_{11} * \mathcal{W}_1][f_{11}(\hat{\mathbb{H}}) * \mathcal{W}_1]) \quad (2.37)$$

$$= \mathbb{E}\left(\left[\sum_{u \in \Omega} f_{11}(u-x)\mathcal{W}_1(u)\right]\left[\sum_{v \in \Omega} f_{11}(v-y)\mathcal{W}_1(v)\right]\right) \quad (2.38)$$

$$= \sum_{u \in \Omega} f_{11}(u-x)f_{11}(u-y) \quad (2.39)$$

$$= f_{11} * f_{11} \quad (2.40)$$

$$\mathbb{C}(g_2, g_1) = \mathbb{E}([f_{21} * \mathcal{W}_1 + f_{22} * \mathcal{W}_2][f_{11}(\hat{\mathbb{H}}) * \mathcal{W}_1]) \quad (2.41)$$

$$= \mathbb{E}([f_{21} * \mathcal{W}_1][f_{11} * \mathcal{W}_1] + [f_{22} * \mathcal{W}_1][f_{11} * \mathcal{W}_2]) \quad (2.42)$$

$$= f_{21} * f_{11} \quad (2.43)$$

In the same way, one can prove the following formulas

$$\mathbb{C}(g_3, g_1) = f_{31} * f_{11} \quad (2.44)$$

$$\mathbb{C}(g_2, g_2) = f_{21} * f_{21} + f_{22} * f_{22} \quad (2.45)$$

$$\mathbb{C}(g_3, g_2) = f_{31} * f_{21} + f_{32} * f_{22} \quad (2.46)$$

$$\mathbb{C}(g_3, g_3) = f_{31} * f_{31} + f_{32} * f_{32} + f_{33} * f_{33} \quad (2.47)$$

We now have everything we need to develop explicit formulas for $[f_{ij}]_{1 \leq i, j \leq 3}$. Similarly to the proof of Theorem 2.11, we shall compare each term of the covariance matrix (2.35) with those calculated using the system (2.36). We begin with the observation that the solution of the first equation is trivial

$$f_{11} * f_{11} = \bar{h}_{11} * \bar{h}_{11} \quad (2.48)$$

and one can impose $f_{11} = \bar{h}_{11}$. From the substitution of these terms in (2.44) and (2.45), the inverse Fourier transform leads to

$$f_{21} = \mathcal{F}^{-1} \frac{\hat{h}_{21}^2}{\hat{h}_{11}} \quad (2.49)$$

$$f_{31} = \mathcal{F}^{-1} \frac{\hat{h}_{31}^2}{\hat{h}_{11}} \quad (2.50)$$

A similar computations shows that

$$f_{22} = \mathcal{F}^{-1} \sqrt{\hat{h}_{22}^2 - \hat{f}_{21}^2} \quad (2.51)$$

$$f_{32} = \mathcal{F}^{-1} \frac{\hat{h}_{32}^2 - \hat{f}_{31} \hat{f}_{21}}{\hat{f}_{22}} \quad (2.52)$$

$$f_{33} = \mathcal{F}^{-1} \sqrt{\hat{h}_{33}^2 - \hat{f}_{31}^2 - \hat{f}_{32}^2} \quad (2.53)$$

Hence, using this family of functions $\{f_{i,j}\}_{i,j}$, g exhibits the expected covariance structure, which completes the proof for the trivariate case. The extension to the n -variate case follows from the same development.

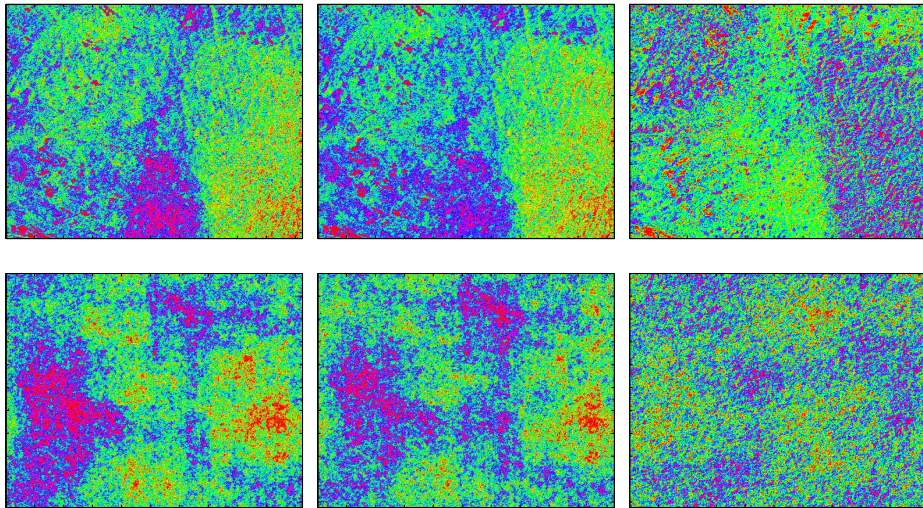


Figure 2.5: Example of the outcome of the trivariate ADSN algorithm. The input images (first row) are texture-like satellite snapshots provided by LANDSAT 8 and taken respectively from channels 1,2 and 5.

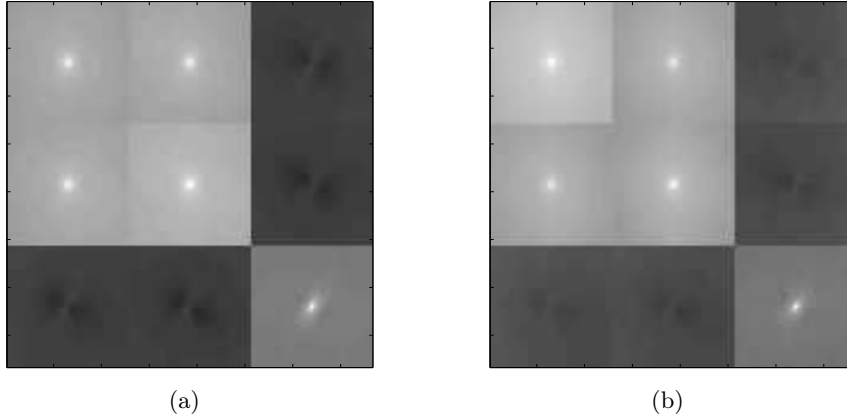


Figure 2.6: Demonstration of the capability of the trivariate ADSN model to produce the correlation and cross correlation of the sample vector images. (a) sample-based kernels (b) Outcomes of the MASN algorithm.

2.5.3 Differences between the MRPN and MADSN

The comparison of the two considered processes is simpler in the univariate case. Given a spot image h the difference of the outcomes of the models lie only in the modulus of their Fourier transforms. As already mentioned, the Fourier magnitudes of the ADSN process are corrupted by a multiplicative Rayleigh white noise. In the case of multivariate models, we will follow the manner in which we have constructed the two processes. In particular, we will rely on equations (2.12) and (2.35). The MADSN is obtained by a point-wise multiplication of each Fourier modulus of terms in the summation (2.12) by a Rayleigh white noise. Given the fact that the matrices are triangular, the difference between the first component of the vector-valued MRPN and MADSN resorts to the univariate case (Fig.2.7). No such direct correspondence can be derived for the other components.

2.6 Parametric representations and associated SPDE-based formulations

We want to address parametric representations of the different models considered in this chapter. In view of the definitions of the univariate (resp. multivariate) RPN and ADSN models in the spectral domain, one can select appropriate parametric models for the power spectrum (resp. cross power spectrum). This selection may be based on a prior knowledge (e.g., Fitting a model to a sample). In the spatial domain, this is equivalent to select appropriate models for the covariance (resp. cross covariance) kernels. In this section we briefly present an important class of the parametric forms of covariance functions which can be associated to a solution of certain SPDE equations.

As a starting point, we recall the definition of the ADSN process presented in section

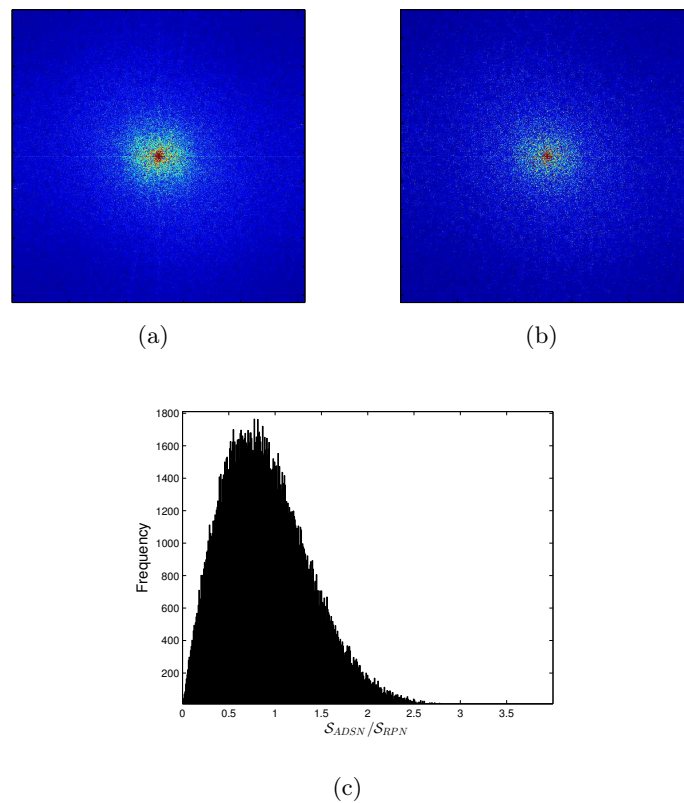


Figure 2.7: Difference between the MRPN and MADSN processes. The Fourier modulus of the first component of the vector image simulated using (a) the MRPN and (b) MADSN algorithm. The modulus of the MADSN is the pointwise multiplication of the modulus of MRPN by (c) a white Rayleigh noise.

2.3 as the spatial convolution of a spot function with a Gaussian white noise

$$X(s) = \mathcal{G}(s) * \mathcal{W}(s) \quad (2.54)$$

It follows by taking the Fourier transform of both sides of the above equation that

$$\hat{X}(k) = \hat{\mathcal{G}}(k)\hat{\mathcal{W}}(k) \iff \hat{\mathcal{G}}^{-1}(k)\hat{X}(k) = \hat{\mathcal{W}}(k) \quad (2.55)$$

$$\iff \hat{\mathcal{L}}(k)\hat{X}(k) = \hat{\mathcal{W}}(k) \quad (2.56)$$

$$\iff \mathcal{L}(s) * X(s) = \mathcal{W}(s) \quad (2.57)$$

If the matrix-valued function \mathcal{L} can be written as operator-valued (pseudo) differential operators, one can rewrite (2.57) as an SPDE

$$\mathcal{L}X(s) = \sigma\mathcal{W}(s) \quad (2.58)$$

where \mathcal{L} is a given (pseudo) linear differential operator, \mathcal{W} is white Gaussian noise and σ is the variance parameter.

All the main results established for the ADSN processes are valid for the SPDEs and drive from the same principles using the duality between (2.58) and (2.54).

The Matérn covariance model and its SPDE representation. We study a special parametric class of (2.58). Namely, the Matérn class of SPDE. Before giving the explicit formulas of the associated operator \mathcal{L} , we introduce the Matérn family of covariance function models. This family is very popular in environmental statistics [48]. The Matérn covariance function has a shape parameter ν , a scale parameter κ , and variance parameter, σ^2 , and can be parametrized as:

$$C(\vec{h}) = \frac{2^{1-\nu}\sigma^2}{(4\pi)^{d/2}\Gamma(\nu + d/2)\kappa^{2\nu}}(\kappa\|\vec{h}\|)K_\nu(\kappa\|\vec{h}\|) \quad (2.59)$$

where K_ν is the modified Bessel function of the second kind of order $\nu > 0$. Special cases resort to a Gaussian and exponential covariance models.

One can analytically establish processes associated with the Matérn covariance family and their SPDE representations. More precisely, as detailed in [49], every centered Gaussian process with a continuous Matérn covariance function has a representation of the form:

$$(\kappa - \Delta)^{\alpha/2}X(s) = \sigma\mathcal{W}(s) \quad (2.60)$$

where $\alpha = \nu/2 - 1/2$. The proof of this result relies on the theory of the pseudo-differential operators and their related spectral representation. We may refer the reader to Samko et al [50] which provides an excellent and remarkably readable treatment of the topic. The fractional operator in (2.60) reduces by Fourier transforms to multiplication by the power $(\kappa + \|k\|)^{\alpha/2}$. Rather interestingly, explicit formula for the inverse Fourier transform of its inverse are also established. This gives us the analytic form of the associated convolution operator \mathcal{G} in (2.54), which is one of the rather interesting aspects of the class of Matérn family.

$$\mathcal{G}(h) = \mathcal{F}^{-1}(1/\hat{\mathcal{L}}_{\kappa,\nu,\sigma}) = \mathcal{C}_{(\kappa,\nu/2-1/2,\sqrt{\sigma})}(h) \quad (2.61)$$

where \mathcal{C} is a Matérn-like covariance function. In addition to this result, one may be tempted to conclude that

$$\mathcal{C}_{(\kappa,\alpha,\kappa,\sigma)} = \mathcal{C}_{(\kappa,\nu/2-1/2,\sqrt{\sigma})} * \mathcal{C}_{(\kappa,\nu/2-1/2,\sqrt{\sigma})} \quad (2.62)$$

This is another result from [50]. Recall that we already know from the above sections that the autocovariance function of random field is just an auto-convolution of the associated spot kernel. The Matérn example is the only case, to our knowledge, when such analytic correspondence is known.

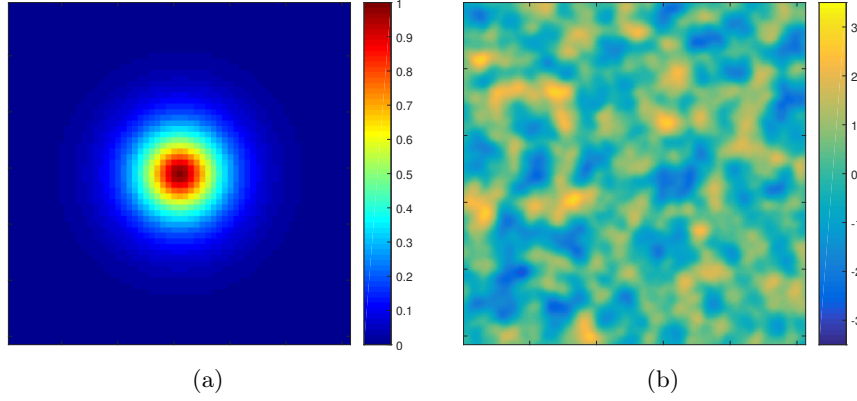


Figure 2.8: (a) Isotropic Matérn covariance function obtained from model (2.59), (b) Realizations of random field with the covariance function shown in (a)

Various extensions. The Matérn covariance function considered in (2.59) is isotropic and involves circular constant-correlation contours. One can extend such functional to account for locally anisotropic image features. The simplest method to perform this extension consists in applying a linear transformation (shear and rotation) to the coordinates system of the standard isotropic Matérn kernel. Such covariance kernels result in elliptical constant-correlation contours. Formally, it resorts to applying the following transformation to the original coordinate system:

$$\begin{bmatrix} x' \\ y' \end{bmatrix} = \begin{bmatrix} 1 & 0 \\ 0 & R \end{bmatrix} \begin{bmatrix} \cos \theta & -\sin \theta \\ \sin \theta & \cos \theta \end{bmatrix} \times \begin{bmatrix} x \\ y \end{bmatrix} \quad (2.63)$$

where R is the anisotropy ratio, θ is the orientation of the principal axis. Notice that the correlation length along the principal axis is controlled by parameter κ in (2.59).

Given a texture sample X , under the assumption that model (2.58) holds, model parameters can be estimated directly from this sample. A non-parametric approach for the identification of the anisotropic correlations in spatially-sampled datasets is developed in [51]. The calibration framework focuses on the so-called Covariance Hessian Matrix (CHM) defined, for differentiable covariance model, as follows:

$$H_{ij}(r) = -\frac{\partial^2 C(r)}{\partial r_i \partial r_j}, \quad i, j = 1, 2 \quad (2.64)$$

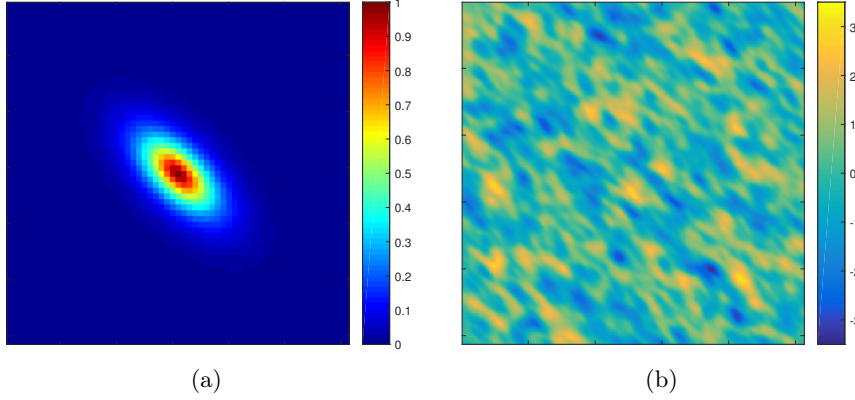


Figure 2.9: Anisotropic Matérn covariance function obtained by applying the transformation (2.63) to the covariance function shown in Fig.2.8(a) with $R = 1/2$ and $\theta = \pi/4$, (b) A realization of random field with the given covariance function.

We determine the parameters of geometric anisotropy from the analysis of the expectation of the Gradient Kronecker Product:

$$Q_{ij}(r) = E(\partial_i X(s) \partial_j X(s)) \quad (2.65)$$

with E denoting statistical expectation.

Swerling has proved in [52] that the Covariance Hessian Matrix (CHM) is related to the expectation of the Gradient Kronecker product (Q) by the following equation:

$$H_{ij}(r)|_{r=0} = Q_{ij} \quad (2.66)$$

The CHM $H_{i,j}^*(0)$, evaluated at zero lag, in the principal coordinate system is a diagonal matrix given by

$$H_{i,j}^*(r)|_{r=0} = -\frac{\delta_{ij}}{2\xi_i\xi_j} \Delta \tilde{C}(0) \quad (2.67)$$

where $\Delta \tilde{C}(0) = \sum_{i=1}^2 \delta^2 \tilde{C}(0) / \delta r_i^2$ is the Laplacian of the isotropic covariance function $\tilde{C}(r)$ evaluated at zero lag. This function is obtained by rotation and rescaling of the axes. The ξ_i, ξ_j ($i, j = 1, 2$) are the correlation lengths in the respective principal directions and δ_{ij} is the Kronecker delta function, defined by $\delta_{ij} = 1$, if $i = j$ and $\delta_{ij} = 0$ for $i \neq j$.

Our numerical scheme is based on the diagonalization of the CHM, where the latter is estimated from the sample by means of \hat{Q} using (2.65). Then, the square roots of the eigenvalues ratio correspond to the anisotropic ratio, while the orientation angles can be obtained from the elements of the diagonalizing transformation matrix. More precisely, we have

$$\hat{R} = \sqrt{Q_{11}^* / Q_{22}^*} \quad (2.68)$$

This approach can be extended to the estimation of the fractional exponent α , associated with the fractal dimension of the field. This parameter, usually hard to estimate from a sample, may provides an additional degree of freedom to constrain the spectral density of the generated field.

Despite this method is very fast and efficient for texture synthesis thanks to Fast Fourier Transforms (FFT), it only accounts for stationary fields and the definition of non-stationary and conditional versions might not be straightforward. The relatively intuitive idea to introduce non-stationary version where the parameters of the SPDE (2.58) may spatially vary. One can investigate different options to state these parameter fields. A conditional setting w.r.t. an external field may be considered. The resolution of the non-stationary SPDEs is then implemented as a non-stationary convolution similar to (2.54) with locally-varying kernels. We report in Fig.2.10 synthetic examples of non-stationary fields by varying the parameters of (2.8). We applied such models to the super-resolution of SST fields in [28]. However, such models were experimentally proven difficult to parameterize with respect to expected global features, which motivates the alternatives considered in Chapter 3 & 6.

To conclude this section about SPDEs, notice that in the same way we defined the multivariate ADSN processes, the equivalent multivariate forms of SPDE equations were studied in [27].

2.7 Conclusion

In this chapter we have presented some approaches of texture synthesis based on spectral constraints. We have showed how it is possible to extend the considered models to the multivariate framework using system of equations. As demonstrated in the experimentation sections, these models allow us to impose cross spectrum constraints on the synthesis. SPDE-based formulations and associated possible parametrizations are also discussed in the last section of this Chapter.

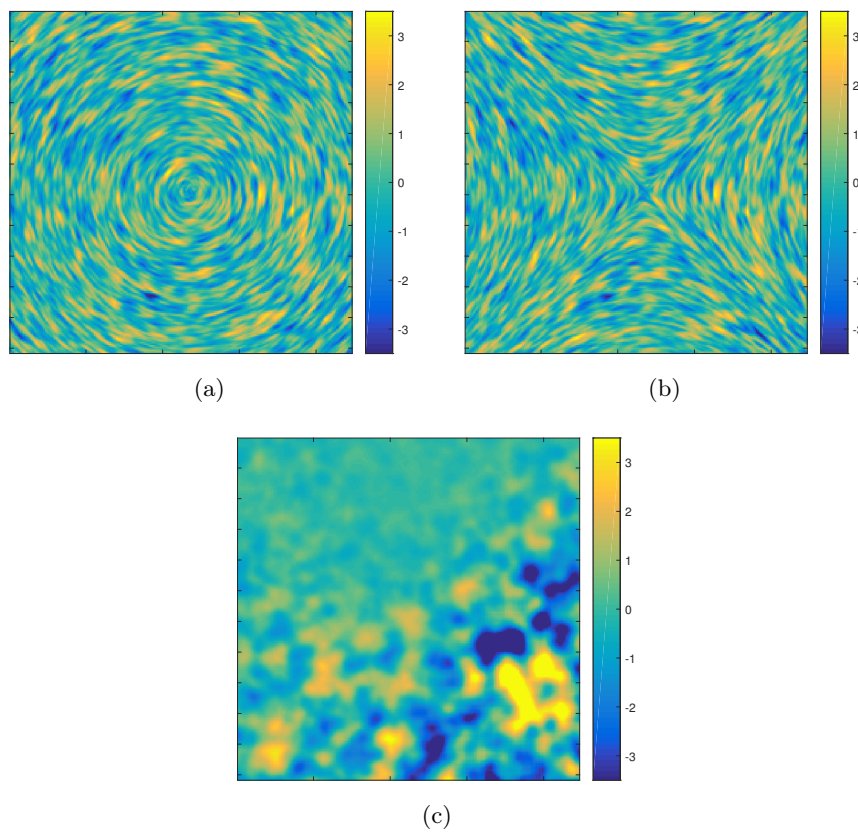


Figure 2.10: Texture synthesis using non-stationary SPDEs for different geometrical patterns: (a) rotational and (b) hyperbolic orientation field using a constant parameters for α , κ , σ and R . The texture in (c) is obtained by (smoothly) jointly varying κ and σ parameters of an isotropic covariance model.

Superresolution of Textured images using stochastic models and a Novel Fourier domain constraint Phase

Contents

2.1 Introduction	29
2.1.1 The texture synthesis problem	29
2.1.2 Previous work (Parametric and non-parametric approaches)	30
2.1.3 Contribution of the Chapter	31
2.2 Shot (Spot) noise model	31
2.3 ADSN	32
2.4 Random phase noise model (RPN)	33
2.5 Multivariate extension	35
2.5.1 Multivariate RPN	35
2.5.2 Multivariate ADSN	38
2.5.3 Differences between the MRPN and MADSN	42
2.6 Parametric representations and associated SPDE-based formulations	42
2.7 Conclusion	47

Abstract We present a method for multi-scale exemplar-based texture modeling and synthesis using spectral texture priors, namely the Random phase noise (RPN) and the ADSN processes. The targeted application is the super-resolution of textured images. These images exhibit different statistical and spectral characteristics. Existing algorithms based on stationary models do not produce realistic results in the case of highly-structured textures. A cascade scheme, formulated in the Fourier domain, is proposed. This scheme is based on learning the spectrum magnitude from a sample while the phase is extracted and imposed from the low resolution image. The proposed methodology is demonstrated using various texture samples.

3.1 Introduction

Super-resolution is the process of estimating a high-resolution image from a low-resolution input by recovering or inventing realistic high-frequency image information [53, 54]. It has received great attention over the last few years in the image processing field as well as in the different application-oriented contexts (e.g., medical images, geophysical remote sensing...). One of the most difficult aspect of the super-resolution of the textured images is the ability to deal, at the same time, with small-scale oscillations areas and the low-frequency regular patterns (i.e., edges) using a single model.

Super-resolution is also known to belong to the family of ill-posed inverse problems. To restrict the vast set of all possible solution images one need to introduce a prior knowledge. Sample-based approaches assume that the desired solution is represented via their similarity to exemplars of previously experienced images (i.e, training datasets). The similarity here refers to the underlying properties and characteristics (e.g., statistical distributions, spectra...) of interest and not to pixel-by-pixel similarity measures. Loosely speaking, we first learn a set of correspondence between the low-resolution and high-resolution patches.

A variety of other techniques have been already proposed in the literature. Some of these approaches focus only on the importance of edges in the textured images [55]. The edge-directed interpolation method described in [56] consists on the estimation of a local covariance coefficients from a low-resolution image and then use these estimates to adapt the interpolation at a higher resolution based on the geometric duality between the low-resolution covariance and the high-resolution one. Besides of the high computational complexity of this method, the resulting super-resolved samples are mostly cartoon-like images. A statistical modeling framework of the edges using the maximum likelihood estimate is proposed in [57]. This approach is crucial for preserving the local anisotropy while obtaining a sharp edges. However, in the textured images edges are not the only key feature and one need, in addition, to generate the small-scale oscillation patterns. Recently, [58] proposes a super-resolution method for the textured images featuring the statistical scale-invariance proprieties. The proposed method exploits a family of stochastic processes, namely the compound Poisson cascade [59], that allows to extrapolate the power spectrum as well as the higher order scale invariant properties to the unresolved high frequencies. One limitation may be that there is any conditioning with respect to the low resolution image and the resulting generated texture details are spatially stationary. Patch-based super-resolution may involve some implicit conditioning but it is seldom made explicit to our knowledge. In this Chapter, we draw upon the non-parametric sampling approaches in texture synthesis [2] and consider an image prior model based on the targeted features taken from other textured images.

The Chapter is organized as follow. In section 3.2 we briefly review the role of both the magnitude and the phase information in stochastic textures. Section 3.3 presents our approach in details and explains the super-resolution scheme. Section 3.4 studies the behavior of this approach using different type of textures. Section

3.5 summarize our main results and points out limitation of the proposed approach.

3.2 Fourier magnitude and phase in stochastic textured images

A stochastic texture is considered as the realization of a spatial random processes. In the Fourier domain, the phase and magnitude play different roles. The randomness is manifested by the fact that only the phase information is random. Synthesizing the so-called random micro-texture, textures that exhibit fast-range dependencies, by a phase randomization technique produces a similar images and do not destroy the visual structural aspect of the image [2]. However, the same randomization approach fails to capture the visual appearance of stochastic textures characterized by a long-range dependencies. This class of textures contains important edge structures (see Fig.3.2). The main motivation of this Chapter is to propose the computationally-

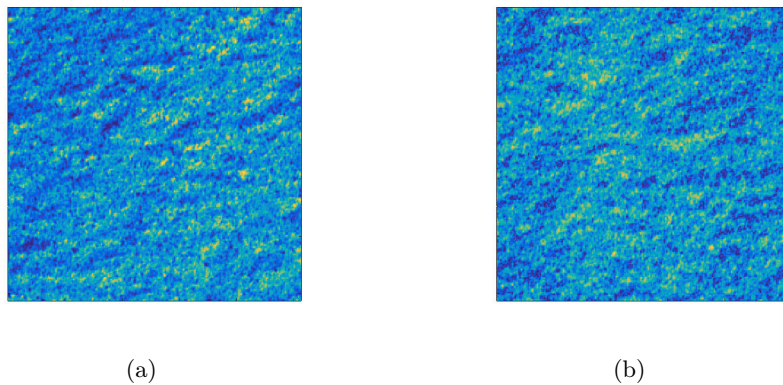


Figure 3.1: Example of texture synthesis by phase randomization [2]. (a) The original sample (b) synthesized texture using the RPN algorithm

efficient method to combine both the Fourier magnitude and phase information to generate a visually high-resolution (HR) images from given low-resolution (LR) input.

3.3 Exemplar-based Super-resolution algorithm

3.3.1 Problem formulation

The super-resolution problem considered in this chapter consists on the following form: A high-resolution textured image is degraded by a low-pass (blurring) filter, It is followed afterwards by a sub-sampling operation. The noise measurement can also be added to the sub-sampled blurred image to create more realistic low-resolution images. In this chapter, we consider noise-free case-studies. Let \mathcal{X} and $\tilde{\mathcal{X}}$ denote

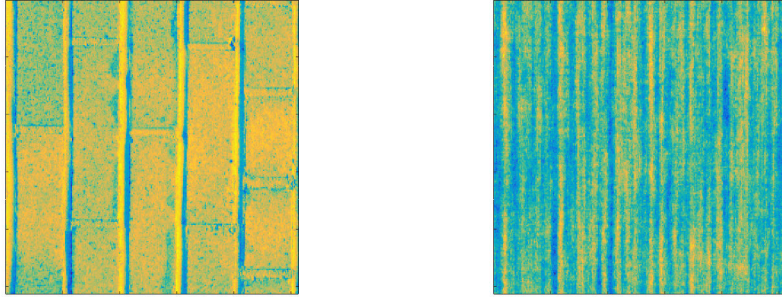


Figure 3.2: Failure example of texture synthesis by phase randomization. (a) The original texture (b) synthesized using the RPN algorithm

the original HR image and the observed LR degraded image. The model can be represented formally as follows:

$$\tilde{\mathcal{X}} = (\mathcal{L} * \mathcal{X}) \downarrow + n(\sigma) \quad (3.1)$$

The low-pass blurring filter \mathcal{L} (e.g., averaging window or Gaussian filter) along with the sub-sampling function (e.g., Dirac comb) gives rise to linear underdetermined system of equations (fewer equations than unknowns) with a many solutions. Thus, the super-resolution problem is an ill-posed inverse problem. To restrain the solution set, one needs to take into account additional prior assumptions about the solution \mathcal{X} .

To address this problem, a prior over the high-resolution image is often considered. Our method relies on the use of a prior on the spectral properties of the inter-scale component between the signal and its augmented (bicubic interpolated) degraded version $\delta\mathcal{X} = \mathcal{X} - \tilde{\mathcal{X}}$.

3.3.2 A model for textured image

In this section, we recall the main definitions and properties of the proposed texture model. The proposed model is divided in two parts. The high frequencies are obtained from homogeneous ADSN process [2, 60]. The low frequencies are given by an image \mathcal{I}_{LR} . The resulting textured image is then obtained by the superposition of the both parts as follows:

$$\mathcal{I} = \mathcal{I}_{LR} + \mathcal{H}(\mathcal{F}^{-1}(|\hat{\mathcal{I}}_{HR}| \exp(i\angle\mathcal{F}\mathcal{I}_{LR}))) \quad (3.2)$$

where \mathcal{H} is a high-pass filter, \mathcal{F} and \mathcal{F}^{-1} refer to the direct and inverse Fourier transform. Notice that the high frequency part of the resulting image has the same phase as the low-resolution component. This property is derived from the well-established importance of phase in images [29, 61].

3.3.3 Superresolution procedure

In this section we detail the elementary steps of the proposed superresolution method. Let r_0 and $r_n(= r_0/2^n)$ be respectively the coarse and the desired resolution. First, we need to resample the original low-resolution image at the intermediate resolution r_1 , with $r_1 = r_0/2$. For this purpose, we use a bicubic interpolation scheme giving rise to a smoothed image $\mathcal{X}_s^{r_0}$ without a considerable addition of small-scale information. The associated Fourier spectrum quickly falls down at scales below r_0 and does not involve a realistic decay (for instance, a power law decay for scale-invariant processes).

The new detail information at scales smaller than r_0 are then modeled and added using the convolution-based process.

$$\mathcal{D}_{r_0}^{r_1}(x, y) = \mathcal{G}_{r_0}^{r_1}(x, y) * \mathcal{B}^{r_1}(x, y) \quad (3.3)$$

where \mathcal{B}^{r_1} is a Gaussian white noise generated at resolution r_1 and $\mathcal{G}_{r_0}^{r_1}$ is the convolution kernel giving rise to the desired Fourier power spectrum of the inter-scale component. The kernel used in (3.3) is computed using the following formula

$$\mathcal{G}_{r_0}^{r_1}(x, y) = \mathcal{F}^{-1}(\sqrt{\tilde{\mathcal{S}}_{r_0}^{r_1}(w)}) \quad (3.4)$$

where \mathcal{F}^{-1} is the inverse Fourier transform and $\tilde{\mathcal{S}}_{r_0}^{r_1}(w)$ is an estimate of the power spectrum.

We estimate the power spectrum of the exemplar using the periodogram-based method. The periodogram is defined as the magnitude squared of the Fourier transform [62]. This definition is based on the Fourier transform. However, the Fourier transform of a non-periodic images suffers from a boundary problem, which causes several artifacts. In particular a well-known cross-shaped artifact in the estimated power spectrum. An efficient way to avoid this problem is the use of Fourier transform of the periodic component as defined by [63].

The generation of the new detail information yields to the following intermediate image:

$$\mathcal{X}_{r_0}^{r_1} = \mathcal{X}_s^{r_0} + \sigma(\mathcal{D}_{r_0}^{r_1} - \langle \mathcal{D}_{r_0}^{r_1} \rangle) \quad (3.5)$$

In some sense, the method, at this stage, reconstructs high frequency textural missing details but does not perform the edge and contour enhancement. In our model this is done by exploiting the Fourier phase information.

$$\mathcal{X}_{r_0}^{r_1} = \mathcal{X}_s^{r_0} + \sigma(\mathcal{F}^{-1}(|\hat{\mathcal{D}}_{r_0}^{r_1}| \exp(i\angle \hat{\mathcal{X}}_s^{r_0})) - \langle \mathcal{D}_{r_0}^{r_1} \rangle) \quad (3.6)$$

where \mathcal{F}^{-1} refers to the inverse Fourier transform. The proposed procedure affects, however, the low frequencies supposed to be contained in $\mathcal{X}_s^{r_0}$. In order to keep the low frequency energy unchanged and to magnify only the missing small wavelength components, a high-pass filter is applied to the reconstructed inter-scale component. In our implementation, we use 2D discrete wavelet transforms as a high-pass filter. The low-frequency energy conservation constraint resorts to keeping only the detail

coefficients of the discrete wavelet transform of the simulated inter-scale component while approximation coefficients at this stage are given by those of the low-resolution observation $\mathcal{X}_s^{r_0}$. In our algorithm, we use Daubechies wavelets. Notice that the same scheme was recently used in [64].

This elementary magnification procedure ($\times 2$) is iteratively performed by cascading the above model until the desired resolution r_n .

3.4 Illustrations

To test the performance of our spectral texture-based prior model and compare it with that of RPN prior (prior only on the Fourier magnitude), we show results of the algorithm on a variety of texture examples. We divide the set of the selected images to the 'ground-truth' 512x512 pixel high-resolution images and the set of training images, each accompanied by corresponding 32x32 pixel low-resolution images generated using 3.1. First, we begin with the case of the micro-textures, defined according to [2], for which the phase information is less important and textures are well-synthesized by phase randomization technique. Our goal here is to check whether this property is also valid in the super-resolution framework, and so the super-resolution scheme, presented in the previous section, could be simplified by working only with the Fourier magnitude without imposing any phase constraint.

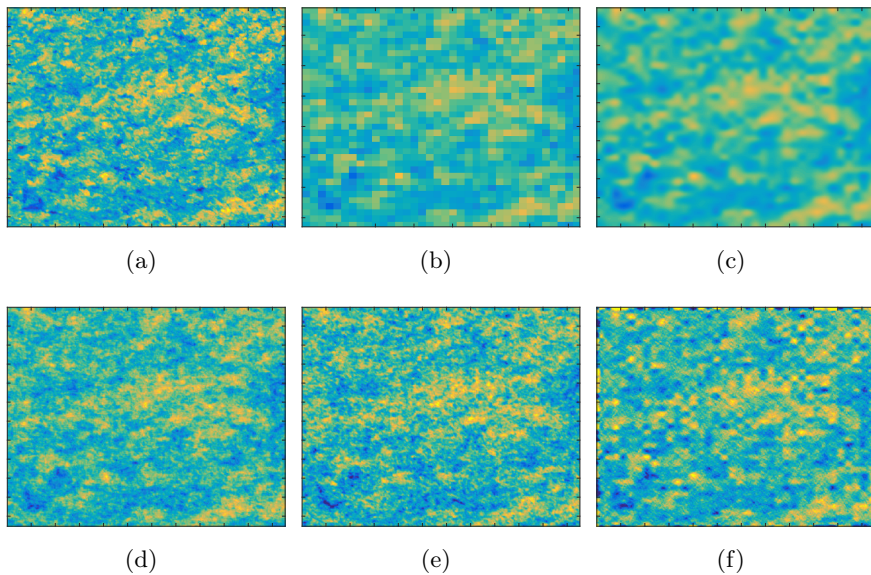


Figure 3.3: Super-resolution of canvas texture: (a) Original image (ground truth). (b) LR image. (c) Bicubic interpolated result. (d) Super-resolution enhanced image obtained using the cascade model with phase randomization. (e) Result obtained without considering cascading. (f) Super-resolution image obtained using phase constraints.

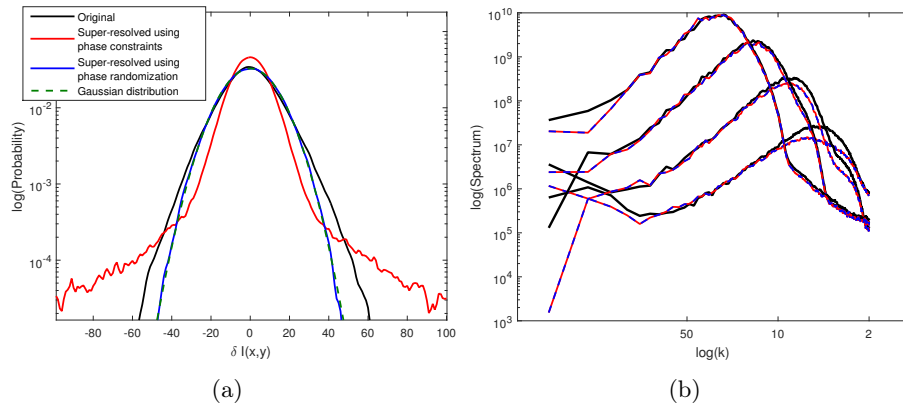


Figure 3.4: Quantitative comparison of results obtained in Fig.3.3. (a) The probability density functions of the marginal cross-scale component of the generated images compared with the ground truth. (b) The spectra of cross-scale components (coarser-to-fine scale).

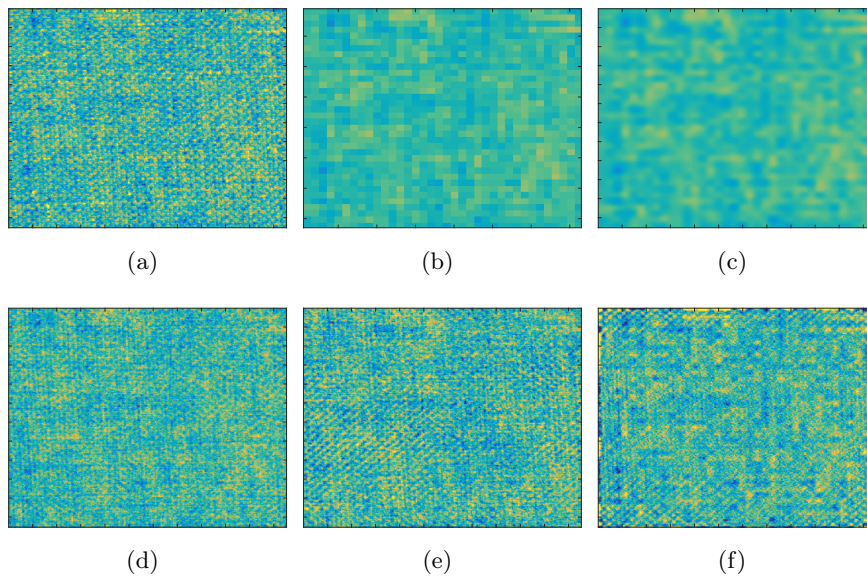


Figure 3.5: The same as Fig.3.3 for the stone texture.

The first two examples of a stone and canvas textures are shown respectively in Fig.3.3 and 3.5. The results obtained by the processing of both examples through the proposed super-resolution algorithm are compared with those obtained by the phase-free algorithm. Our experiments show that the main improvement in the resolution of this type of textures comes from the learned spectrum (i.e., First and second order statistics) and the combined framework does not seem appropriate. In

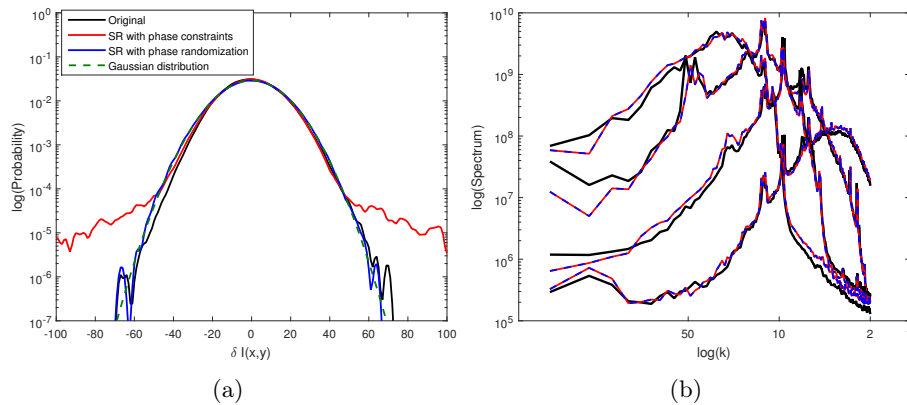


Figure 3.6: The same as Fig.3.4 for the stone texture example.

both examples, the structures of the enhanced texture images resembles that of the ground truth image, even by using only within-scale model without cascading. For such examples, no additional phase constraints seems necessary and all the relevant information is captured by the cross-scale spectrum.

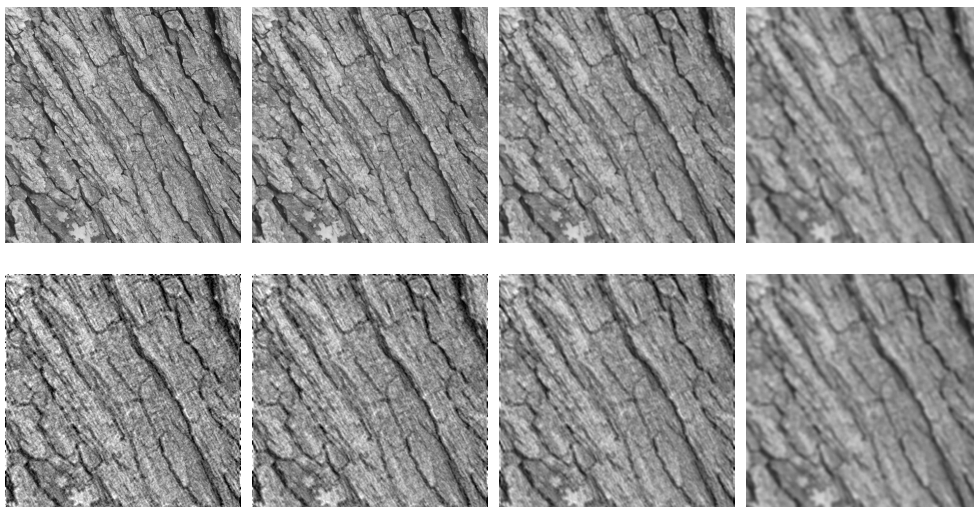


Figure 3.7: Super-resolution of tree bark texture: the first row depicts the ground truth image and the blurred versions using various box filters of size $2^n \times 2^n$ with n ranging from 1 to 3 (from left to right). The super-resolution results are illustrated in the second row for various enlargement factors ranging from $\times 2$ to $\times 8$ (from right to left).

In a second study case, Fig.3.7 displays an example of tree bark texture with highly-structured patterns. This type of texture is characterized by a quasi-

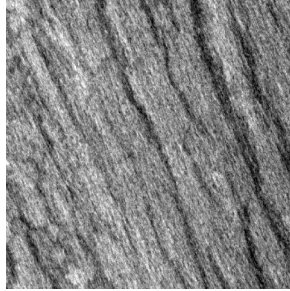


Figure 3.8: Outcome of the RPN algorithm

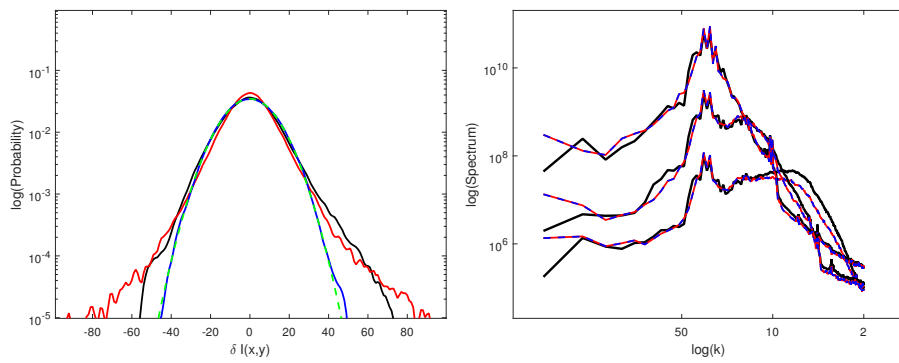


Figure 3.9: The same as Fig.3.4 for the example depicted in Fig.3.7

unidirectional anisotropy direction. We choose a high resolution sample and divide it into a learning and test patches. We carry out constructions exactly as we did for the previous examples (resolution has been artificially degraded by factor 8). The obtained results show that the combined method (i.e., cross-spectrum prior + phase constraints) offer a qualitative improvement comparing to Fig.3.8, obtained by the phase-free model, especially in the edge areas and sharp patterns. Fig.3.9 compares the statistical and spectral characteristics of the ground truth texture the model output.

3.5 Concluding discussion

An important challenge in modeling and enhancement of stochastic textures is to combine second-order statistics (i.e., spectrum) with the phase information. This Chapter raises the question of whether these can be combined in a simple form solution to realistically reproduce high-resolution textures from low-resolution inputs. We demonstrated that assumptions about (only) second-order structure provide good results in the case of homogeneous Gaussian micro-textures. Phase constraints are, however, needed in the case of textures containing important edge structure. In this Chapter, we proposed the simplest possible framework which put together both Fourier spectrum constraint and a phase constraint on the detail synthesis. This approach seems to give good results in the case of textures that exhibit unidirectional patterns. The Fourier spectrum, however, is a global representation of the texture patterns. It cannot unveil their local frequency contents or their local regularity. Thus, one negative aspect of this approach is that we have not been able to develop an analogue for highly-structured textures with locally varying anisotropy direction. Transformation domain techniques, involving image decomposition into a set of spatially oriented frequency channels [65], may be necessary. Such approaches will be explored in Chapter 6 with an application to super-resolution of real satellite images.

Part II

Application to reconstruction of
high resolved textured images
from remote sensing observations

SST-derived geometrical characterization of ocean surface dynamics using Schramm-Loewner Evolution

Contents

3.1 Introduction	50
3.2 Fourier magnitude and phase in stochastic textured images	51
3.3 Exemplar-based Super-resolution algorithm	51
3.3.1 Problem formulation	51
3.3.2 A model for textured image	52
3.3.3 Superresolution procedure	53
3.4 Illustrations	54
3.5 Concluding discussion	58

Abstract In this chapter, we investigate the extent to which the geometrical features of satellite-derived observations of sea surface temperature conform to Schramm-Loewner evolution (SLE) curves. Theoretical and numerical evidence that, for turbulent flows, including SQG dynamics, the level-lines of advected tracers may depict SLE behavior (i.e. curves, which can be mapped into a one-dimensional Brownian motion). By contrast, satellite-derived high-resolution SST observations for active ocean regions are shown to involve more general processes, with Loewner evolution driven by non-homogeneous fractional Brownian motion. The extracted driving forces exhibit a regime-switching behavior, in particular regarding volatilities. We report empirical evidence of an underlying latent state (or regime) given by the magnitude of the gradient and of a regime-independent spectral slope of the Brownian process $s = -2$.

4.1 Introduction

High resolution satellite-derived sea surface images (sea surface temperature, reflectance and/or roughness) often reveal numerous small scale patterns, as eddies

and filaments. These oceanic features with scales smaller than the first baroclinic deformation radius (roughly 20-40 km away from the equator and high latitudes) have drawn increasing attention over the last few years. An important motivation is that wide regions of the ocean are often filled with surface fronts that produce intricate but seemingly organized patterns, likely associated with enhanced horizontal and vertical transports. Traditionally, the characterization of the instantaneous (Eulerian) submesoscale activity involves probability density functions (pdf) and power spectra for the flow variables (momentum, vorticity, tracer) or their gradients. Using large-swath satellite data, observations can help revealing this wide variety of patterns. This textural richness often leads to continuous spectral estimates that span a very wide range of spatial scales. Variances at these different scales are then further often found to follow power-law distributions. Spectral analysis then plays an important role to analyze these observations. It stresses that sea surface temperature and velocity variance distributions in the real ocean can significantly differ from those anticipated from QG arguments ([66]) which could not properly reproduce frontogenesis and the induced strong vertical velocities. In turn, these findings have stimulated research efforts on surface quasi-geostrophy (SQG, [67]), where surface tracer and velocity spectra depict theoretical slopes rolling off as $-5/3$, much shallower than QG prediction, and indeed corresponding more closely to observations ([68]).

Yet, analyzing satellite images, it can be rapidly tested that the original signals can be recovered, although deteriorated, by only using its Fourier phase information while setting its Fourier amplitude information to unity. In contrast to that, if only the amplitudes are obtained and the phases are set to zero or randomly distributed, the recovered image information is almost completely indiscernible ([69]). Indeed, the phase information determines the location and orientation of image features and boundaries, while the module provides only information on their intensity. This indicates that the resulting tracer distribution must thus possess a certain degree of coherence. More specifically, large-scale and small-scale harmonics are likely not statistically independent. Accordingly, power spectra are not solely sufficient at characterizing some important properties of the underlying flow shaping the spatial distribution of the tracer. More particularly, the spectra cannot directly inform about the complexity of front arrangements that can locally arise. A further understanding of tracer mixing related to the proper characterization of its spatial variability thus requires statistical information beyond power spectra. At small scales, tracers can both be organized by large scale motions into thin and relatively smooth filaments, and further stirred by small scale (sub-mesoscale ageostrophic) motions. As such, the degree of regularity of the tracer can be locally impacted, and the analysis of the curvature along tracer field contours certainly suggested to better characterize the competition between the bending and stretching properties of the underlying flow [70, 71]. Our goal here is thus to explore and apply alternative effective means for the analysis of spatial variability depicted by a trace to possibly unveil the importance of submesoscale stirring based on the resulting tracer geometrical properties. Following recent theoretical and numerical evidences that turbulent

flows may involve specific geometrical features characterized by SLE curves [15], we investigate a SLE-derived strategy for the characterization of sea surface dynamics. It comes to the statistical analysis and decomposition of the geometry of isolines of the considered tracer according to the driving function of Loewner map. Loewner maps provide a mean to map 2D isolines to a one-dimensional signal. As such, random 2D curves may be characterized by the associated one-dimensional random walks.

The chapter is organized as follows. The data used in this study are presented in section 4.2.1. The SLE-based analysis method is briefly described in 4.2.2. The results are presented and discussed in 4.3 and 4.4 respectively.

4.2 Materials and Methods

4.2.1 Sea surface temperature Data

As geophysical tracer, we first consider ultra high resolution Landsat 8 Level 1 Thermal Infrared Sensor (TIRS band 10) images provided by the United States Geological Survey (USGS) EROS Center (<http://earthexplorer.usgs.gov/>). The product is converted from spectral radiance to brightness temperature (BT) [72]. The resolution of the TIRS thermal sensor is 100m and the data are resampled to 30m to match multispectral bands. As an example, we select the whole cloud-free image data received on September 11, 2014 (8021×8131 pixels). The scene covers the North Atlantic Ocean near the Brittany coast in the north-west of France (Fig. 4.1). In our study, we are particularly interested in areas where the activity of the upper ocean dynamics is very important (e.g, frontal areas) and the signal-to-noise performance is improved. We also consider high-resolution L2 level SST snapshots provided by the infrared VIIRS sensor at 0.75km resolution onboard the Suomi National Polar-Orbiting Partnership (NPP) and by the infrared MODIS sensor at 1km resolution from Aqua and Terra satellites.

4.2.2 Schramm-Loewner Evolution and geometrical features of turbulent processes

The Schramm (or Stochastic) Loewner evolution (SLE) was introduced by Oded Schramm [13] to find scaling limits of various probabilistic discrete processes in the 2D plane (e.g., Loop-erased random walks). SLE has been shown to describe many conformally-invariant (i.e., locally scale invariant) 2D complex systems, especially in statistical physics (e.g., percolation). Recently, this theory has found applications in areas close to that considered in this paper [73, 74, 15]. The SLE theory is the only analytic framework (to our knowledge) that allows for modeling the non-self-touching-like random curves by mapping them recursively using a succession of conformal mappings onto a one-dimensional Brownian motion parametrized by a single parameter κ , called the diffusivity.

Here, we give a brief introduction to SLE curves and their related numerical

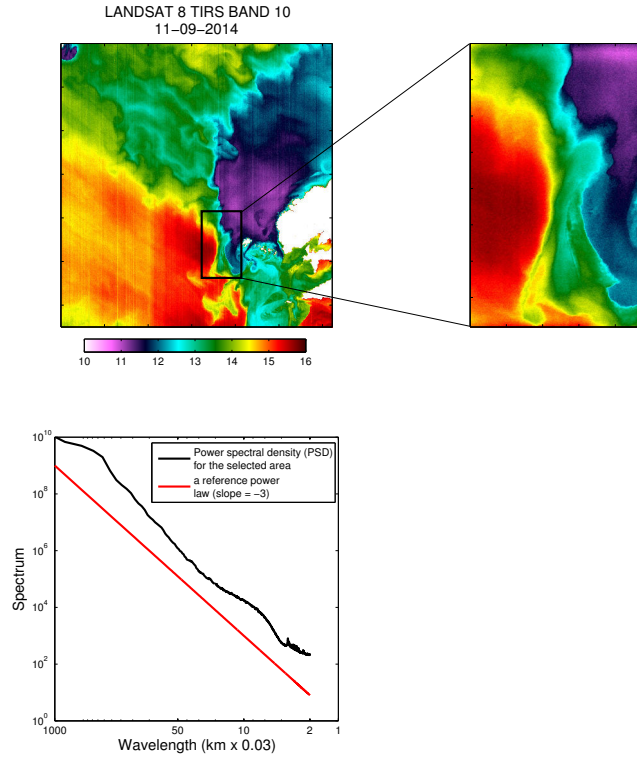


Figure 4.1: Upper panel: Brightness temperature snapshot provided by the infrared TIRS sensor on board Landsat8. Lower panel: The power spectral density of the selected study area.

computation. Let us consider a random non self-touching curve $\gamma(t)$, parametrized by a dimensionless time t , in the upper half plane starting from the origin z_0 and growing to the infinity z_∞ (a point sufficiently far from the origin). According to the Riemann mapping theorem, it is possible, as illustrated in Fig.4.2, to define a unique conformal map g_t at any time t from $H \setminus \gamma[0, t]$ (the whole domain minus the trace of the curve up to time t) onto H itself such that there exists a continuous real function $\xi(t)$ and g_t satisfies the stochastic Loewner differential equation,

$$\partial_t g_t(z) = \frac{2}{g_t(z) - \xi(t)}, \quad g_0(z) = z, \quad (4.1)$$

where $\xi(t)$, called the driving function, is a one-dimensional Brownian motion with zero mean and $\sigma^2(t) = \kappa t$. In addition, the mapping g_t satisfies the following conditions:

- $g_t(\gamma(t)) = \xi(t)$
- $\lim_{|z| \rightarrow \infty} g_t(z) = z$

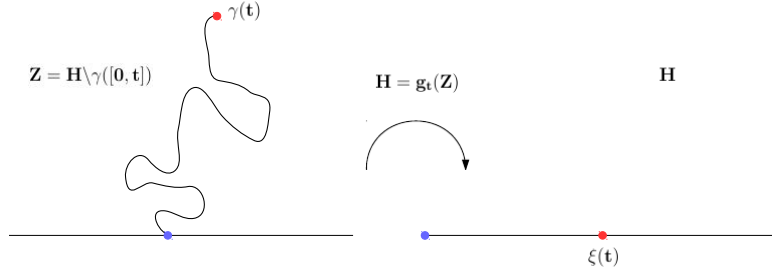


Figure 4.2: Illustration of the Schramm-Loewner evolution idea. The conformal mapping g_t , which satisfies Loewner's equation, maps the upper half plane without the curve up to time t , $H \setminus \gamma([0, t])$, onto the whole upper half plane.

Under the SLE assumption, the diffusivity parameter κ drives a set of geometrical properties of the curve such as the distribution of the winding angles and the fractal dimension. In turn, different methods may be considered to estimate the diffusion constant κ that characterizes SLE curves:

- Winding angle statistics: For a given random curve $\gamma(t)$ in the upper-half plan, we often consider $\gamma(t)$ as a discrete set of points $z(t_i)$ at a discrete times, the continuous (SLE object) curve is obtained by connecting the neighboring sites with line segments. The winding angle along the curve, denoted by $\theta(\gamma)$ and defined at each point $z(t_i)$ can be computed iteratively as $\theta_{i+1} = \theta_i + \alpha_i$, where α_i is the turning angle between the two consecutive points $z(t_i)$ and $z(t_{i+1})$. [75] derive the exact probability distribution of the winding angle for a random SLE curve. This gives a Gaussian distribution with variance:

$$\text{var}(\theta(\gamma)) = \frac{\kappa}{4} \ln(L_y) + c \quad (4.2)$$

with κ is the diffusivity parameter, c is a constant and L_y is the vertical axis size. According to this relation, $\kappa/4$ corresponds to the slope of the variance of $\theta(\gamma)$ against L_y .

- Direct SLE computation: The computation of the distribution of the winding angle is an indirect measurements of the diffusivity κ . Therefore, one can extract and analyze the properties of the underlying driving function $\xi(t)$ directly to see if it corresponds to a Brownian motion. By discretizing the equation 4.1, we can numerically solve it by considering the driving function to be constant within a small (Loewner) time interval δt . One can easily verify that the following map equation is a solution to 4.1:

$$g_t(z) = \xi(t) + \sqrt{(z - \xi(t))^2 + 4\delta t} \quad (4.3)$$

Notice that we can compare those estimates to the prediction $\kappa = \min(2, 8(d_f - 1))$ [76] by measuring the fractal dimension d_f .

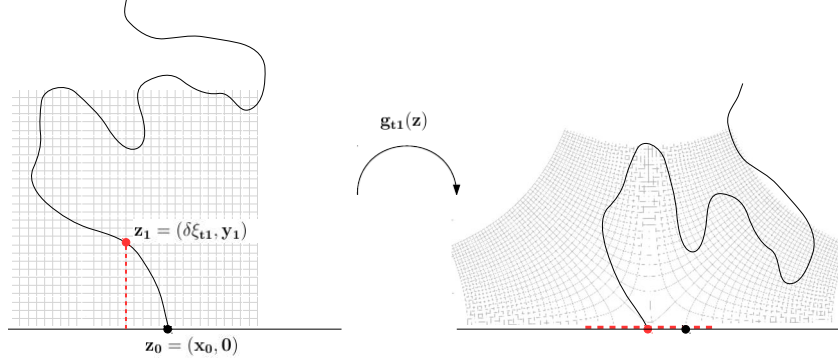


Figure 4.3: Illustration of the an iteration of the slit map algorithm. The portion of the curve between z_0 and z_1 is approximated by a vertical slit (red segment). The algorithm consists of transforming the vertical slit to the abscissa axis. This elementary transformation is iterated for the whole curve.

Slit map algorithm To extract the driving function from a given 2D curve, we use the iterative slit map algorithm described in [77]. For a candidate SLE curve $\gamma([0, T])$ given by its discrete points $\{z_0^0 = 0, z_1^0, \dots, z_n^0\}$, we subdivide the interval $[0, T]$ into $\bigcup_{i=0}^{i=N} [t_i, t_{i+1})$ with $t_0 = 0$ and $t_N = T$ and we consider the driving function as a constant within each time subinterval (i.e., $\xi([t_i, t_{i+1})) = \xi_i$). We then construct the mapping g_{t_i} by a composition of infinitesimal elementary conformal mappings $\tilde{g}_{t_i, t_{i-1}} \circ \tilde{g}_{t_{i-1}, t_{i-2}} \cdots \tilde{g}_{t_1, t_0}$. In this case the value of the driving function $\xi(t_i)$ is given by $g_{t_i}(z(t_i))$. The idea of the slit map algorithm is to approximate the portion of the curve (at iteration j) between the first point $z_0^j = (x_0^j, 0)$, which belongs to the abscissa axis, and the next closest point, $z_1^j = (x_1^j, y_1^j)$, by a vertical segment (called slit). The algorithm then consists in mapping all the points of the curve, obtained at iteration $i - 1$, except the first by the mapping $g_{t_i}(z) = \delta\xi_i + \sqrt{(z - \delta\xi_i)^2 + 4\delta t_i}$ by taking $\delta\xi_i = x_1^i$ and $\delta t_i = y_1^i/4$. One can verify easily that this conformal map removes the vertical slit by sending the top of the segment $z_1^i = (x_1^i, y_1^i)$ to the abscissa axis [see Fig.4.3 for an illustration]. The number of points in the resulting curve after each iteration is reduced by one point. We recursively repeat this process till the whole curve is transformed. This procedure has been checked on an ensemble of Gaussian Free Field (GFF) level lines where it yielded the correct theoretical value $\kappa = 4$ [78] (see Fig.4.4).

4.2.3 SLE-based analysis of SST level-lines

We apply the proposed SLE-based analysis to the level lines of the selected ocean brightness temperature (BT) image with a view to characterizing the underlying turbulent dynamics. A specific aim is to evaluate whether the driving processes obtained by mapping the BT level lines using the Loewner equation conform to

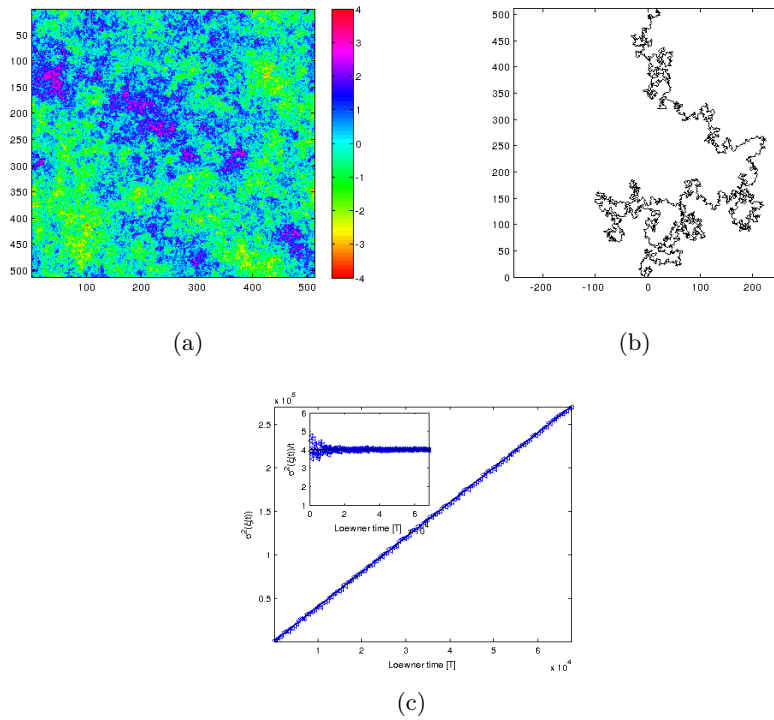


Figure 4.4: SLE-based characterization of the level lines of a Gaussian Gaussian Free Field: (a) realization of the 2D Gaussian Free Field simulated using the spectral method [3] (b) A selected level line of from the simulated snapshot, theoretically proven to resort a realization of a SLE(4) process ($\kappa = 4$) (c) Statistics of the extracted driving functions: variance of the driving functions as a function of the Loewner time. The diffusion coefficient κ is given by the slope of this curve.

Brownian process hypotheses as expected for the inverse turbulent cascade [15].

To verify directly this hypothesis, we proceeded as follows. For the given tracer image, we extract and isolate a large number of level lines. After a simple coordinate transformation (rotation and translation) such that each curve starts from the origin and the rest of points belong the upper half plane, we extract the Loewner driving functions from the transformed level line sample using the slit map algorithm. To verify whether the extracted driving functions $(\xi_t)_{1,\dots,N}$ are well described by a one-dimensional Brownian motion, we calculate the associated diffusion behavior (i.e., the variance $\sigma^2(t)$ for each t) and analyze the associated probability density functions $P(\xi_t)$. In addition, we perform a spectral analysis of the obtained SLE driving functions as well as a statistical analysis of their increments.

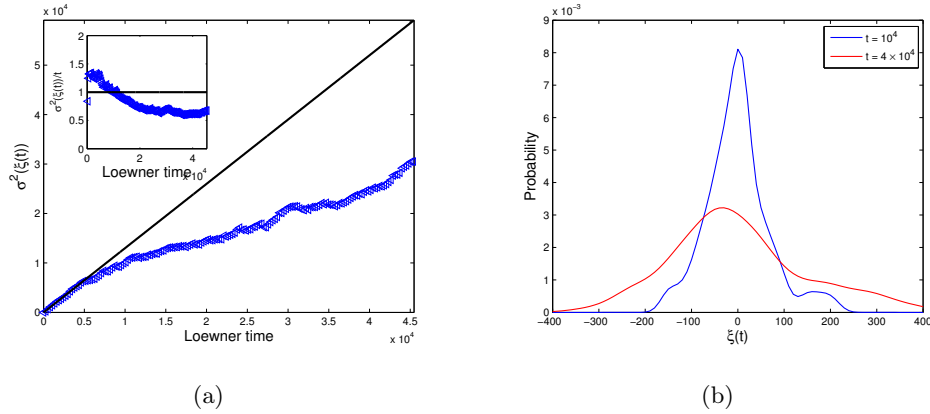


Figure 4.5: Statistics and the diffusive behavior of the extracted driving functions from an ensemble of BT level lines. (a) The variance of ξ_t against the Loewner time. (b) The probability density of ξ_t for $t = 10^4, 4 \times 10^4$.

4.3 Results

We report in this section the application of the proposed SLE-based analysis to the high resolution Landsat 8 TIRS BT snapshot off Brittany in the north-west of France.

SLE-based analysis of the considered BT snapshot: Figure 4.5(a) reports the statistics of the driving functions extracted from a large sample of level lines. We observe a linear scaling of the variance for short (Loewner) time. At somewhat higher time of 0.5×10^4 , it exhibits a deviation from the linear behavior. The instantaneous probability distribution functions of the driving function $P(\xi_t)$ at two different times are shown in Figure 4.5(b). They do not appear to match a Gaussian hypothesis.

Figure 4.7 reports the SLE-based analysis obtained from two different pieces of a selected long level line (see Fig.4.6). Panel 4.7(b) reports the extracted driving functions for both contour pieces. We proceed to check if scaling is observed for the Fourier spectrum of the driving functions and whether the extracted slopes are similar for both curves. In panel 4.7(c) we show the log-log plots of the power spectral densities. The power law relations certainly appear to hold true. Moreover, the empirical spectral slopes are almost the same for both curves. In addition, we statistically analyze the increments of the driving functions. In the inset of Fig.4.7(c) we report the associated probability density functions. We point out a common quasi-Gaussian shape of the normalized distributions. In panel 4.7(d), we plot the mean auto-correlation functions of the increment signals. The correlation function is characterized by a long range dependence for both level lines and does not vanish after a few time steps.

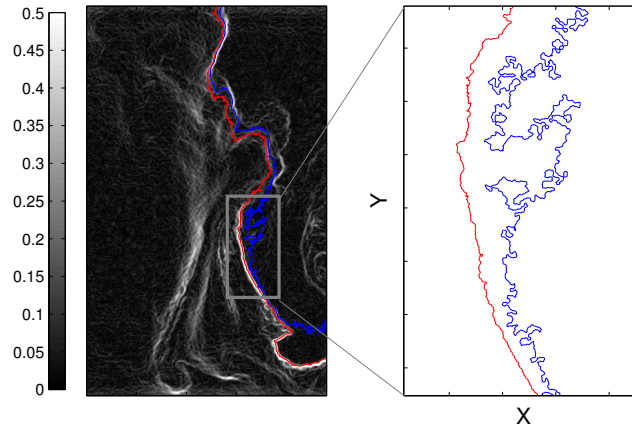


Figure 4.6: The gradient magnitude field of the selected study region with the two selected level lines

BT gradient magnitude as latent driver of the SLE process: The examples reported previously show that BT level-lines do not obey to the standard homogeneous stochastic Loewner evolution SLE, for which the SLE driving functions involve a Brownian motion hypothesis. Fig.4.6 suggests a strong dependence between the local geometrical variabilities of the level-lines and the magnitude of the gradient of the underlying tracer field. This issue is clearly illustrated in the previous example since the two level lines pieces were selected from large (resp. low) gradient magnitude areas (see Inet of Fig.4.7(a)). The driving functions associated with these two curves clearly depict different variabilities.

These observation support the hypothesis of a generalized regime-switching SLE process with BT gradient magnitude acting as a latent driver: the lower the gradient, the greater the diffusivity coefficient κ , *i.e.* the variance of the SLE driving functions. We further investigate this hypothesis from a quantitative point of view. We aim at determining how BT gradient magnitude may act on the spectral slope of the driving functions and on the marginal distribution of their increments. We proceed as follows. In a first step, we compute a moving-window variance of the driving function increments extracted from a non-homogeneous long level-line. Non-homogeneity here means that the distribution of the along-level-line gradient magnitude is not unimodal. We report in Fig.4.8(c) the result of this analysis. We observe a clear strong dependence between the gradient magnitude and the local diffusivity coefficient κ , estimated as the variance of the SLE driving function. The variance increases in the flat regions (*i.e.*, small gradient) to reach values close to 3. Notice that value of $k = 4$ was empirically demonstrated for level lines of the

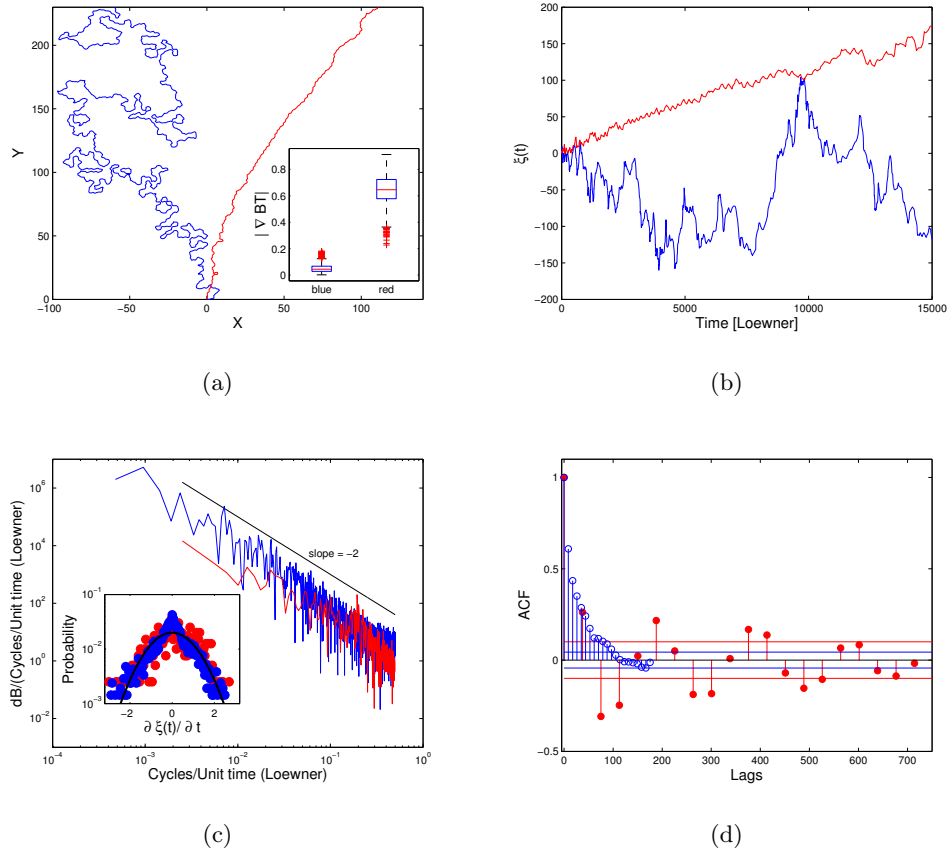


Figure 4.7: Results of the SLE-based analysis of the two selected level lines in Fig.4.6. (a) Level lines transformed to the upper half plane and starting from the origin. Inset: the distribution of the along level line BT gradient magnitude. (b) Driving functions corresponding to the considered level lines. (c) Power spectral density of the extracted forcing function. Inset: The probability density of the driving increments rescaled by its variance. (d) The auto-correlation functions of the driving increments with an approximation of the confidence bounds using the Box-Jenkins-Reinsel approach.

temperature in SQG dynamics model [73]. Conversely, the variance decreases to zero in the frontal areas (i.e., large gradient) as a result of the existence of almost 1D segments. We proceed to check whether the gradient magnitude act on the spectral slope of the driving functions. For this purpose, we sample a large set of BT level-lines extracted from different regions of the image. For each level-line, we also extract the along-level-line BT gradient magnitude. This signal is segmented into homogeneous segments using the algorithm described in [79]. This algorithm is chosen for its performances in capturing well state changes (i.e. jumps i.e). An example of this procedure is illustrated in Figure 4.8(a). Given this gradient-based

segmentation, we carry out a quantitative SLE-based analysis, piece by piece. We report the results in Fig.4.9. Regarding the spectral characteristics of the SLE driving functions, interestingly the dominant pattern is a power decay. The associated spectral slope shows a clear modal distribution around -2.

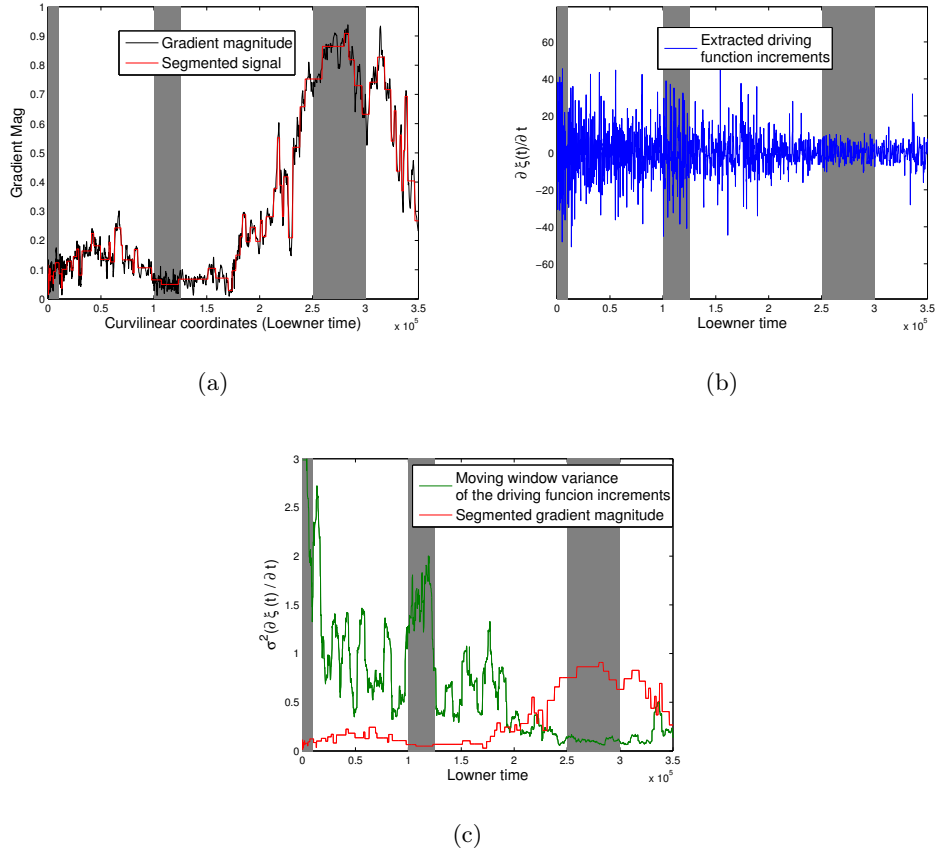


Figure 4.8: Illustration of the gradient-based regime-switching behavior of the driving function. (a) The BT gradient magnitude extracted and segmented from a typical long BT level line. (b) The extracted driving force as function of Loewner time. (c) The moving-window variance of the driving function increments. The variance shows clear dependence on the local gradient magnitude. It increases to reach values between 1.5 and 3 for the low gradient intensities (The two first shaded bar). Conversely, it decreases to zero for large gradients as a result of the existence of a long almost 1D segments.

4.4 Discussion

In this chapter, we investigated the geometrical patterns depicted by a sea surface tracer, namely brightness temperature (BT), as a mean to characterizing the

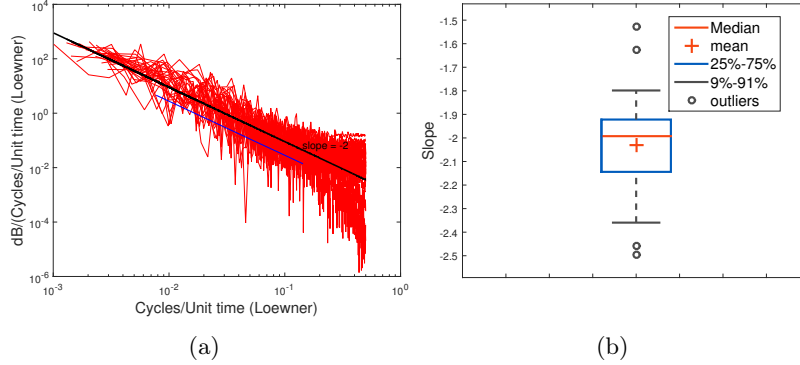


Figure 4.9: (a) Spectral analysis of driving functions extracted from a large ensemble of gradient-based homogeneous portions of BT level lines. (b) The distribution of the empirical fitted spectral slopes. The fitting is done using the normalized spectra in the wavelength bandwidth determined by the blue segment.

underlying submesoscale-mesoscale turbulent dynamics from high-resolution remote sensing observations (100m-1km spatial resolution). Previous works mainly explored empirical statistical features such as spectral analyses or curvature-based analyses [71]. Here, following recent theoretical and numerical advances [15], we propose to analyze the level-lines of the considered tracer as realizations of 2D random walks, and more specifically Schramm-Loewner Evolution processes. Such processes have been shown to arise from turbulent flows, including SQG dynamics. SLE processes relate to conformal invariance properties and are driven by a Brownian motion, whose diffusivity κ controls the geometrical properties of the SLE curves (e.g. fractal dimension, winding angle...). We develop and apply a SLE-based analysis to the level-lines of real high-resolution BT observations. We rely on split algorithm [77] for the identification of the SLE driving functions for any level-line and perform a statistical and spectral analysis of the resulting SLE driving functions.

Our experimental results support the hypothesis of BT level-lines as realizations of SLE-related processes. Whereas Bernard and al. [15] exhibited homogeneous SLE processes driven by standard Brownian motions for numerical simulations of turbulent flows, we show that such homogeneous SLE processes may not be consistent for real sea surface tracers. We here reveal conditional fractional SLE processes, whose driving functions in (Eq.4.1) may be modeled as

$$\xi(t) = \int_0^t dW(t, \kappa(\|\nabla BT(t)\|)) \quad (4.4)$$

where $dW(t)$ is a quasi-Gaussian correlated white noise. Diffusivity coefficient κ , which controls the regularity of the curve, is a function of the magnitude of the gradient of the field: the lower the gradient magnitude, the greater the diffusivity coefficient. The latter implies that, in homogeneous regions (resp. frontal areas), BT level-lines are more irregular (resp. regular). This is an expected behavior in

relation to along-front stretching [80]. Interestingly, for low gradients, the estimated diffusivity coefficient κ is close to 4 as shown by [15] for the SQG dynamics in the inverse turbulent cascades. Random process $W(t)$ is characterized by its modal spectral slope of about -2, and its increments exhibit heavier tails than a Gaussian process. A first explanation may lie in the underlying multifractal nature of the tracer field unlike the analytic predictions of SLE theory (simple fractal). It may be noted that a similar SLE-based analysis was applied to MODIS and VIIRS SST datasets and led to the same observations. This supports the validity of the proposed SLE-based model for the submesoscale-to-mesoscale range.

Overall, our work reveals, to our knowledge for the first time, evidences of non-homogeneous SLE processes driven by fractional noise in real remote sensing observations. Up to now, all known examples of SLE analysis were found using statistical physics models (e.g. Percolation) or fluid mechanics equations (e.g. SQG). This study opens new research avenues from a theoretical point of view in terms of statistical properties of conditional fractional SLE processes and of turbulent flows. Regarding ocean turbulence, it also provides a novel framework for the characterization of ocean turbulence from the geometry of high-resolution sea surface observations, including extension to multi-tracer analyses. Future work should further explore the potential of the proposed SLE-based analysis for the characterization of the space-time variabilities of fine-scale upper ocean dynamics (e.g., seasonal and regional variabilities).

Removing Striping Noise from Cloudy Level 2 Sea Surface Temperature and Ocean Color Datasets

Contents

4.1	Introduction	61
4.2	Materials and Methods	63
4.2.1	Sea surface temperature Data	63
4.2.2	Schramm-Loewner Evolution and geometrical features of turbulent processes	63
4.2.3	SLE-based analysis of SST level-lines	66
4.3	Results	68
4.4	Discussion	71

Abstract This chapter introduces a new destriping algorithm for remote sensing data based on combined Haar Stationary Wavelet transform and Fourier filtering. Striping noise is common in ocean remote sensing observations. The State-of-the-Art methods based on the DWT may not be effective and may cause different visual artifacts when the image is reconstructed. In this context, our contribution is three-fold: i) to avoid as much as possible the shortcoming of the classical DWT, we propose to use the Undecimated Wavelet transform (UWT) known as the most appropriate decomposition for reconstruction purposes; ii) we combine a spectral filtering and UWT using the simplest possible wavelet, the Haar basis; iii) we handle 2D fields with missing data as ocean remote sensing observations may involve large missing data rates due to atmospheric conditions (e.g., clouds). The performances of the proposed filter are tested and validated on the suppression of horizontal strip artifacts in cloudy L2 Sea Surface Temperature (SST) and ocean color snapshots.

5.1 Introduction

Passive sensors on board remote sensing platforms use several scanning methods to generate land and sea surface imagery. Images provided by the Sun-synchronous

Earth orbit satellites are achieved by a combination of progressive scanning lines in the cross-track direction while the sensor platform motion is along the in-track direction. The provided images are often contaminated by several types of noise. These undesired artifacts have an impact on the visual quality of the provided images. If not corrected, these noises will cause processing errors. In this chapter we will deal with striping noise patterns. This type of noise are often present in sea surface temperature and ocean color images provided by infrared and optical imaging spectrometers (e.g. MODIS, VIIRS...). It consists in sharp repetitive patterns which take the form of stripes over the entire image [81] (See Fig.5.1).

The reduction of these stripe artifacts is an important research topic. A large number of destriping algorithms have been recently suggested. All the scene-based methods of the destriping literature exploits geometrical priors about the noise. These priors are related to the regular periodicity of the noise. One may cite a variety of approaches based on low-pass filtering implemented in the spatial or frequency domain [6, 7, 8, 9, 10]. A common feature shared by these methods is that they give rise to blur artifacts. More sophisticated filtering approaches have been proposed. Multiresolution analyses using wavelet decompositions were investigated in [4, 12]. More recently, variational methods were introduced and explored in [82, 83, 5]. These methods may however be prohibitively expensive for large datasets. Reducing striping artifacts in an effective manner without blurring the images still remains challenging. Moreover, the considered case-study applications, infrared sea surface temperature and ocean color observations, do not involve cloud-penetrating sensors, What may result in a very high rate of missing data (gaps) in the provided images. These gaps make the use of the traditional Fourier or wavelet filtering techniques not feasible and requires modifications. In this paper, we address the removal of striping noise in ocean remote sensing images involving missing data as illustrated in Fig.. We develop a destriping algorithm based on a combined wavelet-Fourier filtering. Our algorithm can be regarded as an extension of [4]. We evaluate our contribution for real ocean satellite-derived images with a focus on both SST and ocean color imagery.

This paper is organized as follows. In section 5.2, we provide a short review of the assumptions required by the wavelet decomposition and Fourier transform. In section 5.3, we provide a detailed technical description of the proposed destriping algorithm. We report numerical experiments with real ocean remote sensing data, including a comparison to state-of-the-art approaches in Section 5.4. Section 5.5 concludes this chapter.

5.2 Problem statement

Let us consider an observed image $u_{sn}(i)$ defined in a rectangular domain $i \in \Omega$, affected by an additive stripe-type noise. The image degradation model can be

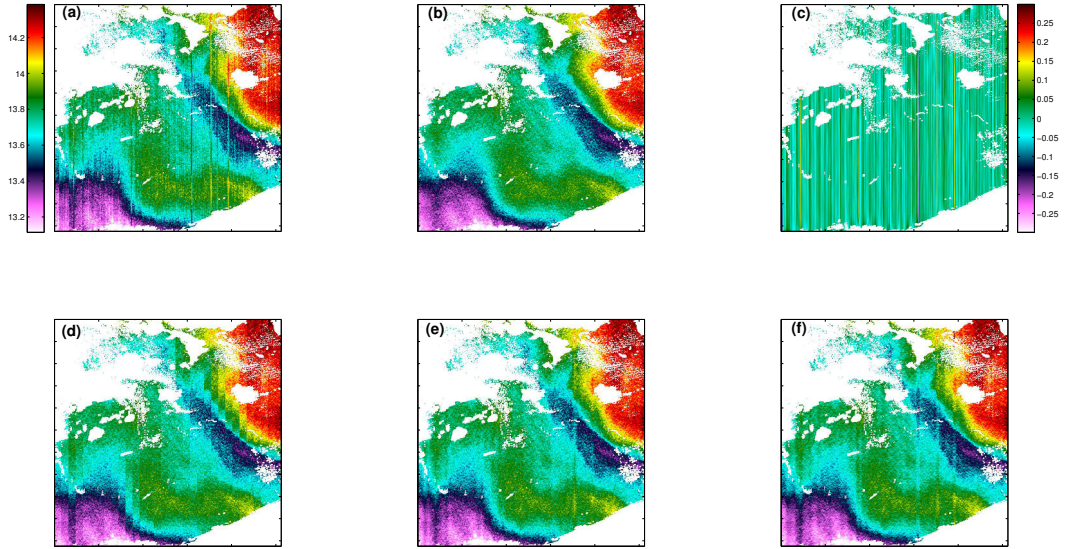


Figure 5.1: Desipping of an ocean brightness temperature snapshot obtained by TIRS Lannsat 8 on September 11, 2014. The original data are shown in panel (b) while the desipped data are shown in panels (b), (d), (e) and (f) using respectively our method, [4] with Haar wavelet, [4] with Daubechies-4 and using a variational approach proposed by [5].

expressed by the following equation

$$u_{sn}(i) = u(i) + sn(i) \quad (5.1)$$

where $u(i)$ would be the true value at pixel i and $sn(i)$ is the striping noise perturbation. The analysis of satellite images shows that the striping noise can be considered as a structured noise in which the large variability is along the y axis of the image, as illustrated in Fig.5.1.

By exploiting this prior on the spatial structure of the undesired noise, the filtering problem consists in removing the striping noise of the images without introducing any blurring effects. Following [4], the proposed approach relies on an appropriate decomposition of the image $u_{sn}(i)$ so that the striping noise effect can be isolated from the original hidden image. Notice that we will not deal with other stationary noise, which may be present in the images and removed using appropriate methods. Several filtering approaches have been developed for the removal of striping noise in satellite images. Following the idea that striping noise is a superposition of quasi-perfect periodic signals and can be easily identified in the 2D Fourier spectrum, one can construct a filter for removing it at a given frequency in the Fourier domain [10]. The weak point of this method is the fact that this filter does not only remove part of the spatial frequency component related to the undesired stripe noise, but also eliminates and reduces the part of the same component present in the real (physical) signal. In order to avoid this over-denoising effect, [4] proposes to perform this

spectral filtering method after a first finite-level discrete dyadic wavelet transform. In this algorithm only the wavelet coefficients (details) are assumed to contain the undesired striping noise and are filtered in the Fourier domain. All the approximation coefficients are kept and the resulting image is obtained by the inverse wavelet transform using the denoised coefficients. The decimated Wavelet analysis (DWT) takes advantage of scaling and directional properties to detect and remove striping patterns in the wavelet domain. The DWT is a non-redundant decomposition [11]. This is particularly interesting for storage and computational efficiency purposes. Nevertheless, for reconstruction-related applications, which is our use case here, the DWT does not fulfill the translation-invariance property, what may lead to a large number of artifacts when modifying its wavelet coefficients.

5.3 Proposed destriping approach: THE UWT-Fourier based destriping scheme

Following [4], we propose to tackle the problem of removing striping noise through a combined wavelet-Fourier approach. As previously mentioned, destriping with the traditional (orthogonal) discrete wavelet transform sometimes exhibits visual artifacts. These artifacts are caused by the sensibility of these algorithms to translation. The Undecimated wavelet transform (also called stationary wavelet transform) was designed to overcome the lack of translation-invariance of the DWT [11]. This property is achieved by removing the decimation step in the orthogonal wavelet transform.

Haar-based UWT decomposition: In the proposed Desptriping scheme, the 2D Haar wavelet transform is the proposed analysis technique. The Haar basis function is well known as the first and the simplest wavelet analysis. The associated scaling and wavelet functions (denoted respectively by $\phi(x)$ and $\rho(x)$) are illustrated in Fig. 5.2.

The major advantages with the use of the Haar analysis are the following:

1. Interpretability: the form of Haar filter is simple and easy to implement;
2. Computational efficiency: unlike the continuous wavelets, fast calculations are obtained, which is important for large satellite derived data products;
3. The inverse transform is performed without any edge effect artifacts. This a key feature in our case as we deal with images involving missing data.

Notice that for applications where reconstruction is needed, the Haar transform also has limitations. Images reconstructed with the Haar filter may exhibit block-like artifacts when the decimation is involved. The considered UWT approach resolve this problem.

The original image u_{sn} is represented in the UWT domain by a sequence of details at different scales and orientations along with an approximation image at a

predefined coarsest scale.

$$\tilde{u} = (\mathcal{U}_0^J, \mathcal{U}^{J-1}, \dots, \mathcal{U}^1) \quad (5.2)$$

where \mathcal{U}_0^J represents the approximation image at the lowest scale J and $\mathcal{U}^k, k = 1 \dots J - 1$ represent the detail images at level k . Each of these component consists of three orientation bands $\mathcal{U}^k = [\mathcal{U}^{k,v}, \mathcal{U}^{k,h}, \mathcal{U}^{k,d}]$. The original image can be obtained using its coefficients by the inverse UWT.

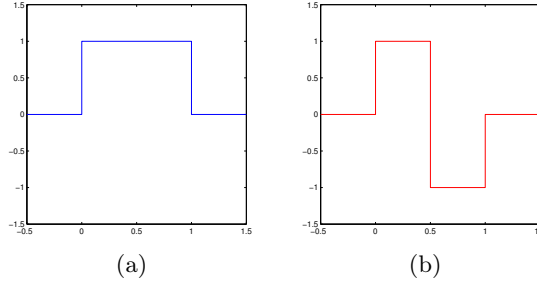


Figure 5.2: The Haar filter. (a) Scaling function (low-pass filter) and (b) Wavelet function (High-pass filter)

Fourier filtering: We assume that the noise is periodic, invariant along the x-axis and distributed over several spectral component. Given the Haar UWT decomposition of the noisy image u_{sn} , we further assume that the striping noise is only present in the vertical and diagonal bands of the UWT decomposition and perform a Fourier filtering independently for each detail image of these two components $\mathcal{U}_{sn}^{i,v,d}$. Let us denote by g_α the considered filter in the Fourier domain. The filtered detail image for band (k, θ) is given by

$$\mathcal{F}^{-1}(g_\alpha \times \mathcal{F}\mathcal{U}_{sn}^{k,\theta}) \quad (5.3)$$

where \mathcal{F} and \mathcal{F}^{-1} refer, respectively, to the Fourier and the inverse Fourier transform. The denoised image \tilde{u} then resorts to

$$\tilde{u}(i) = \mathcal{W}^{-1}(\mathcal{U}_{sn}^0, \mathcal{U}_{sn}^{1,h}, \dots, \mathcal{U}_{sn}^{n,h}, \mathcal{F}^{-1}(g_\alpha \times \mathcal{F}\mathcal{U}_{sn}^{k,\theta})_{k=1:n}) \quad (5.4)$$

where \mathcal{W}^{-1} is the inverse UWT transform, k and θ are, respectively, the scale level and the orientation of the wavelet subband and n is the number of decomposition levels.

Fourier filter design: In the 2D wavenumber domain $\vec{k} = (k_x, k_y)$ the ideal horizontal (resp. vertical) stripes are almost located near the high frequency part in the vertical (resp. horizontal) direction, i.e $(0, k_y)$ [see Fig. 5.3 for an illustration]. The destriping Fourier filter is designed to remove this wavelengths from the Fourier transform of the noisy UWT coefficients. For this purpose, we apply a band-pass

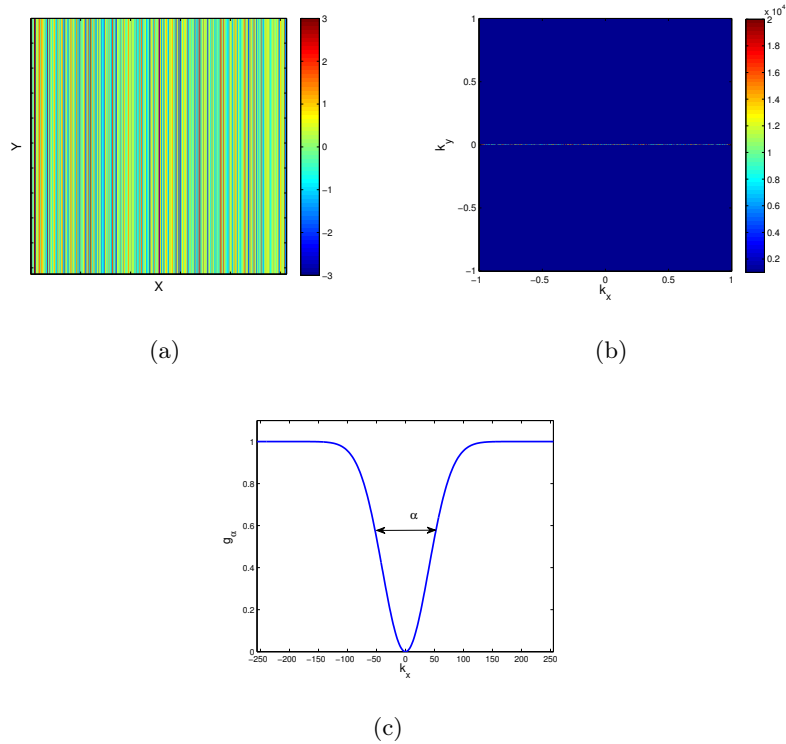


Figure 5.3: (a) A simulated perfect vertical Gaussian striped sheet. (b) The associated 2D power spectrum. All non-zero values are located near the high frequency part in the horizontal direction (c) The inverted Gaussian function considered as the Fourier filter in our algorithm

filter around $k_y = 0$. This can be achieved by the pointwise multiplication of the FFT coefficients with an inverted Gaussian function

$$g(k_x, k_y) = 1 - \exp(-k_x/\sigma^2) \quad (5.5)$$

where σ controls the width of the filter in the k_x -direction. Fig.5.3 shows an example of such a function. Since the observed striping artifacts are almost horizontal (resp. vertical), the value of σ must be small so that the Fourier coefficients are set to zero only at $k_x = 0$ (resp. at $k_y = 0$). Thereby, the filtering process is expected to eliminate striping artifacts without producing blur effects.

We define the method noise of u as the image difference

$$ns(i) = u_{sn}(i) - \tilde{u}(i) \quad (5.6)$$

This method noise (or noise residue) should be as similar as possible to an image composed only of striping patterns.

Destriping in presence of missing data: Destriping in the presence of missing data is a very challenging task, especially when considering a Fourier and wavelet analysis. These decompositions cannot handle images with missing data and require the images to be interpolated prior to the computation of the decompositions. A classical zero-padding strategy may result in a poor estimation of the decomposition and may produce severe visual artifacts due to the introduced discontinuities. It may be noted that we do not address the joint removal of striping noise and interpolation of missing data areas. The goal is rather to apply as preprocessing step an appropriate interpolation scheme, which will result in no noticeable discontinuities of the denoised image at the boundaries of missing data areas. For this purpose, we consider the harmonic image inpainting as described in [84]. The method smoothly interpolates inward from the pixel values on the outer boundary of the missing regions. In the following, we will briefly explain the method. Let us consider an image denoted by f and defined in a rectangular domain denoted by Ω . Suppose that this image is only known at a subset $\Omega_k \subset \Omega$. The harmonic inpainting method consists in filling in the missing region by solving the following Dirichlet boundary value problem

$$\begin{cases} \Delta u = 0 & \text{on } \Omega \setminus \Omega_k \\ u = f & \text{on } \Omega_k \\ \partial_n u = 0 & \text{on } \partial\Omega_k \end{cases} \quad (5.7)$$

where ∂_n denotes the derivative operator normal to the boundaries. We can also consider higher-order differential operators as interpolant (e.g the biharmonic operator Δ^2).

5.4 Experimental Results

Experimental setting: Several BT, SST and ocean color snapshots acquired by MODIS Aqua/Terra, VIIRS NPP and TIRS Landsat8 were selected to illustrate

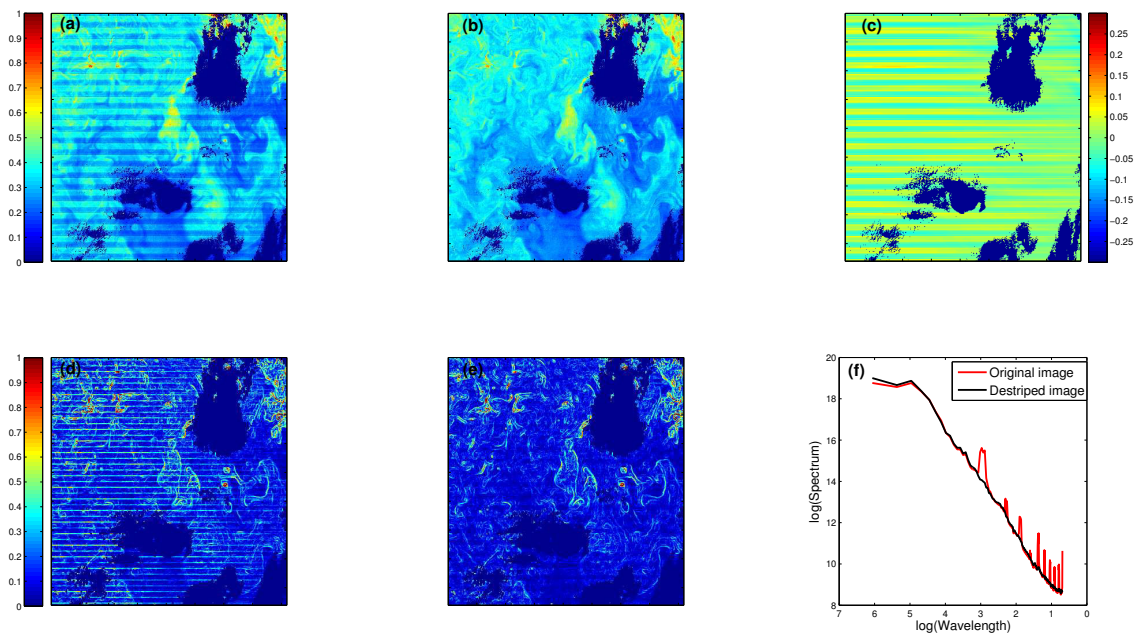


Figure 5.4: Illustration of the destriping of ocean color products: (a) chlorophyll-a concentration obtained by Modis Terra on December 22, 2015 around 06:20 UCT in the Arabian sea region. The destriped data are shown in panel (b). The gradient magnitude of the original image and the destriped image are shown respectively in panel (d) and (e). Comparison of the averaged Fourier power spectrum is illustrated in panel (f).

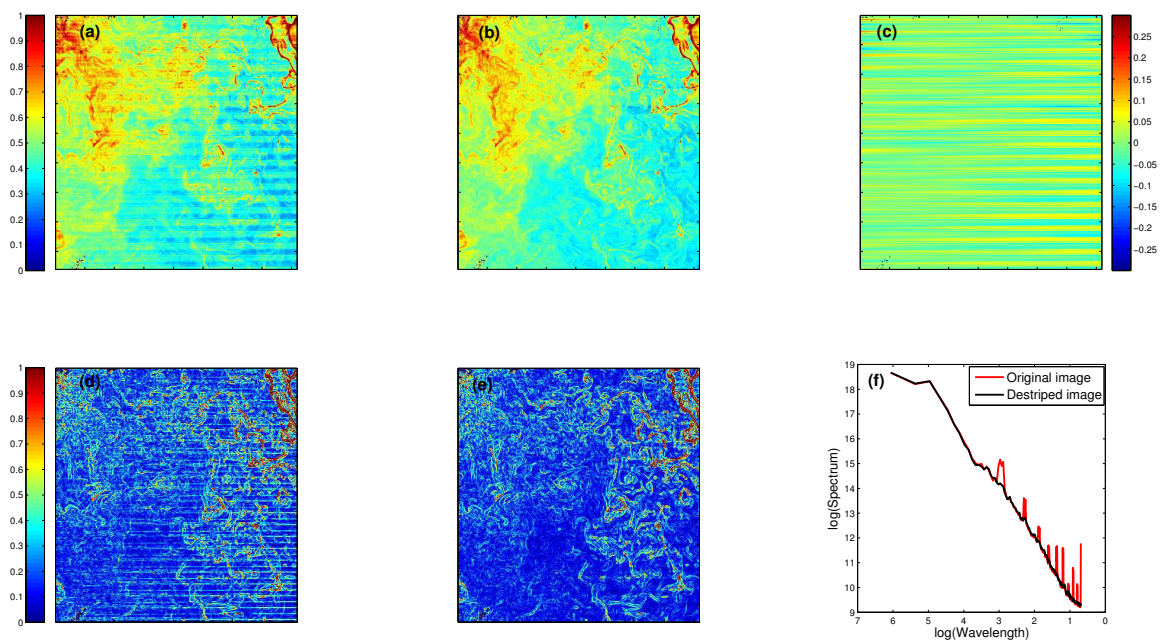


Figure 5.5: Illustration of the Destriping of ocean color products: (a) chlorophyll-a concentration obtained by Modis Terra on December 22, 2015 around 06:20 UCT in the Arabian sea region. The destriped data are shown in panel (b). The gradient magnitude of the original image and the destriped image are shown respectively in panel (d) and (e). Comparison of the averaged Fourier power spectrum is illustrated in panel (f).

and validate the performance of the proposed algorithm. We choose scenes heavily affected with striping noise.

Examples of destriping The visual improvement of Modis-Terra ocean color snapshots is illustrated in Fig.5.4 and Fig.5.5. Smaller images ($\approx 400 \times 400$ pixels) compared to the entire received granule was selected. The reason is that the striping effect is visually hard to observe on significantly large images. Visually, the proposed preprocessing result in a clear improvement of the visual quality of the snapshots. They do not contain any residual horizontal stripes and do not reveal any blur effect. Fronts and sharp gradients areas are degraded by stripe noise in the original images. This occurs because stripes lead to larger vertical gradients. These geometrical features are significantly enhanced in the resulting destriped snapshots. In panels Fig.5.4(f) and Fig.5.5(f), we plotted the averaged Fourier power spectrum. The stripes are revealed in the Fourier spectrum by several impulses (or pics) located at different wavelengths, often at Mid and High frequency components. We can observe from the analysis of the the spectral densities before and after the destriping process that striping noise components are no more observed in the spectra of the processed images.

We also applied our algorithm to SST snapshots provided Modis sensor onboard Aqua platform. As shown in Fig.5.12, we reported similar to those obtained for ocean colour snapshots.

Influence of the key parameters of the proposed scheme.

The results of our destriping method suggest that both the variance of the Fourier filter and the number of decomposition levels in UWT transform do have an effect on the quality of the obtained images. Fig.5.8 shows the joint influence of these key parameters. It suggests that the typical variance parameter must be small. Large values produce a blurring effect. In the various results illustrated in this paper, the default value for the σ parameter is set to 5. Notice that even with smaller values the algorithm gives good performances. Regarding the UWT, a suitable number of decomposition shall not exceed 5 levels. To deal with the missing data issue while using the Fourier filtering, our method uses a preprocessing step which consists in filling in the missing areas using the Laplacian inpainting method. Fig.5.7 stresses the benefit of such an interpolant comparing with the classical zero-padding method. This method has been chosen for a practical considerations, since it is parameter-free and inexpensive in computer storage space (relatively sparse matrices to invert) compared to inpainting method based on high-order differential operators (e.g., biharmonic inpainting) This method is especially suitable for images involving high rate of missing data where the discretisation of Laplace operator gives rise to large matrices. From the reported experiment here using a bi-harmonic interpolant, we expect other inpainting methods based in differential operator (e.g., AMLE) to lead to similar destriping performances, at the expense of an increased computational complexity.

Comparison to state-of-the-art algorithms:

We performed a comparisons to two recent state-of-the-art algorithms, namely the Fourier-wavelet scheme proposed by [4] and the non-local variational approach

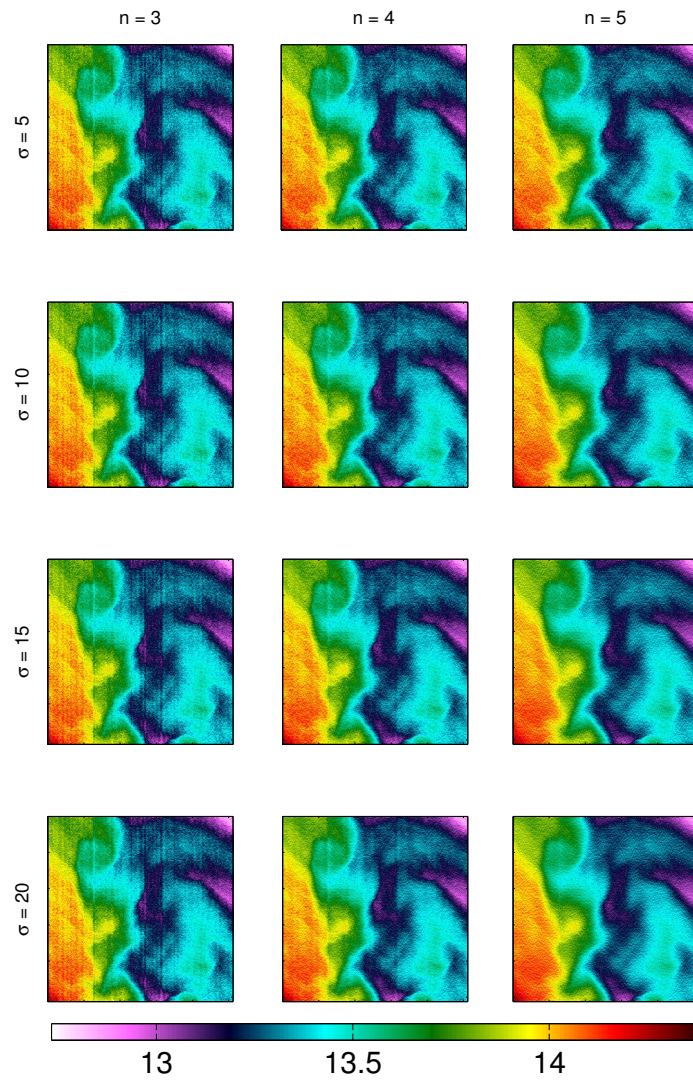


Figure 5.6: Destriping results an ocean brightness temperature snapshot using different values of the variance related to the Fourier filter g_α (Eq.5.3) and for different wavelet decomposition levels.

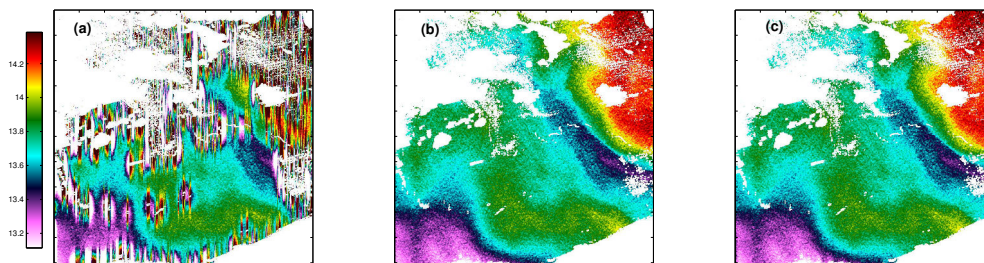


Figure 5.7: Destriping results of the image shown in Fig.5.1(a) using different method for filling the missing areas before destriping; (a) zero-padding; (b) harmonic inpainting (c) biharmonic inpainting.

proposed by [5].

Compared to our approach, [4] uses the decimated wavelet transform (DWT) which is less effective, especially in the heavy stripped image. In addition, the use of the Haar filter is not suitable and the number of taps (i.e., nonzero coefficients) for the chosen wavelet form must be large. This is illustrated by the results reported in Fig.5.8. The quality of the image generated by our method is superior to the images obtained using [4]. Unlike panels Fig.5.8(d)-(e), all the stripes was removed and the image contains no artifacts.

Fig.5.8 also shows the improved destriping performance of our algorithm compared to [5]. We further compare in Fig.5.9 the method noise resulting from our algorithm and [5]. The visual inspection of the associated Fourier power spectra shown in panels Fig.5.9(c)-(d) suggests that the energy of our method noise is almost distributed in the narrow horizontal wavenumbers band near $k_y = 0$. By contrast, the energy related to the method noise of the destriped image using [5] is distributed over a broad spectral band and does not conform to the prior assumption about the geometrical nature of the undesired noise. A direct impact of this observation can be seen in the averaged Fourier spectrum reported in panel Fig.5.9(e). In fact, the signal spectral magnitude is attenuated for frequencies located near the mid-wavenumber region.

To achieve a quantitative comparison with the considered sate-of-the-art methods for the ocean color maps we compute the mean of the cross-track profiles of each image. This quantitative metric measurement gives a good indication of the strength of the striping noise present in a given image. It consists in calculating the average value along each scan line. The presence of stripes translates to the mean cross-track profile by a strong periodicity. Using this metric, the goodness

of a given destriping algorithm is described in terms of its ability to remove this periodic component and obtain a smooth signal. We plot in Fig.5.10 the cross-track profiles of images displayed in Fig.5.4 and Fig.5.5. As expected, the original destriped image exhibits a strong periodicity. The profiles of the destriped images using our approach as well as [4] and [5] are also reported. While our approach and [4] resort to slow-varying profiles with no periodic pattern, [5] does not sufficiently remove these periodic components which are still visible at the end of the scan.

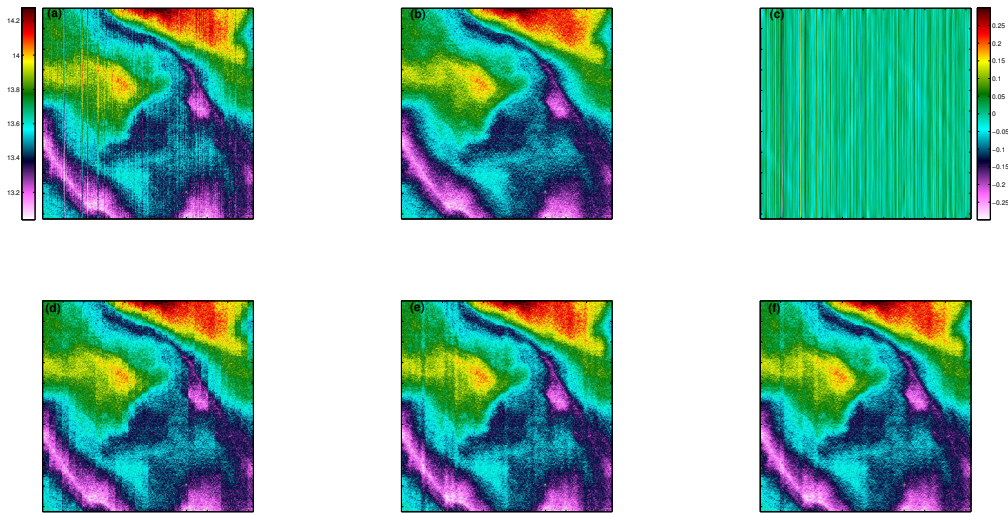


Figure 5.8: (a) Original brightness temperature image from TIRS Landsat 8. (b) Destriped image using our method. (c) The removed residual component. (d) Destriped image with [4] using Haar function. (e) [4] using db4. (f) Destriped image with [5]

Impact of the destriping for the analysis of SST and Ocean Color snapshots: We illustrate the potential of the proposed destriping algorithm for an operational use of the resulting sea surface fields. The first application deals with the application of our algorithm as a preprocessing step in the automatic detection of SST fronts [85]. For this purpose, we apply a Sobel filter to a subset of an original Modis SST maps at full sensor resolution of $\approx 1\text{km}$ and using a downsampled resolution of $\approx 4\text{km}$ (Notice that in [85] the edge detection algorithm is performed using data at $\approx 4\text{km}$). We perform the same operation using the destriped version of the considered image. Fig.5.11 illustrates the results obtained for this experiment. As expected, in both the full and downsampled resolution of the real image, strong gradients are exhibited for real SST fronts and also caused by the vertical stripes. As such, an automatic detection algorithm would hardly be able to discriminate these two classes of gradient patterns. By contrast, the effect of the destriping is clear in the processed images. It reveals more clearly the geometry of the SST fronts, which were occluded in some cases by the striping artifacts. This example illustrates that our destriping scheme can enhance the detection of thermal fronts using simple

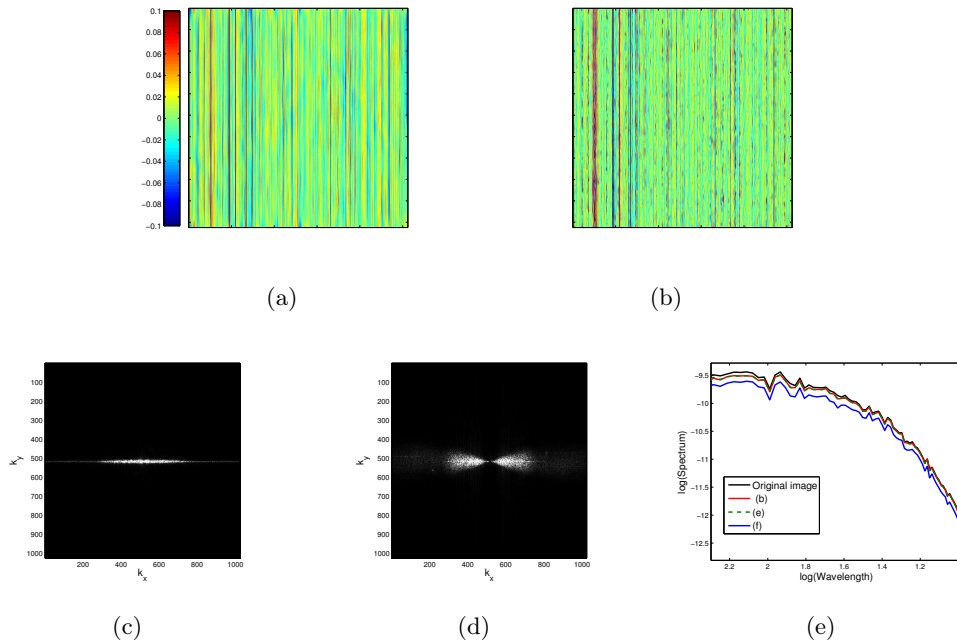


Figure 5.9: The method noise of the original image shown in Fig 5.8 associated to (a) Our method (b) [5]. Panel (c) and (d) report respectively the Fourier power spectrum of (a) and (b). The averaged Fourier power spectrum of the obtained results in Fig 5.8 are plotted in (e), the legend inside refers to Fig.5.8

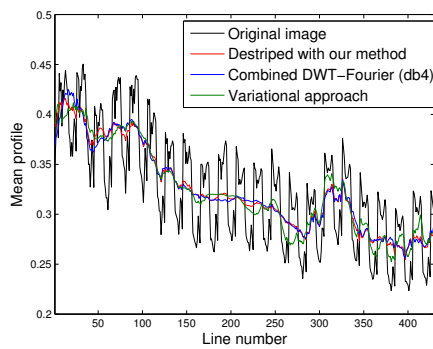


Figure 5.10: Mean cross-track profiles of the original and destriped images shown in (a) Fig.5.5 compared with the state-of-the-art algorithms.

automatic front detection algorithms.

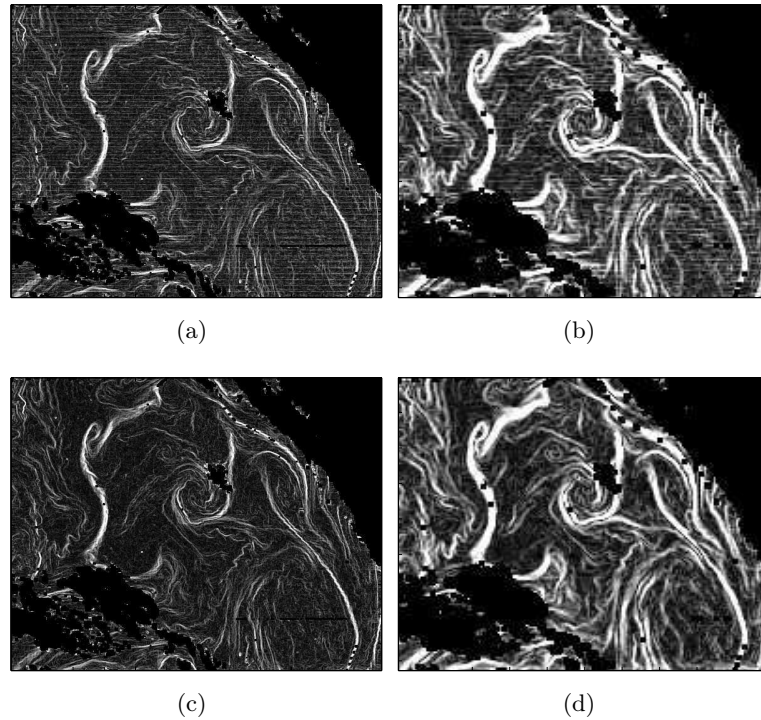


Figure 5.11: Illustration of the impact of the striping noise in the detection of thermal fronts from SST snapshots. The magnitude gradient field of a Modis snapshot computed using the Sobel operator using (a) the full image resolution (b) down-sampled version at 4km (c) destriped image at the full sensor resolution (d) the destriped image at 4km resolution.

The retrieval of Level-2 SST products from a Level 1 brightness temperature data may be considered as a second potential use of the proposed destriping approach. The linear (resp. nonlinear) SST retrieval algorithms are typically based on linear (resp. nonlinear) combination of brightness temperature extracted from several channels. Brightness temperature datasets are also involved with stripe artifacts. Thus, it is more convenient to reduce stripe noise before performing the retrieval. Here we report such an application using VIIRS data. Brightness temperatures from the 375 m resolution Imagery Bands (I-Band) are used with 750 m resolution SST fields obtained from the VIIRS Moderate Resolution Bands (M-Band) to obtain 375 m SST fields. The algorithm consists in computing regression coefficients by a rolling-window analysis. We report two examples in Fig.5.13. They illustrate the benefits of the destriping prior to the application of SST retrieval algorithm.

5.5 Conclusion

In this chapter, we addressed the removal of striping noise artifacts in ocean remote sensing images. Such artifacts are common due to the scanning process underlying the formation of satellite-derived sea surface observations. We proposed a novel destriping scheme, which combines a UWT decomposition of the image to a Fourier filter. Contrary to most state-of-the-art techniques, our scheme also deals with missing data. On different real satellite-derived images, we demonstrated the relevance of the proposed approach compared to previous work. The use of the UWT is regarded as a key component, which brings clear benefit compared to the DWT [4] and variational prior [5]. We also illustrated the impact of the proposed destriping scheme for the further analysis of satellite-derived sea surface fields.

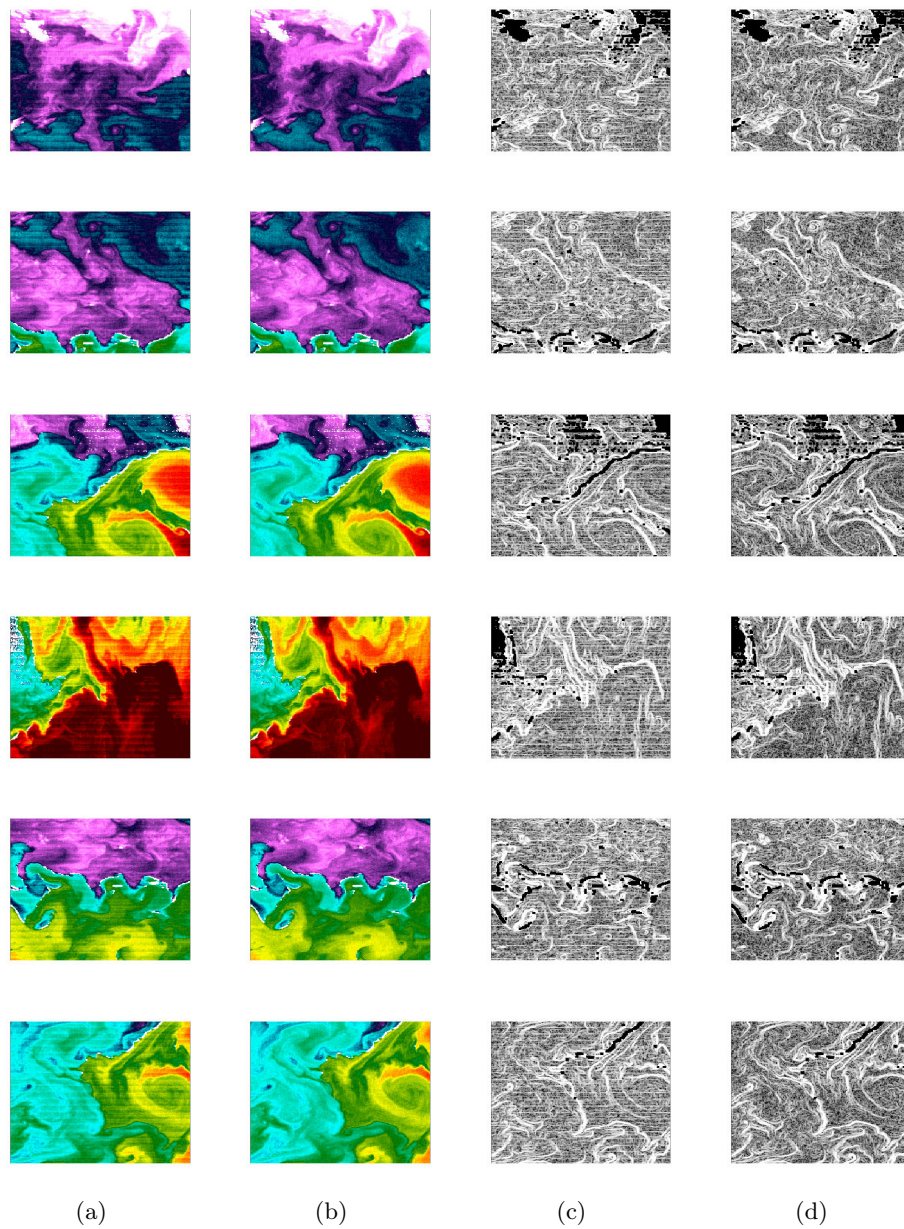
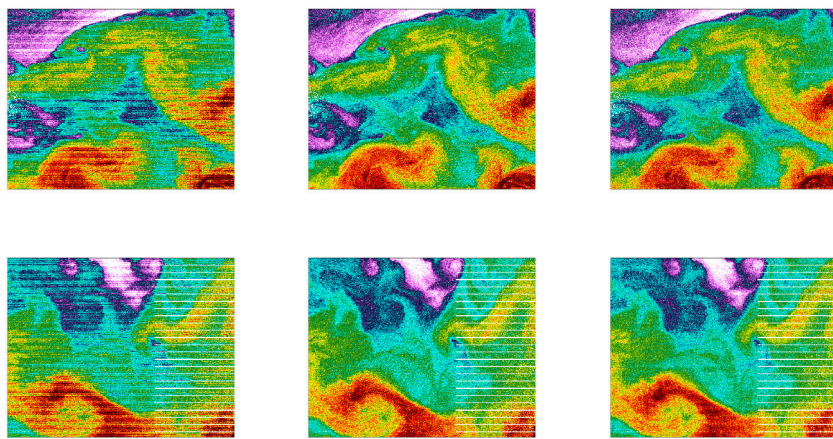


Figure 5.12: Illustration of the destriped results for SST snapshots derived from Aqua Modis sensor. (a) Original images (b) Destriped images with the proposed algorithm. (c) Gradient magnitude of the original fields. (d) Gradient magnitude of the Destriped images



(a) VIIRS SST 750 m (b) Destriped SST 750 m (c) VIIRS SST 375 m

Figure 5.13: Illustration of the potential use of the proposed destriping algorithm. The destriped VIIRS SST data are used along with the I-Band BT at 375 m to produce SST product at 375 m.

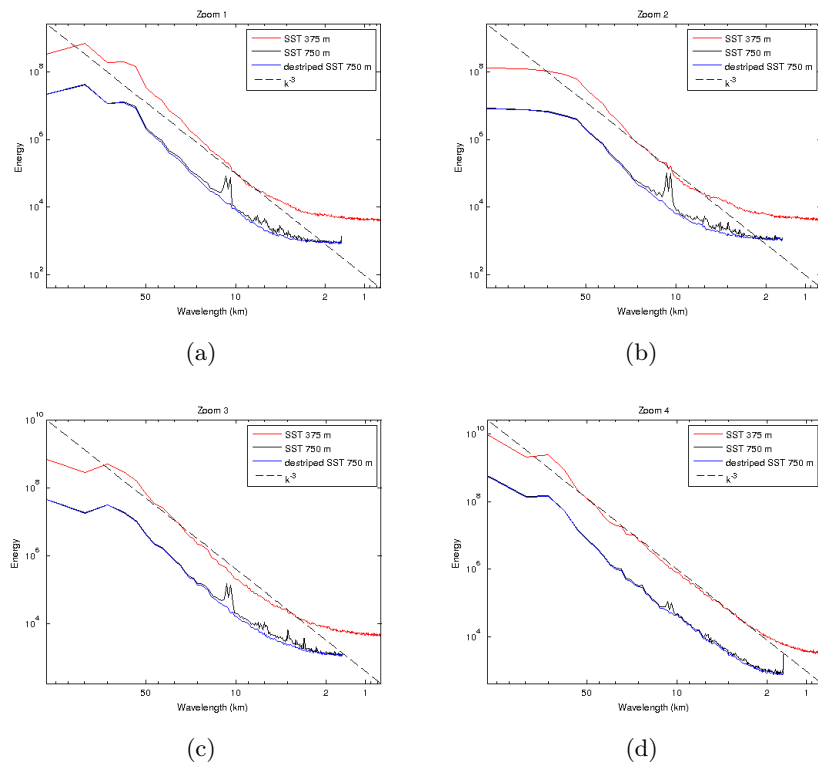


Figure 5.14: Power spectral density (PSD) plots for SST snapshots in Fig 5.6. The frequency components related to the periodic stripes in VIIRS 750 m (Black curves) are extremely attenuated. The graphs have been artificially translated for sake of clarity .

Superresolution of low-resolution satellite SST images using phase-constrained and cascaded multivariate Gaussian models

Contents

5.1 Introduction	75
5.2 Problem statement	76
5.3 Proposed destriping approach: THE UWT-Fourier based destriping scheme	78
5.4 Experimental Results	81
5.5 Conclusion	90

Abstract The characterization of submesoscale dynamics and their impact on the global ocean surface processes is not well understood in part because of the difficulty in addressing it with satellite-based instrumentation. Measurements of fine scale structures over the world oceans are limited by the coarse-resolution of microwave-based sensors on one hand and the sensitivity to cloud coverage of infrared instruments on the other hand. In this chapter, we investigate the possibility of generating high-resolution SST (infrared-like) images using a low-resolution (microwave-like) observations along with an empirical parametrization of the unresolved scales. We consider multivariate random field models based on statistical priors from high-resolution infrared images. The method enhances the resolution of the SST images by exploiting the joint multi-scale statistics of the small-scale details in the wavelet domain using a random cascade model together with an imposed Fourier-phase constraint. Our model is tested and validated using infrared high-resolution satellite SST images provided by Aqua Modis sensor.

6.1 Introduction

Because of its importance to the ocean as well as to the atmosphere, SST is recognized as one of the ocean surface Essential Climate Variables (ECVs). The importance of SST (and the others ECVs) derives primarily from its spatial distribution;

how the parameter varies spatially. To demonstrate this point, we briefly mention some applications: SST is used as the lower boundary condition in the operational Numerical Weather Prediction (NWP) models (i.g., ECMWF). The study of Chelton and Wentz [86] argue that an accurate knowledge of the global SST field is essential for accurate representation of the ocean-atmosphere interaction in the numerical models.

The amount of the available observed variability is, of course, constrained by the spatial resolution of the instruments used to produce maps of the interest variables. Today, it is hard to resolve a 10km (and less) eddy in an SST field. Consequently, the spatial resolution of the data product determines the (physical) processes that may be studied and unveiled. As the resolution of the remotely sensed SST data products has improved it has become increasingly clear that the small-scale features, previously ignored and less-known, may well be impacting large scale ocean processes.

Today, thanks to satellites, a large set of multiscale SST data has been collected using passive satellite sensors. Under certain atmospheric conditions, high-resolution multi-band passive infrared imagery provides a detailed observations of ocean variables. The richness of the provided images allows us to analyze and understand the spatial heterogeneity of the ocean surface. As already mentioned, an extremely important issue, which can be treated and become accessible using the high-resolution data is the characterization of the submesoscale dynamics and their impact on the global ocean surface processes. Unfortunately, however, the infrared measurements has the disadvantage of being restricted to a clear-sky conditions. The low-resolution micro-wave measurements may be considered as an alternative for the retrieval of SST data in the presence of clouds. In addition to the sensibility to heavy rain, the disadvantage using this type of data is the much coarser resolution. The typical pixel size of microwave SST images is $\approx 25-50km$. Therefore, this makes microwave observations rather useful for observing and characterizing global scale ocean processes like major ocean fronts. For the identification of small-scale frontal structures high-resolved fields are required.

The desire for high-resolved SST maps have always been a strong motivation to explore algorithms for optimal enhancement of available low-resolution datasets into more complete high-resolution fields with much more small-scale-resolved details. The Optimal interpolation scheme is the common approaches used to combine all available observations. As a result of smoothing effects, the spatial resolution of the interpolated sea surface temperature product is dramatically degraded. [86] clearly shows the significant dramatic impacts of the optimally interpolated SST fields, used as the lower boundary condition for the European Center for Medium-range Weader Forecasting (ECMWF) global weather model, on the accuracy the surface wind stress in the high SST gradient regions (i.g., Gulf Stream).

To estimate high-resolution geophysical tracers at the ocean surface, given one or multiple sources of low-resolution measurements, a priori information about the multi-scale statistics of the interest variable is essential. In this chapter, we investigate a multi-scale textural-based models for the conditional synthesis of high-

resolution geophysical tracers from a low-resolution observation and possible partial high-resolution observations. The information content associated to textures plays an important role in remotely-sensed SST images. The spatial properties of these images are almost represented by this content, in particular, the truly-resolved scale. It is clear that the point spread function (PSF) associated to low-resolution instruments eliminates or at least reduces the amount of this information. A relevant super-resolution scheme would be expected to realistically reproduce this textural content conditionally to the degraded version of the images. One can learn the shape and the statistics of these textures from observed high-resolution cloud-free fields. The most challenging task while dealing with the synthesis of the observed textures using a given model is the ability to synthesize textures simultaneously at all observation scales (and orientations). As reviewed in Chapter 2, this issue relates to texture synthesis. Spectrally-driven approaches are particularly appealing for SST fields, as they are expected to embed spectral features associated with fine-scale ocean turbulence. Recently, in [2], it is shown that a new texture can be synthesized in a fast and reliable manner by imposing a spectrum directly sampled from an example image. However, this model is restricted to Gaussian textures that exhibit small-scale oscillations and do not contain structured patterns (i.e., edges).

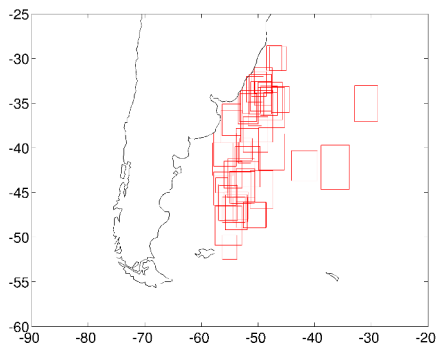
The key contributions of this chapter are: i) the demonstration that SST images (locally) exhibit some remarkably regular multiscale spectral properties, mainly related to inter-scale and scale-to-scale dependencies, ii) the definition of a modeling framework based on multivariate wavelet-based texture models, and iii) the formulation of an additional inter-scale phase constraint. We illustrate from applications to both synthetic and real SST snapshots (Infrared Aqua Modis dataset) collected from different and independent oceanic regions, the relevance of the proposed model to capture important multiscale statistical features of SST fields.

This chapter is organized as follows: Section 6.2 is devoted to a brief discussion of key statistical features of SST images in the Wavelet and Fourier domains. In the context of SST image superresolution, the proposed multivariate texture-based model is described in 6.3 and 6.4. We also discuss different practical aspects of its implementation in 6.5. Section 6.6 reports experimental results. Section 6.7 presents a summary of the study and points out some future research.

6.2 SST data and Elementary statistics

The SST data used in this study have been obtained by Modis thermal infrared sensor on board the Aqua and Terra satellites (NASA Earth Science satellites mission). Data are in Level-2 ungridded orbital swath format and are available on NASA's OceanColor Web supported by the Ocean Biology Processing Group (OBPG) at NASA's Goddard Space Flight Center. We choose relatively cloud-free scenes (typically, no more than 10% of missing data). Fig.6.1 shows locations of the study area where data were collected.

Data pre-processing The collected SST data are processed to reduce the most



(a)

Figure 6.1: Spatial locations of collected SST snapshots in the Malvinas region considered as the area of study

obvious undesired noise. The method described in Chapter 5 is applied to detect and remove the striping noise. In addition, to reduce the amount of the stationary noise, while preserving the sharpness of the fronts, a 3×3 pixel median filter is applied. The data were then gridded, i.e., mapped from the satellite coordinate system onto a regular longitude-latitude grid with a $1km$ spacing.

Different studies investigated the statistical features of SST fields. [87] and [88] studied the statistical structure of sea surface temperature images using high-resolution satellite-based datasets. Fourier and wavelet-based analyses provide a sparse description and parametrization across a wide range of spatial scales. Regarding the averaged Fourier spectrum, it was unveiled that it generally follows a power law. As shown in Fig.6.2(d) this scaling behavior is not far from k^{-3} . The statistical distribution of the wavelet coefficients is characterized by a symmetric and sharp distribution around the mean value with an extended heavy tails significantly heavier than the standard Gaussian case (see Fig.6.2(e)). Note that such non-Gaussian statistical properties are widely acknowledged features of turbulent fields [89] and natural images [90].

6.2.1 Wavelet Decomposition and Marginal Statistics

The representation of images from their wavelet coefficients, illustrated in Fig.6.3, has been proven meaningful for a variety of image processing applications, including image simplification or compression [91], texture characterization and recognition [92]. In the field of geophysics, wavelets decomposition may also appear as powerful tools to characterize the turbulent flows [93]. As derived in [11], an image may be decomposed as a tree wavelet subbands. This representation provides a full and sparse (but not necessarily non-redundant) representation of the image, in the sense that the original image may be exactly reconstructed from this tree of coefficients

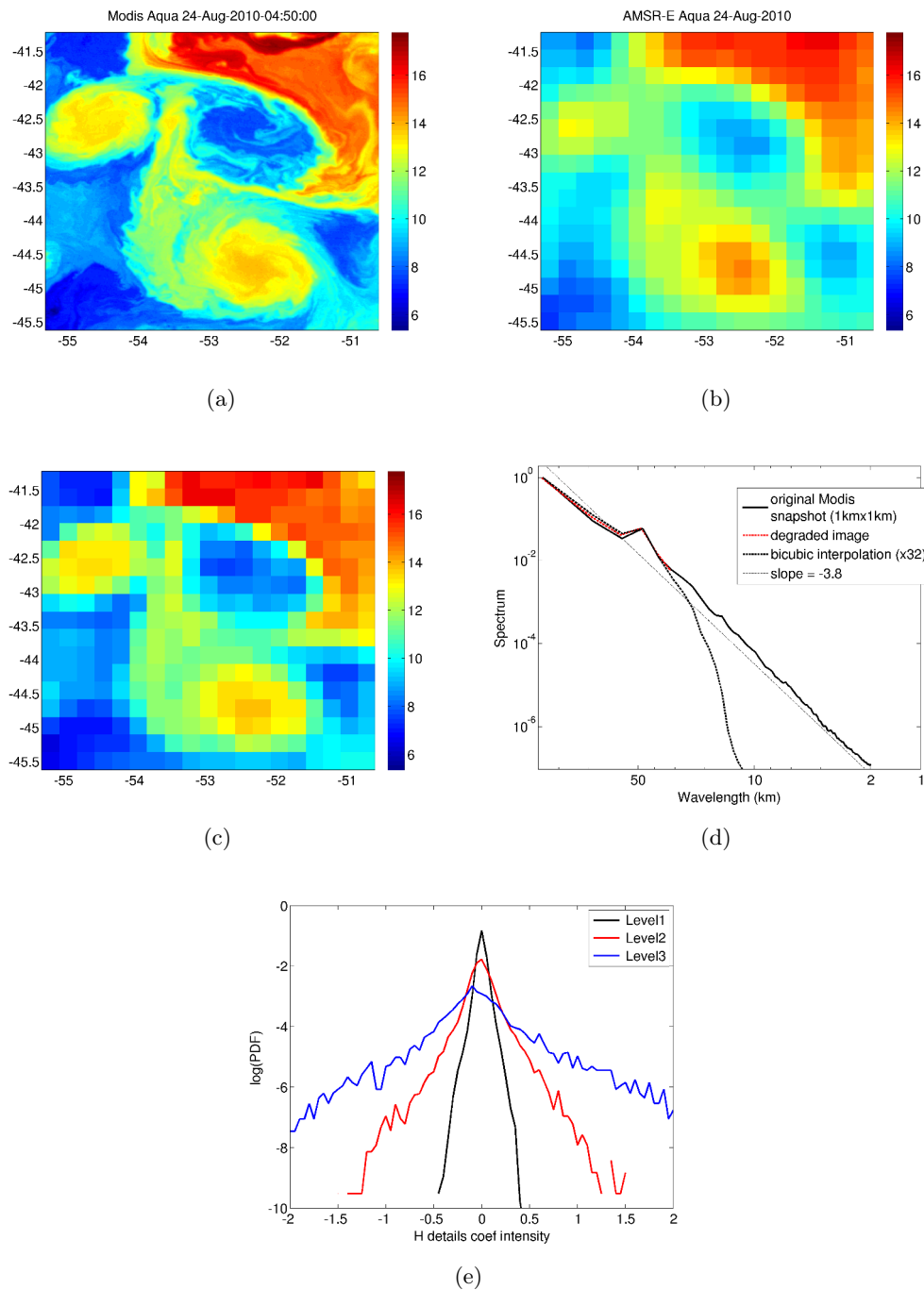


Figure 6.2: Fourier and Wavelet characterization of SST data (a) Snapshot of MODIS SST in the Malvinas region (b) AMSR-E snapshot (c) degraded version of the Modis snapshot to AMSR-E resolution (d) The associated averaged Fourier power spectra (e) Probability density function (PDF) of the horizontal subbands (details) coefficients of the first, second and third levels of the wavelet decomposition of image (a).

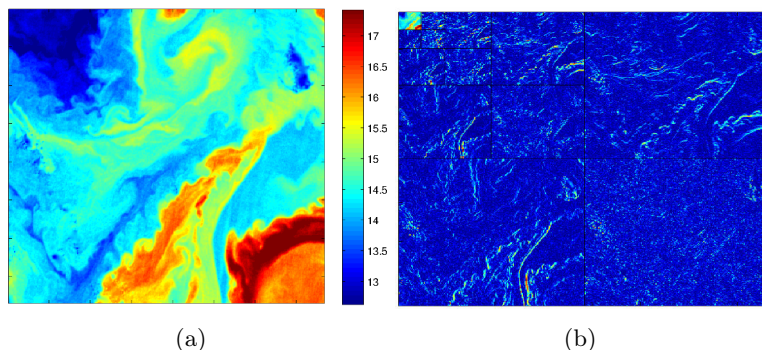


Figure 6.3: Modis SST snapshot (a) and the corresponding Wavelet decomposition at level 4 using db4.

using an inverse transform.

$$u = \mathcal{R}\mathcal{W}u \quad (6.1)$$

where \mathcal{W} and \mathcal{R} refer, respectively, to the direct and inverse wavelet transform. Following Chapters 2 and 3, we further explore such decomposition-based representations with a view to modeling the inter-scale component of SST images.

6.2.2 Joint Statistics of the Wavelet Coefficients: inter-scale and across-scale Dependencies

SST anomaly snapshots are characterized by non-trivial two-dimensional (marginal) correlation structures (see Fig.6.7). Fitting theoretical parametric models to such empirical highly-oscillating anisotropic kernels is not a trivial task. Furthermore, simulation based only on second-order statistics priors (i.e., magnitude Fourier spectrum) do not lead to realistic fields. Fig.6.4 demonstrates that an image generated from a Gaussian process with the same power spectrum as a turbulence-like reference image is easily visually-distinguishable from images of this class. This demonstrates that higher order non-Gaussian statistical properties and non-stationary geometric patterns (e.g., fronts) are contained in the Fourier-phase information [29]. In Fig.6.5, we perform the same experiment as [29], which consists in reconstructing an image from its Fourier coefficients by setting the phase and magnitude components, respectively, to ones. The obtained results shows the importance of the phase information. It may be noticed that we can still distinguish the global geometrical aspect of the image reconstructed with only the Fourier phase part. By contrast, a noisy image is obtained when the phase information is destroyed.

Following these observations, we investigate the (undecimated) wavelet transform, as a mean to perform a sparse decomposition of the strong spatial dependencies observed at different scales. The multi-scale decomposition considered here can be justified in many different ways. As illustrated in Fig.6.3 (for DWT), UWT separates the high resolution input image into different sub-band images.

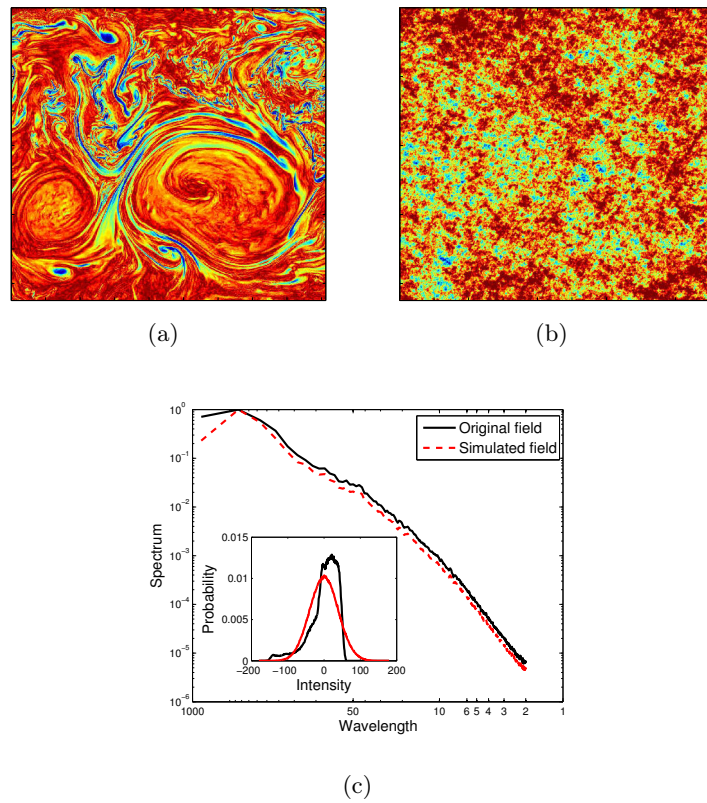


Figure 6.4: Statistical analysis of a 2D turbulent flow field: (a) example of two-dimensional turbulent flow field (b) Synthesized Gaussian image obtained by imposing the spectrum of (a). Comparison of the power spectra. (inset) Comparison of the PDFs.

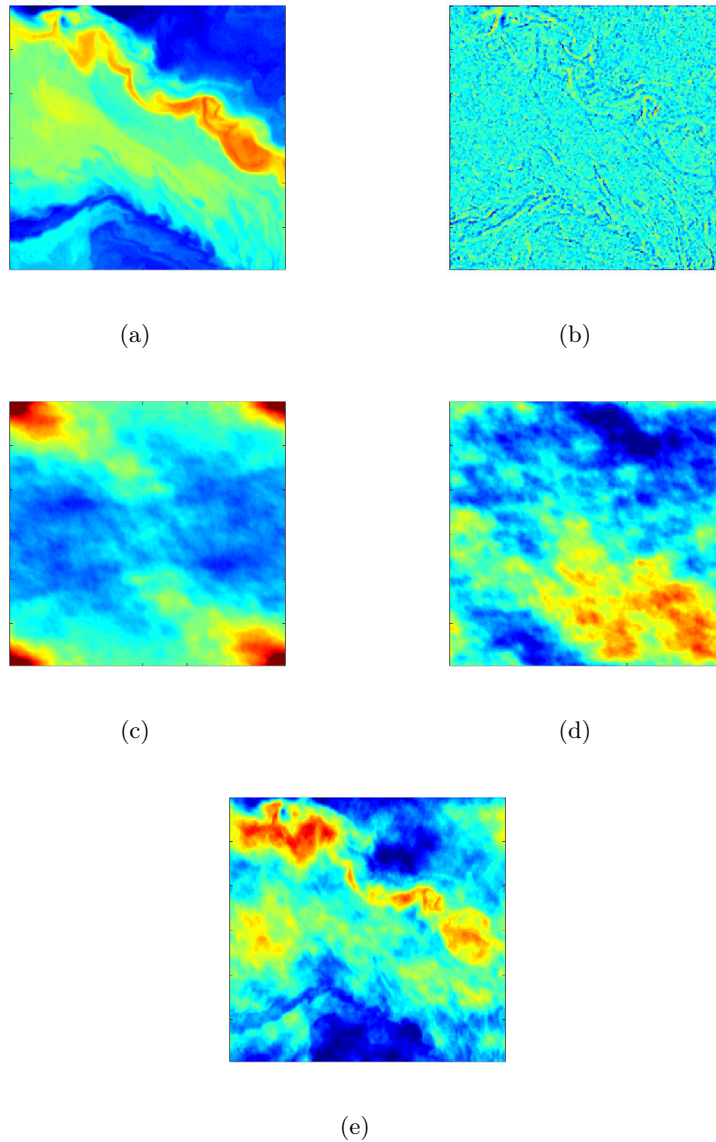
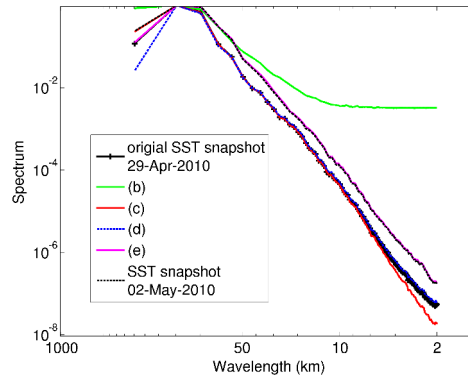
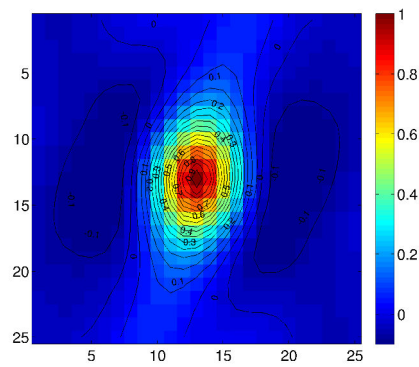


Figure 6.5: Demonstration of the importance of the phase information in the SST images: (a) original SST snapshot provided by Aqua Modis sensor captured on 29-Apr-2010 (b) synthesized image obtained using the inverse Fourier transform by keeping only the phase information (c) image reconstructed by imposing a constant Fourier phase using the same Fourier magnitudes as the original. (d) image obtained by the random phase noise process (RPN) (e) image obtained by using only the phase information from the original image while the magnitude is learned and imposed from another clear-sky SST snapshot captured on 02-May-2010. Remark that the edge information still present in (b) and a realistic image is obtained in (e)



(a)

Figure 6.6: Power Fourier spectra of images reported in Fig.6.3



(a)

Figure 6.7: Autocorrelation function associated to the inter-scale component of Fig.6.2(a)

6.3 Multivariate texture-based models for the Wavelet Coefficients of SST images

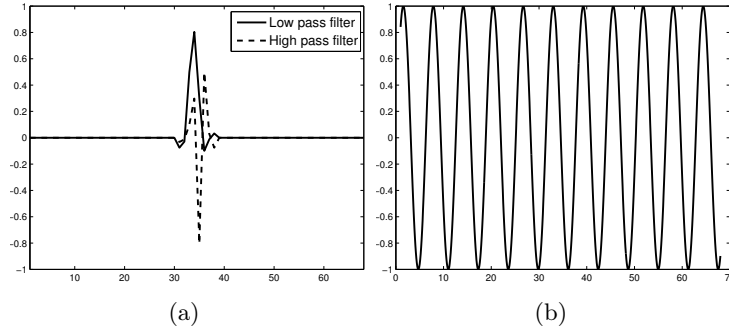


Figure 6.8: (a) The lowpass and highpass analysis filters associated to Symlet wavelet (Sym4), also known as Daubechies least asymmetric wavelets. In order to illustrate the difference with the classical Fourier analysis, a simple sine wave is shown in (b).

As described in [11, 94], the multi-resolution analysis (MRA) allows an orthonormal (energy-conserving) transformation of an original signal into a scale space. This theory was formulated based on the study of orthonormal, compactly supported wavelet bases. This decomposition is quite similar to a signal transformation into the classical Fourier wavenumber space. The difference lies in the fact that the notion of scale in the MRA is spatially localized while the wavenumber, in the Fourier transform, has a global extent (see Fig.6.8). We formally define the length scale in the MRA as:

$$L_n = 2^n L_0 \tag{6.2}$$

where n is the index of a given scale and L_0 is the original or desired scale length in, respectively, the analysis and reconstruction case. In our algorithm, we set $L_0 = 1km$.

The main idea of the MRA analysis is to expand the original signal/image, at L_0 , into two complementary spaces called the scale and wavelet space. Roughly speaking, one can decompose the original signal $s(x, y)$ as $s(x, y) = \tilde{s}(x, y) + \varepsilon(x, y)$ where $\tilde{s}(x, y)$ is a mean smooth part which belongs to the scale space, i.e., L_1 and $\varepsilon(x, y)$ refers to residual field in the wavelet space. Furthermore, one can iterate this operation on the newly obtained scale field into multiple wavelet spaces.

$$s(x, y) = \tilde{s}_n(x, y) + \sum_{k=0}^n \varepsilon_k(x, y) \tag{6.3}$$

where the index of summation k denotes that the scale of the component is $L_k = 2^k L_0$ and n is the largest scale of the decomposition. As an example, the length scale of Modis datasets is $L_0 = 1km$, for $n = 5$ the coarsest scale will be approximately

$30km$ which approximately corresponds to the AMSR-E resolution. Notice that the finer details of the SST field are captured in $(\varepsilon_k(x, y))_{k=1, \dots, n}$ at the smaller indices. Each component in 6.3 can be developed separately as follows:

$$\varepsilon_k(x, y) = \sum_{(i,j)} d_{ij}^{(k)} \chi_{ij}^{(k)}(x, y), \quad j = 1, \dots, n \quad (6.4)$$

$$\tilde{s}_n(x, y) = \sum_{(i,j)} a_{ij}^{(n)} \phi_{ij}^{(n)}(x, y) \quad (6.5)$$

where $d_{ij}^{(k)}$ and $a_{ij}^{(n)}$ are the wavelet coefficients. Respectively, they are called details and approximation coefficients. The basis functions in 6.5 are defined as

$$\chi_{ij}^{(k)}(x, y) = \frac{1}{2^k} \chi\left(\frac{x}{L_k} - i\right) \chi\left(\frac{y}{L_k} - j\right) \quad (6.6)$$

$$\phi_{ij}^{(k)}(x, y) = \frac{1}{2^k} \phi\left(\frac{x}{L_k} - i\right) \phi\left(\frac{y}{L_k} - j\right) \quad (6.7)$$

where χ is one dimensional function called the wavelet function (or the mother wavelet) and ϕ is the scaling function (or the father wavelet). From 6.7 one can assume that the wavelet basis are self-similar functions since each basis function is a scaled and translated version of either the mother or father wavelet function.

Our model exploits the undecimated wavelet transform (UWT) instead of the classical DWT. The UWT filter is carried out without the downsamplers by a factor 2^j at each level j for the decomposition as well as for the reconstruction using the inverse transform. This gives rise to coefficient fields with the same size as the original image to decompose. Notice that the choice of the UWT is motivated by:

1. Overcoming the shift dependency of the discrete wavelet transform (DWT) [11].
2. Computational Statistical Inference: to properly estimate the empirical cross-correlation and joint probability distributions, fields should have the same dimensionality. DWT is a non-redundant decomposition which transforms data into wavelet space preserving cardinality. This can be seen as a direct result of downsampling by a factor 2 at each level and as a consequence subbands, at different levels, do not share the same size. This makes the calculation of the cross-correlation and the joint statistics complex. Redundant transformations, namely the Undecimated wavelet transform, seems here more appropriate.

6.3.1 Cascaded Gaussian random field models on Wavelet Trees

We propose regarding image wavelet sub-bands as realizations of Gaussian Texture-based model. Following Chapter 2, we consider the following formulation

$$\varepsilon_i^\theta = \mathcal{G} * \bar{\mathcal{W}} \quad (6.8)$$

where \mathcal{G} is a spot kernel previously learned from an available sample and $\bar{\mathcal{W}}$ is a noise process. i and θ refer, respectively, to the level and the orientation of the wavelet sub-band. As already seen in Chapter 2, the sampled spot allows us to impose the spectrum of the synthesized sub-bands. Remark that both univariate processes described previously, namely the RPN and the ADSN [2], can be represented by the equation (6.8). The difference lies only in the noise process. Whereas $\bar{\mathcal{W}}$ is a standard Gaussian white noise for the ADSN process, which is defined in the Fourier domain as the process whose Fourier modulus are i.i.d Rayleigh random variables and the phases are distributed according to the circular uniform distribution, the Fourier modulus associated to the RPN process are set to ones. Surprisingly, the wavelet sub-bands we deal with are visibly not susceptible to pointwise multiplication of their Fourier components by a Rayleigh noise. We illustrate this point in 6.9. Of course, the same property is not true for the original image, nor should it be. Thus, both models are valid and applicable in our case.

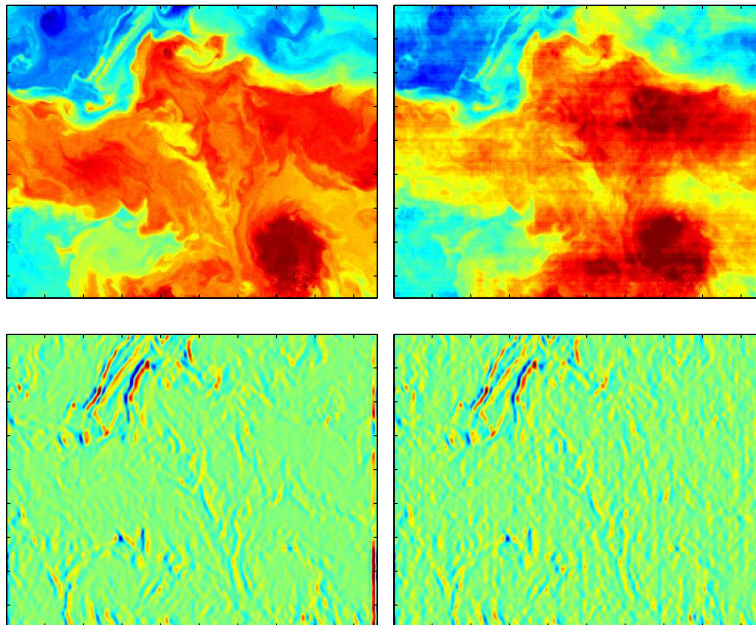


Figure 6.9: Illustration of the effect of the pointwise multiplication of the Fourier modulus by a Rayleigh noise. The SST image (top) is corrupt whereas the associated wavelet sub-bands (bottom) are visually robust to this multiplication. Here, we illustrate this effect using the vertical wavelet sub-band at the level 2.

The above correlated random field model could be employed to model a single sub-band component. Sub-bands are however clearly mutually dependent, at least at the same or closest levels, and applying the above model independently to each component would not make sense. The key idea of our work is to introduce a stochastic multivariate texture-based model, able to model and capture the cross-dependence structures of the wavelet sub-bands (details) of the image, such that

each sub-band is characterized by a texture-based model similar to 6.8. We propose regarding sub-band wavelet (details) coefficients as realizations of multivariate texture-based model as developed in Chapter 2. For a given decomposition length scale L_n , let us denote by $\varepsilon = \{\varepsilon_1^v, \varepsilon_1^h, \varepsilon_1^d, \dots, \varepsilon_n^v, \varepsilon_n^h, \varepsilon_n^d\}$ the wavelet coefficients. Within a continuous setting, such model can be stated according to:

$$\begin{pmatrix} \varepsilon_1 \\ \varepsilon_2 \\ \vdots \\ \varepsilon_n \end{pmatrix} = \begin{pmatrix} \mathcal{G}_{11}(h) & \mathcal{G}_{12}(h) & \cdots & \mathcal{G}_{1n}(h) \\ \mathcal{G}_{21}(h) & \mathcal{G}_{22}(h) & \cdots & \mathcal{G}_{2n}(h) \\ \vdots & \vdots & \ddots & \vdots \\ \mathcal{G}_{n1}(h) & \mathcal{G}_{n2}(h) & \cdots & \mathcal{G}_{nn}(h) \end{pmatrix} \begin{pmatrix} \bar{\mathcal{W}}_1 \\ \bar{\mathcal{W}}_2 \\ \vdots \\ \bar{\mathcal{W}}_n \end{pmatrix} \quad (6.9)$$

where \mathcal{G}_{ij} is a variant of the cross-correlation function, auto-correlation in the case of $i = j$, between ε_i and ε_j . $\bar{\mathcal{W}}$ is a vector of independent white noise process. As has already been noted in Chapter 2, we shall limit ourselves to a triangular block matrix for $(\mathcal{G}_{ij})_{ij}$.

6.4 Super-resolution model

Given the above model, we now address the problem of texture-based super-resolution as the problem of sampling from a conditional multivariate density constrained by an ensemble of statistical and spectral prior measurements taken from a high-resolution example images. The stochastic multivariate texture-based model proposed in 6.3 naturally applies, in the wavelet domain, to consider correlation and cross-correlation priors of the sub-bands wavelets coefficients. In addition, to synthesize the low frequency regularity of the wavelet sub-bands with respect to the low-resolution image (i.e., the structured parts), we impose the Fourier phase of the approximation coefficients.

The considered super-resolution model resorts to:

$$\begin{cases} (\varepsilon_i^{v,h,d})_{i=1,\dots,n} = [\mathcal{G}_{ij}(\theta)]_{1 \leq i,j \leq 3 \times n} * \mathcal{W}^\top \\ \tilde{\varepsilon}_i^{v,h,d} = |\hat{\varepsilon}_i^{v,h,d}| \exp(j \times \angle \hat{s}_n) \\ \tilde{I} = \mathcal{R} \left[s_n, (\tilde{\varepsilon}_i^{v,h,d})_{i=1,\dots,n} \right] \end{cases}$$

where $\mathcal{W} = (\mathcal{W}_1, \dots, \mathcal{W}_{3 \times n})$ is a vector of independent white noises, s_n the approximation coefficients and θ is the exemplar image used to calibrate the various spot kernels. In this model we start with a multivariate independent Gaussian white noises, and force this noises to satisfy the constraints listed above. Notice that the projection constraint is naturally satisfied since we do not change the approximation coefficients.

This super-resolution scheme clearly constrains the geometry of the high-resolution sample \tilde{I} from the geometry of the low-resolution image (UWT approximation coefficients) through the Fourier phase spectrum.

6.5 Numerical resolution

The proposed super-resolution model involves two steps: i) a learning step from an example and ii) the generation of a sample of the multivariate sub-bands model. Regarding the learning step, we consider a non-parametric offline estimation method. Specifically, we apply the following procedure:

1. We first collect exemplar images and for each sample, the wavelet expansion is performed.
2. Kernels \mathcal{G}_{ij} are all computed with respect to the relationships already established in Chapter 2. In particular, these kernels are functionals of the spectral and cross-spectral densities (i.e., correlation and cross-correlation functions) of the wavelet sub-bands. As already mentioned in Chapter 3, we estimate the power spectrum of the exemplar images using the periodogram. The estimation requires only a single exemplar, but unfortunately this gives rise to noisy spectrum. To overcome this problem we compute a mean periodogram by averaging multiple periodograms using several exemplars. The cross-spectrum of two exemplar images is defined as the Fourier transform of their cross-covariance function [95]. However, from the Wiener-Khinchin theorem, it can be implemented more efficiently as the complex-valued product of the Fourier transforms of the two images [96]. In the case of learning from samples involving missing data, instead of directly calculating the spectra, we can compute the correlation and cross-correlation functions, the kernels being then obtained by a Fourier transform of these functions. Once these kernels have been calculated and normalized, it is possible to go to the simulation step.
3. In this step, we assume that we are only provided with a low-resolution version of a new image (not included in the training set), i.e., approximation coefficients. Based on the estimated kernels in the previous offline learning step, we simulate the wavelet details coefficients using Eq.(6.9).

6.6 Results and Discussion

In Fig.6.10 we provide an example of how the new superresolution scheme works using daily synthetic sea-surface temperature observations. Data are generated over a 90 day period for several test regions with infrared resolution $\approx 1km$. Panel (b) shows a high-resolution ($L_0 = 1km$) SST snapshot which we aim at reconstructing. Here we set the length scale parameter from which the reconstruction will be performed to $L_n = 16km$ i.e., $n = 4$. In the obtained low-resolution image, the loss of many small-scale features can be clearly observed. There is also a weakening of the gradient magnitude due to the low-pass filter. We reconstruct the virtual high-resolution field, at $L_0 = 1km$, through our super-resolution scheme starting from the low-resolution image. Using this method, we obtain Fig.6.10(c), which is visually similar to the real image, especially in terms of generated realistic small

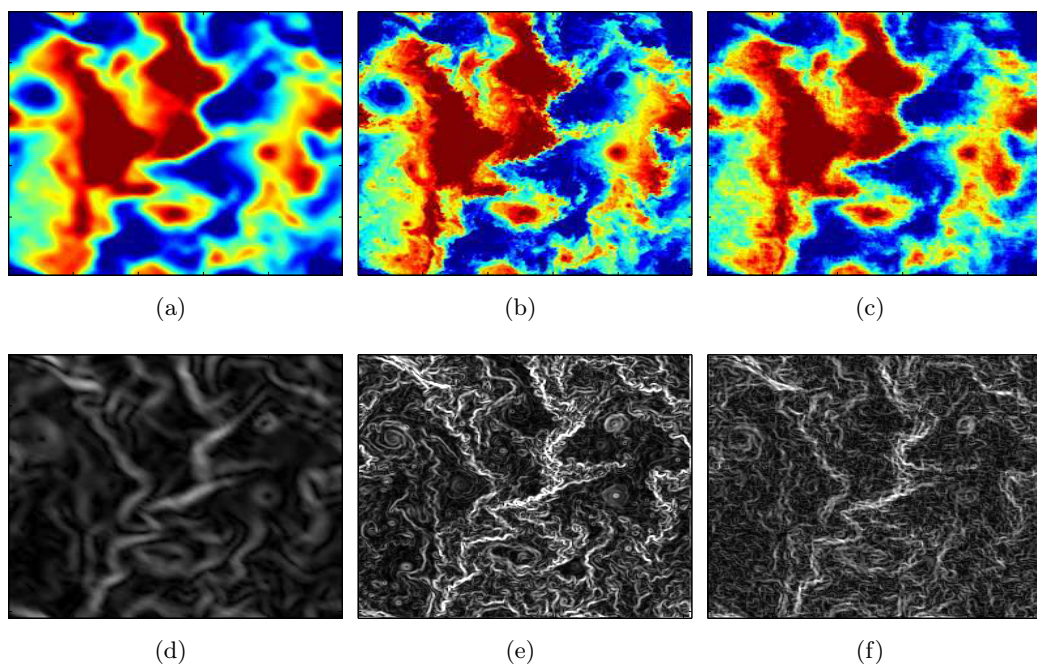


Figure 6.10: Snapshots of the sea-surface temperature (SST) anomaly in a $250km \times 250km$ subregion of the Equatorial Pacific. (a) The low-resolution observation, (b) truly observed high-resolution snapshot and (c) the reconstructed image. The second row depicts respectively the gradient magnitude field of the three images.

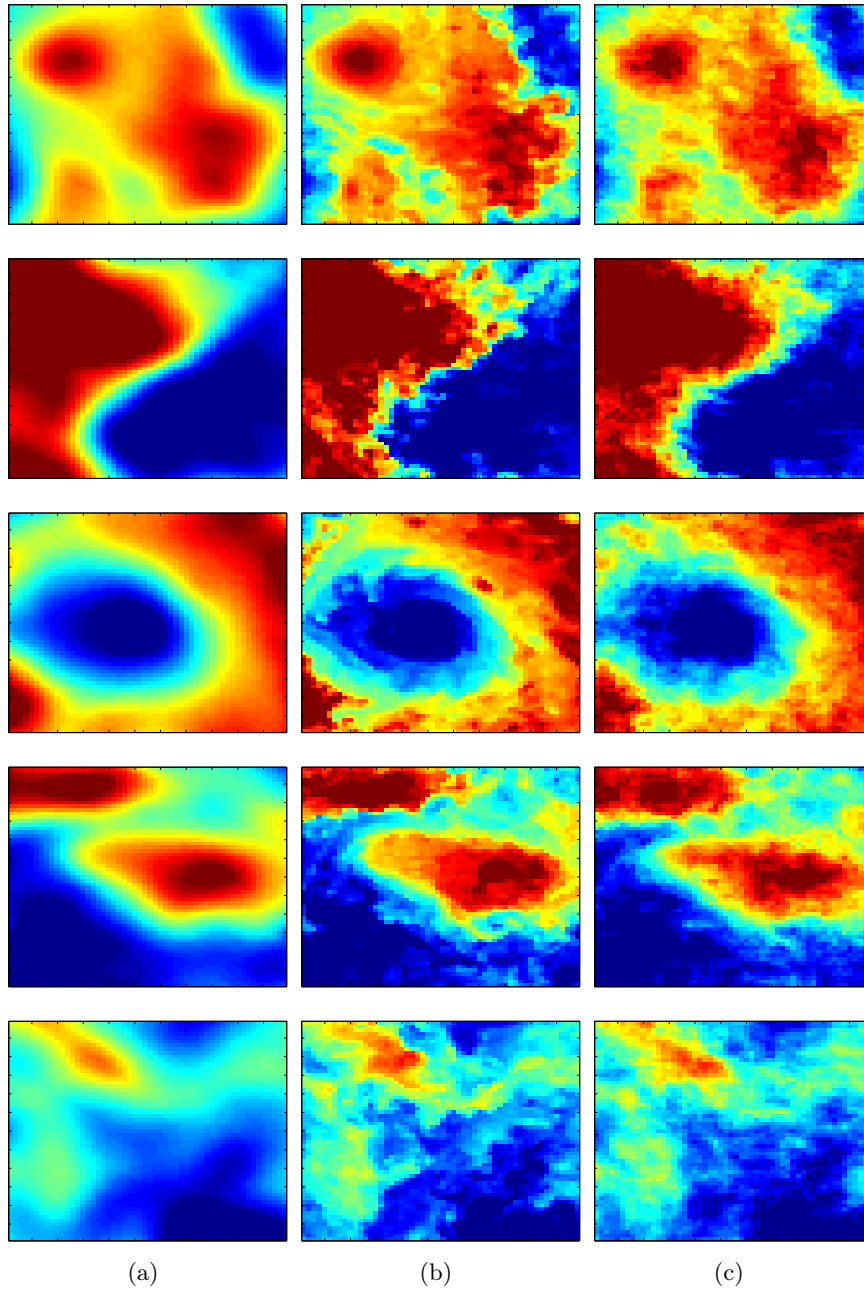


Figure 6.11: zooms into subareas of the image considered in Fig.6.10. (a) Low-resolution patches, (b) true High resolution observations and (c) reconstructed patches.

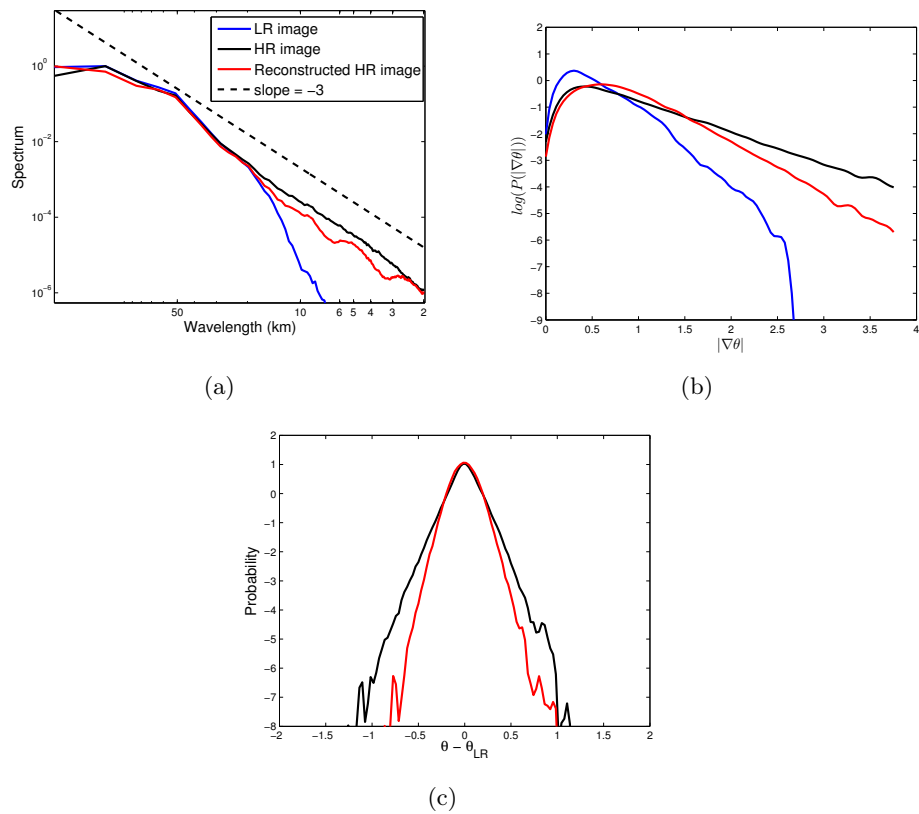


Figure 6.12: Quantitative results showing the Effectiveness of the proposed method. (a) Fourier power spectra. (b) Marginal PDF of the magnitude of SST gradient fields illustrated in Fig.6.10 (second row). (d) Marginal PDF of the inter-scale components.

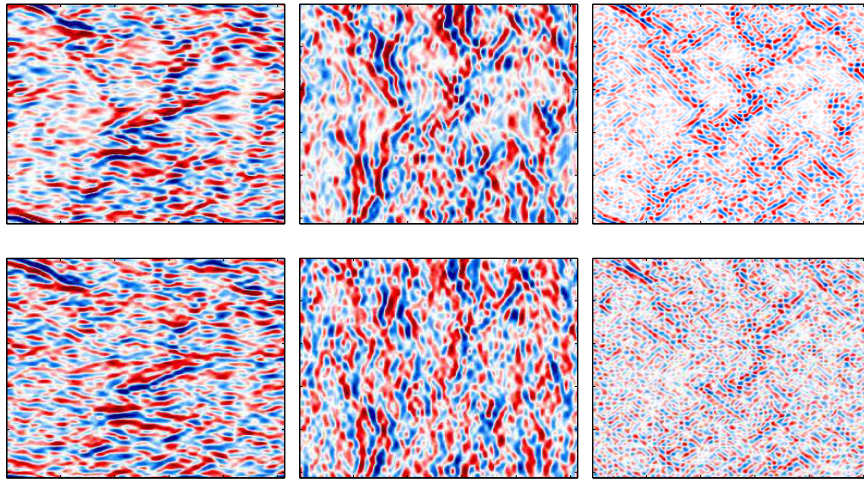


Figure 6.13: (First row) The three 'ground truth' detail subbands at Level 3 (horizontal, vertical, and diagonal, respectively). (b) The reconstructed detail subbands (Second row).

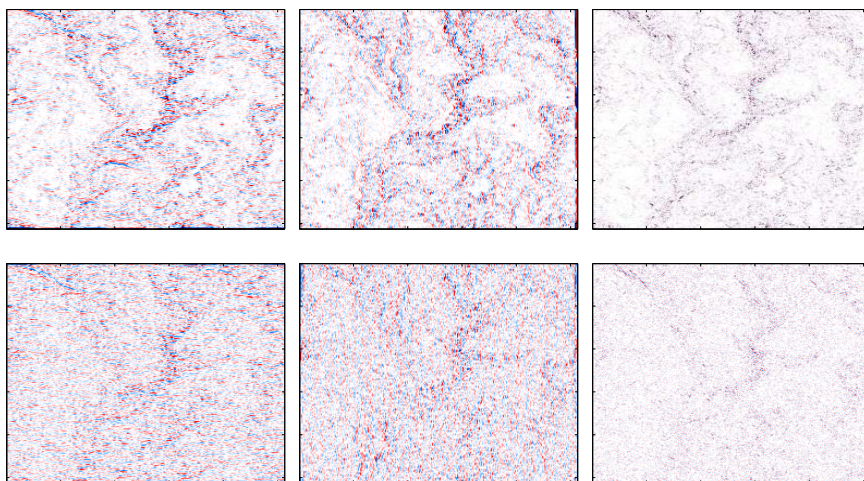


Figure 6.14: The same as Fig.6.13 for level 1.

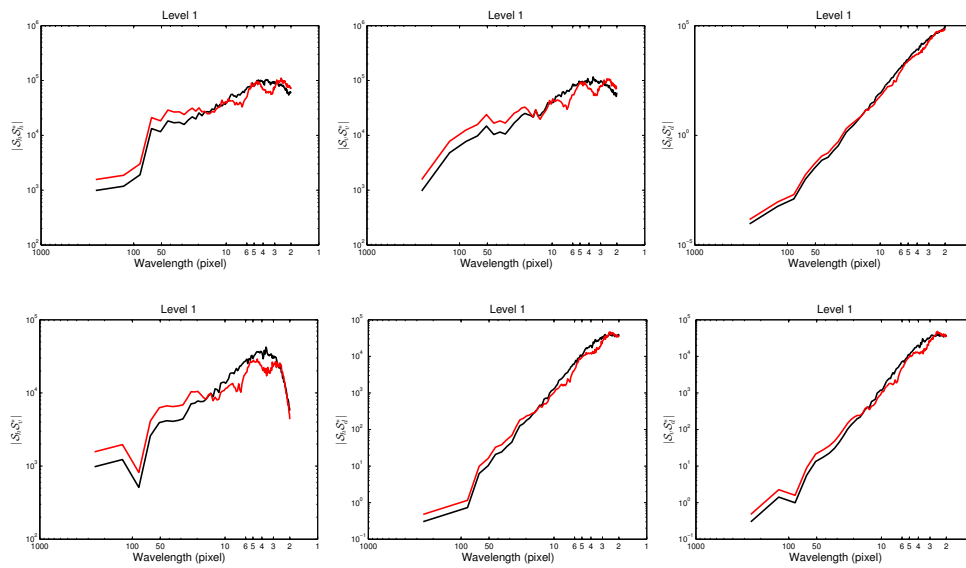


Figure 6.15: The spectra (first row) and the cross-spectra (second row) of the detail subbands at Level 1 for the original SST snapshot (black) and the reconstructed field (red).

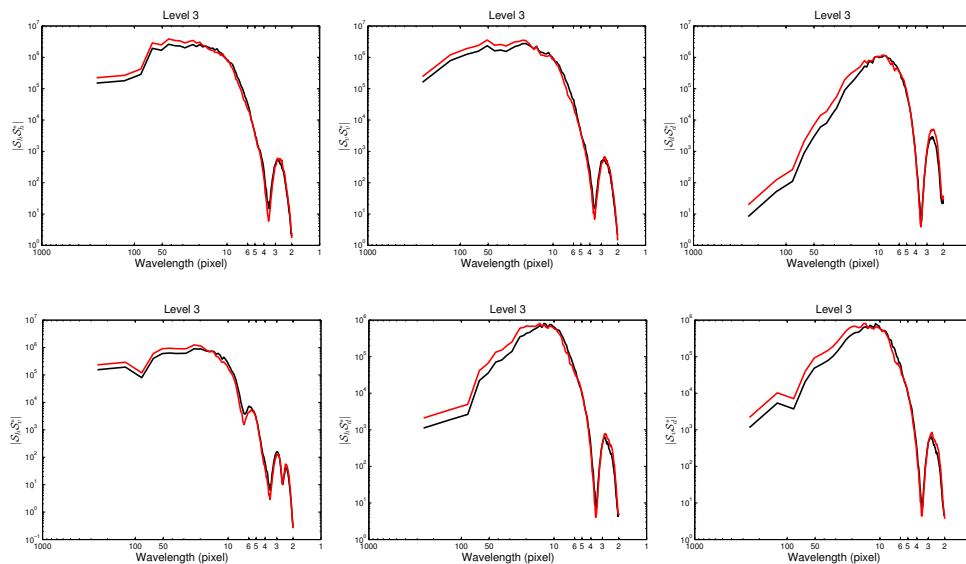


Figure 6.16: The same as Fig.6.15 for the Level 3.

scales structures. A zoomed-in comparison between the reconstructed field using our method and the original high-resolution snapshot, shown in Fig.6.11, reveals similarities in the recovered texture details.

To check whether the model is effective in terms of the reconstruction of marked fronts and gradient enhancement, we examine the obtained gradient fields. We also analyze the front enhancement capability of the model through the statistics of the magnitude gradient $|\nabla\theta|$ quantified by the probability density function (PDF). In Fig.6.10, panels (d) to (f), we compare the intensity of the SST gradients for the three fields. For the low-resolution snapshot, as expected, it is apparent that this field is considerably smoothed and the small-scale gradients are removed. Considering the intensity gradients of the reconstructed field, we observe that the production of small-scale structures and sharp edges is clearly visible. Moreover, the PDFs of SST gradients of the reconstructed snapshot are much more similar to those of the original field (see Fig.6.12(b)). This underlines the potential of the proposed technique for the reproduction of the statistical and geometrical SST fields, especially at SST fronts. We conclude the qualitative characterization of our method by giving realisations of the reconstructed wavelet sub-bands. In Fig.6.13 and Fig.6.14, the reconstructed sub-bands at level 3 (i.e., large scales) and level 1 (i.e., small-scales) from the full model is given. We report in the same figures sub-bands from the original snapshot. Thanks to the use of the phase constraint, the geometrical aspects of the reconstructed fields are satisfactory reproduced even though there are some differences at small-scale (i.e., level 1) between the ground truth and the reconstructed fields.

In order to get more quantitative characterization of the effectiveness of our method, we turn now to spectral and statistical proprieties of the reconstructions. In Fig.6.12(a) we report the radially averaged wavenumber spectrum of the reconstructed high-resolution field. In the same figure, we also show the spectra computed for the original low-resolution field. First, we clearly observe the effect of the filtering: beyond $k \simeq 30km$, the spectrum of the low-resolution field falls heavily as a result of the elimination of the small-scales, while at larger scales it is indistinguishable from the spectrum of the original high resolution image. The issue of improving resolution and reconstructing small-scale missing details allows to extend the spectrum at higher wavenumbers ($k \geq k_d$). We observe that the small-scale energetic content is widely rebuilt in the reconstruction example. The slope of the log-log spectrum is significantly closer to that obtained for the original snapshot. As already pointed out, the super-resolution scheme, formulated in the wavelet domain, allows to impose spectral and cross-spectral constraints within and between different sub-bands. In order to check this last remark, we perform a spectral analysis of the reconstructed sub-band wavelet coefficients. We compute the wavenumber power spectrum and the cross power spectrum (i.e., The Fourier transform of the cross correlation). These spectra are then averaged over all directions. In Fig.6.15 and Fig.6.16, we report, respectively, the result of such analysis using the sub-band coefficients at levels 1 and 3. In both cases, a good agreement has been found between the power spectra of the reconstructed field and those of the original high

resolution snapshot.

In order to evaluate the benefits of the various imposed spectral constraints, fig.6.17 shows the results obtained for an SST snapshot using our method and a reconstruction method based on running separate models of the form (6.8) for each sub-band component. The uni-variate model constrains the second-order statistics (i.e., power spectrum) but does not allow to produce the dependency structures (i.e., cross spectra) between different reconstructed components. In addition, there is no conditioning with respect to the low resolution observation. This makes the obtained image noisy and does not add textured small-scale details in a plausible manner. In our method, the conditioning is done through the imposed constraint on the Fourier phase of the simulated sub-bands.

We also apply our super-resolution scheme to satellite images provided by the infrared Modis instrument in the Malvinas region. Fig.6.18 compares the ground truth of an SST snapshot at the infrared resolution ($\approx 1km$) with the result of our super-resolution procedure applied to the low-resolution observation. The resolution of the original image has been artificially degraded by factor 32 (\approx resolution of micro-wave instruments). We compare the reconstruction result of the proposed approach to that of a model with no cross-spectral and phase constraints. This example further stresses the relevance of the proposed model. By looking at the intensity of gradient fields of the reconstructed field, one can see that the frontal structures are satisfactory recovered and enhanced. The benefits of the proposed approach is clear in terms of generating non-homogeneous high-structured patterns (see Fig.6.18(h)). In Fig.6.21, we show one-dimensional horizontal sections at arbitrary points.

6.7 Conclusion

In this chapter, we have presented a novel superresolution image method which exploits low-resolution temperature observations as inputs of a multivariate random field model, formulated in the wavelet domain, for the reconstruction of high-resolution images, which involve realistic small-scale structures. The prior of our model explicitly states the second order structure of the wavelet subbands coefficients. The imposed phase constraint allows us to control geometrical features of the resulting image, in terms of local regularity of frontal structures.

Our future work will particularly investigate parametric models. Regarding theoretical aspects, the major item is parameter estimation. Besides applications to the texture-based interpolation of missing data, spatio-temporal extensions of the proposed model are also of interest.

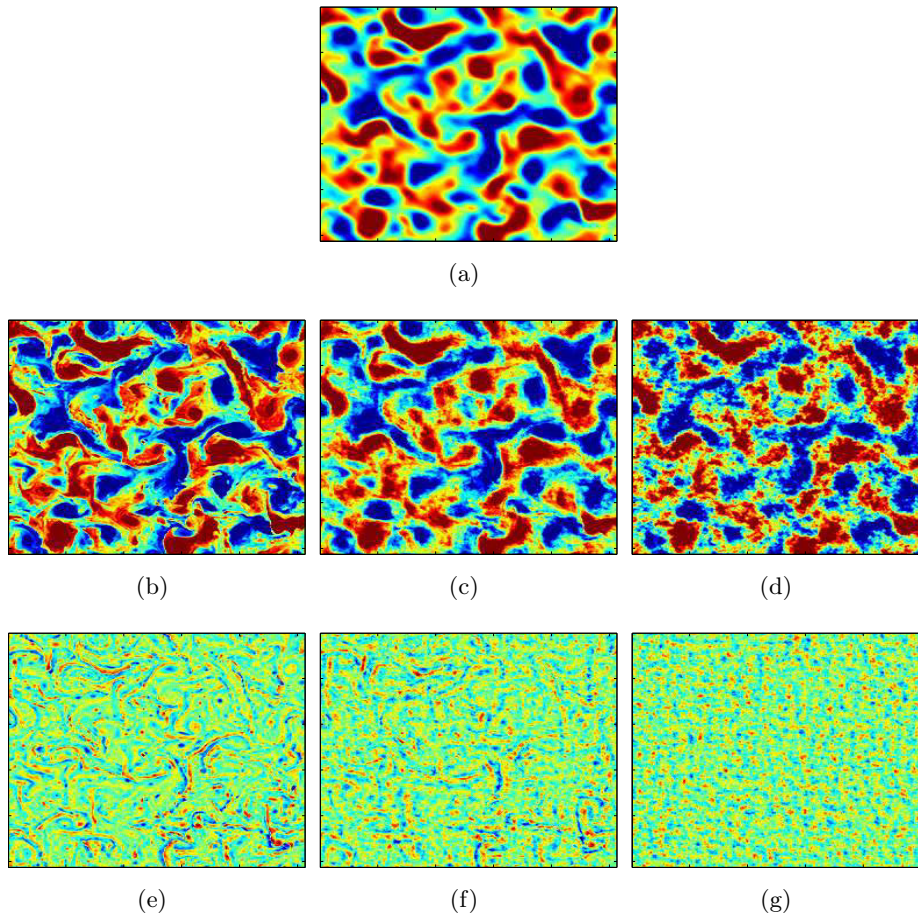


Figure 6.17: Synthesis result when dropping the cross-spectral constraints. (a) The low-resolution image, (b) the original high resolution image, (c) the constructed image using our approach and (c) the image synthesized by an independent simulation of the model (6.8) for each sub-band. (e) to (g) represent, respectively, the inter-scale component for the tree images in the middle.

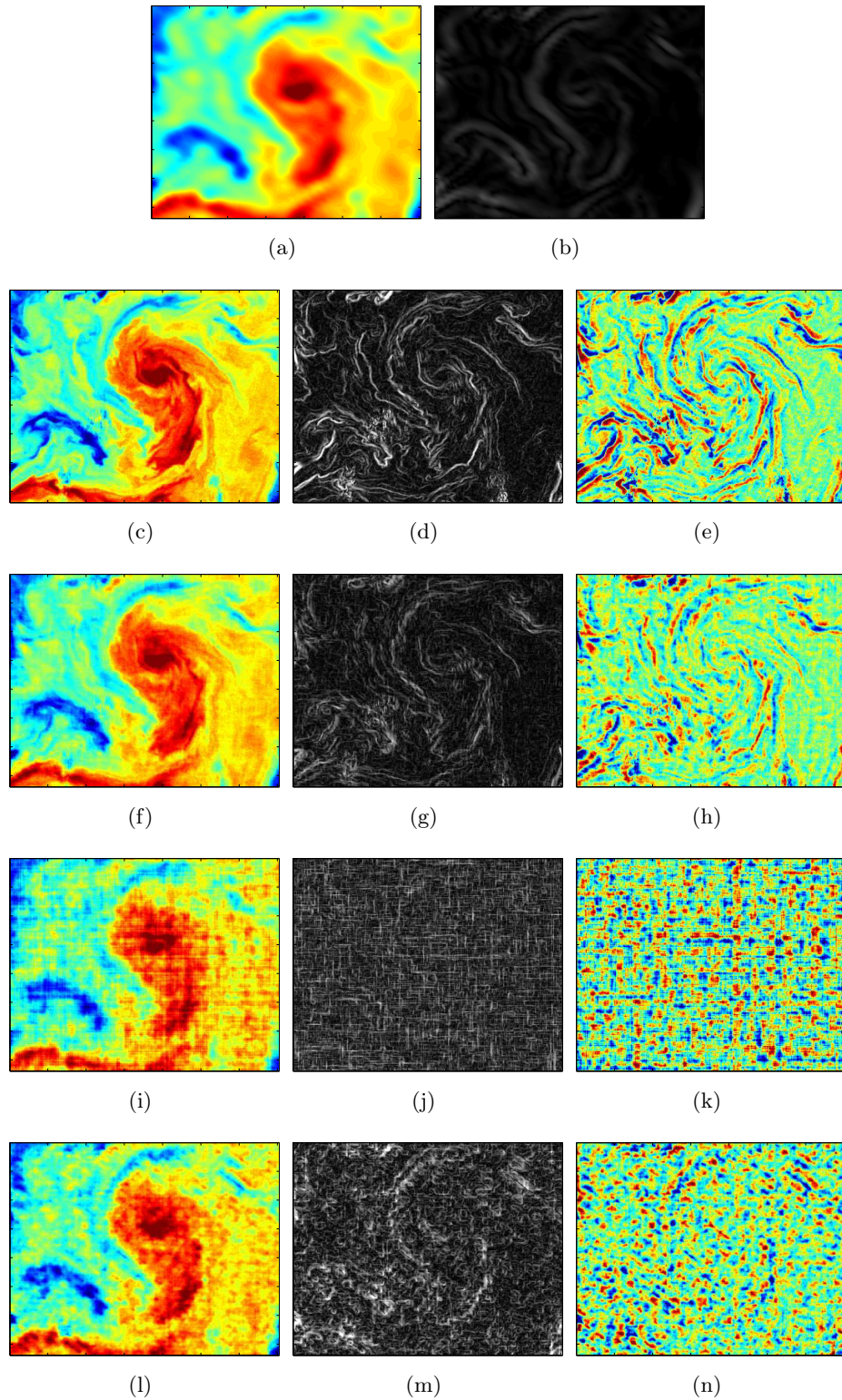


Figure 6.18: Application of our super-resolution scheme on a low-resolution satellite-based image: (a) low-resolution image and (b) the associated magnitude gradient field. Second row shows, respectively, the original high resolution image provided by Modis sensor along with the magnitude of its gradient field and the associated inter-scale component. In the same order, the third row reports the result obtained using our method. Results obtained with the uncorrelated stationary Gaussian model for the wavelet sub-bands without imposing the phase constraint is shown in the fourth row.

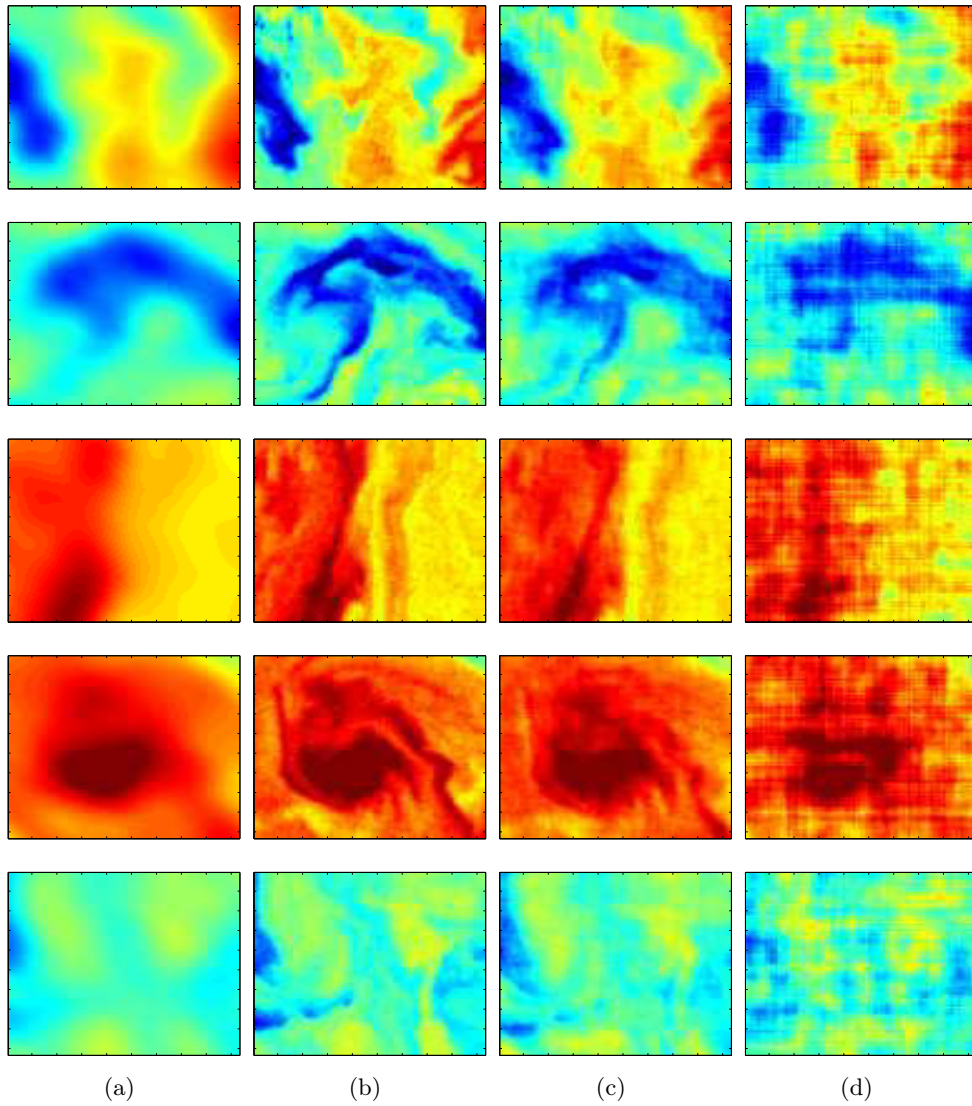
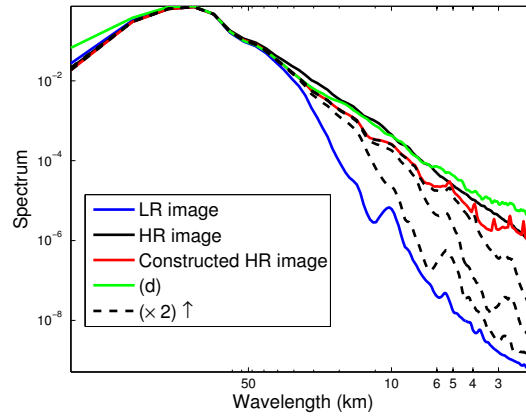


Figure 6.19: Zoomed-in comparisons of the results obtained in 6.18 (a) LR patch, (b) original high resolution patch, (c) proposed model (d) model with no cross-spectral and phase constraints (Fig.6.18(i))



(a)

Figure 6.20: Averaged Fourier power spectra estimated from images in 6.18 and from corresponding super resolved versions for various enlargement factors ranging from $\times 2$ to $\times 16$.

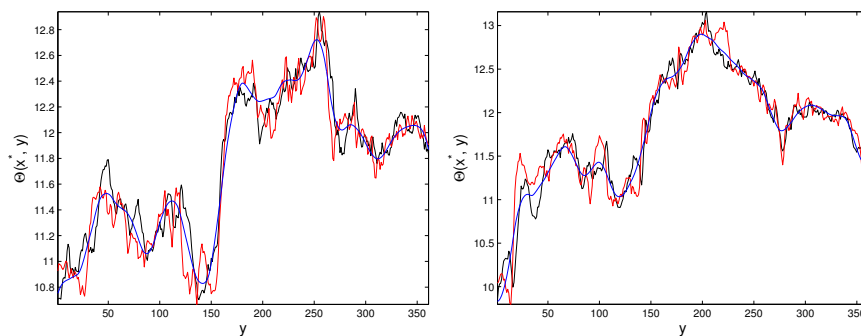


Figure 6.21: Two different line transects of images in 6.18. For interpretation of the references to color in this figure caption, the reader is referred to 6.20

Conclusion and discussion

Contents

6.1	Introduction	95
6.2	SST data and Elementary statistics	97
6.2.1	Wavelet Decomposition and Marginal Statistics	98
6.2.2	Joint Statistics of the Wavelet Coefficients: inter-scale and across-scale Dependencies	100
6.3	Multivariate texture-based models for the Wavelet Coefficients of SST images	104
6.3.1	Cascaded Gaussian random field models on Wavelet Trees	105
6.4	Super-resolution model	107
6.5	Numerical resolution	108
6.6	Results and Discussion	108
6.7	Conclusion	115

Various satellites provide images of multiple ocean parameters at different resolutions. Among all the observed parameters, Sea Surface Temperature (SST) is a peculiar example. Microwave-based radiometry provides low-resolution observation (≈ 50 km) while infrared-based instruments deliver high resolution SST measurements (≈ 1 km). In addition to their intrinsic resolution, the different satellite sensors also differ in their sensitivity to the atmospheric conditions, and especially the cloud coverage. Whereas microwave estimates of SST are unaffected by (non-precipitating) clouds and provide measurements in all weather conditions, infrared sensor may result in high missing data rates (up to 90% over several consecutive days in some regions).

In this thesis, we have focused on two problems: the reconstruction of high-resolution SST fields from low-resolution observations, and the characterization of the turbulent-related geometrical patterns exhibited by SST fields. We have proposed several textural-based super-resolution models and their multi-scale formulation. Such scale-dependent methods are expected to depict geophysically consistent features, with a view to conforming to the underlying ocean turbulence characteristics, especially: i) consistent high-resolution geometric textured patterns, ii) specific spectral signatures, iii) non-Gaussian marginal distributions.

In what follow we discuss the proposed work and give some perspectives.

- **Stochastic models for textured images**

We have proposed in this work several stochastic texture-based models and associated synthesis algorithms. In first time, we have explored the mathematical and algorithmic results of two exemplar-based texture models. The two randomization processes are the RPN and ADSN models. Both are Gaussian, homogeneous and valid for textures that does not exhibit macro-geometric patterns. The specificity of these models is to synthesize a texture sample by imposing constraints on its Fourier spectrum using random phase noise. In Part I of this thesis, we have extended the above-mentioned models to the multivariate framework. The originality of this extension is the ability to take into account additional cross-spectrum constraints. In Chapter 3, we proposed a straightforward application to sample-based super-resolution of textured images. Textures may exhibit highly-structured patterns (i.e., edges). The most defining characteristic of textures is their underlying geometry. It remain however a challenge to model and reproduce such patterns. In Chapter 2, we have not yet developed tools for handling this type of macro-geometric structures. Second-order forms (i.e., spectrum) may only be very weak constraints concerning the structure of the underlying patterns, as coherent structures essentially sign in the phase information. We then have formulated the super-resolution problem as a texture synthesis guided by the phase information of the low-resolution image. The conclusions of this Chapter are: 1) Not surprisingly, free-phase constraint model seems to provide a good results for homogeneous Gaussian micro-textures; 2) The phase constraints are needed to handle the coherent structures; 3) Unfortunately, this procedure is limited to highly unidirectional anisotropic textures and can not be directly applied to directional varying anisotropic textures, at least using the considered unsophisticated formulation. This last remark gives us the idea of considering multi-orientation analysis by decomposition of textures into components having orientation selectivity characteristics. The multiresolution wavelet framework gives us such framework. The way to handle these problems is essentially presented in Chapter 6 with an application to super-resolution of satellite-based SST snapshots.

- **Modeling fine-scale spatial variabilities of high-resolution SST fields**

In Chapter 4 in the second part of this thesis, we have addressed the characterization of the submesoscale dynamics captured by IR satellite-based SST snapshots. In this study, we used untraditional tools that have been heavily used in the context of numerical simulations of turbulent flows. We focused in particular on the analysis of the regularity of satellite-derived SST level lines in terms of the SLE analysis. It consists on mapping the (2d)curves on one dimensional signal using conformal maps that satisfy the so-called Loewner equation. The one-dimensional signal is, under the SLE hypothesis, the classical Brownian motion which is characterized by a single parameter κ called diffusivity. Curves are then classified according to the value of this parameter. We have found empirical evidence that the SST level lines may be regarded as non-homogeneous SLEs (i.e., with varying κ) unlike results found for the temperature snapshots in (numerical) SQG models or the vorticity field for the Navier-stocks equations, where the κ parameter is a constant. In Future works, we will first focus on selecting study regions so as to cover a variety of

upper ocean scenarios: western boundary currents, upwelling regions, the Mediterranean, high latitudes and equatorial. Secondly, temporal series may be considered. We can extend such studies to test their ability to capture expected mesoscale seasonal variations and evaluate the relevance of the κ statistics to perform a robust classification of ocean dynamical regimes. We will also address the extension of the proposed SLE-based analysis to other ocean tracers (e.g., salinity, chlorophyll...).

- **Reconstruction of high-resolution geophysical fields from satellite-derived observations**

In Chapter 5 of this thesis, we first deal with the pre-processing issues of the satellite data. Remote sensing images are contaminated by different type of noises. Prior to any processing or knowledge extraction using these data, all noises must be eliminated or at least reduced. In this context, we have dealt with the striping noise which is an ubiquitous phenomenon in the IR satellite-based SST. We have proposed a combined Fourier-wavelet Filtering approach. Our primary interest lies in cloudy datasets. Hence, we mainly propose an adaptation of the spectral filtering to the case of gaped data. Comparative studies are explained and experiments are carried out for different State-of-the-art methods.

In terms of application, we have developed a super-resolution technique for ocean satellite images. This work originates in particular from the observation of Sea Surface Temperature by infrared and microwave passive instruments but could have applications to other remote sensing observations. The main purpose is not to predict the true hidden fine scale information, but rather to propose a realistic prediction of this information with a focus on both gradient enhancement and small-scale oscillating patterns generation. The present approach aims at using a priori about the cross-spectral proprieties of the multi-scale level of details. In this context, the framework of the multiresolution analysis is used to handle various observed geometrical patterns at different scales. We show that the multivariate texture-based models, described in Chapter 2, combined with Fourier-phase constraints are the most able to reproduce these features across all the observable scales. Thanks to the numerical experiments we have shown that the results are visually quite satisfactory. Thanks to the phase constraints the highly-structured areas (i.e., edges) are recovered. Moreover, The expected spectral and cross-spectral proprieties are indeed quantitatively well produced. In Chapter 3, we have seen that the spatial based model is not able to reproduce well these patterns.

A lot of research work remains on. From a methodological point of view, our future work will also explore several extensions. In particular, parametric models may be considered. The SPDE equations and their multivariate extensions introduced in Chapter 2 seems to be a good candidates. Our future work will further explore this framework. Regarding theoretical aspects, we will focus on the parameter estimation methods and non-stationary formulations. The proposed super-resolution algorithms are then of key interest to address the missing data interpolation in high-resolution images given the associated low-resolution observation. The use of

the phase information in such potential application is under investigation and yet to be accomplished. The extension to spatio-temporal fields will also be of key interest. Regarding the application to ocean remote sensing data, the extension of the proposed model to the joint interpolation of two or more data sources should be investigate. Beyond the joint processing of multi-sensor data for same geophysical fields (here, SST), one could also explore the relevance of the proposed model for the joint analysis of different geophysical fields for which a mutual conditioning might be expected, but difficult to explicit model. The joint interpolation of SST and ocean colour data may provide a typical example, where could expect to benefit from multi-sensor SST data to constrain the interpolation of ocean colour data, which often involve very large missing data rate in temperate areas.

Bibliography

- [1] C. G. Kaufman, M. J. Schervish, and D. W. Nychka, “Covariance tapering for likelihood-based estimation in large spatial data sets,” Journal of the American Statistical Association, vol. 103, no. 484, pp. 1545–1555, 2008. (Cited on pages iii and 23.)
- [2] B. Galerne, Y. Gousseau, and J.-M. Morel, “Random phase textures: Theory and synthesis,” Image Processing, IEEE Transactions on, vol. 20, no. 1, pp. 257–267, 2011. (Cited on pages iv, 6, 22, 24, 30, 31, 32, 33, 35, 50, 51, 52, 54, 97 and 106.)
- [3] S. Sheffield, “Gaussian free fields for mathematicians,” Probability Theory and Related Fields, vol. 139, no. 3, pp. 521–541, 2007. [Online]. Available: <http://dx.doi.org/10.1007/s00440-006-0050-1> (Cited on pages v and 67.)
- [4] B. Münch, P. Trtik, F. Marone, and M. Stampanoni, “Stripe and ring artifact removal with combined wavelet—fourier filtering,” Opt. Express, vol. 17, no. 10, pp. 8567–8591, May 2009. [Online]. Available: <http://www.opticsexpress.org/abstract.cfm?URI=oe-17-10-8567> (Cited on pages vi, 5, 6, 76, 77, 78, 84, 86, 87 and 90.)
- [5] M. Bouali and A. Ignatov, “Adaptive reduction of striping for improved sea surface temperature imagery from suomi national polar-orbiting partnership (s-npp) visible infrared imaging radiometer suite (viirs),” Journal of Atmospheric and Oceanic Technology, vol. 31, no. 1, pp. 150–163, 2014. (Cited on pages vi, vii, 76, 77, 86, 87, 88 and 90.)
- [6] R. Srinivasan, M. Cannon, and J. White, “Landsat data destriping using power spectral filtering,” Optical Engineering, vol. 27, no. 11, pp. 271 193–271 193–, 1988. [Online]. Available: <http://dx.doi.org/10.1117/12.7976791> (Cited on pages 5 and 76.)
- [7] R. E. Crippen, “A simple spatial filtering routine for the cosmetic removal of scan-line noise from landsat tm p-tape imagery,” Photogramm. Eng. Reote Sens., vol. 55, pp. 327–331, 1989. (Cited on pages 5 and 76.)
- [8] J.-J. PAN and C.-I. CHANG, “Destriping of landsat mss images by filtering techniques,” Photogrammetric engineering and remote sensing, vol. 58, no. 10, pp. 1417–1423, 1992. (Cited on pages 5 and 76.)
- [9] J. J. Simpson, J. I. Gobat, and R. Frouin, “Improved destriping of {GOES} images using finite impulse response filters,” Remote Sensing of Environment, vol. 52, no. 1, pp. 15 – 35, 1995. [Online]. Available: <http://www.sciencedirect.com/science/article/pii/0034425794000782> (Cited on pages 5 and 76.)

- [10] J. Chen, Y. Shao, H. Guo, W. Wang, and B. Zhu, “Destriping CMODIS data by power filtering,” IEEE Transactions on Geoscience and Remote Sensing, vol. 41, pp. 2119–2124, 2003. (Cited on pages 5, 76 and 77.)
- [11] S. Mallat, A Wavelet Tour of Signal Processing, Third Edition: The Sparse Way, 3rd ed. Academic Press, 2008. (Cited on pages 5, 78, 98, 104 and 105.)
- [12] J. Torres and S. O. Infante, “Wavelet analysis for the elimination of striping noise in satellite images,” Optical Engineering, vol. 40, no. 7, pp. 1309–1314, 2001. [Online]. Available: <http://dx.doi.org/10.1117/1.1383996> (Cited on pages 5 and 76.)
- [13] O. Schramm, “Scaling limits of loop-erased random walks and uniform spanning trees,” Isr. J. Math., vol. 118, pp. 221–288, 2000. (Cited on pages 11 and 63.)
- [14] I. A. Gruzberg, “Stochastic geometry of critical curves, schramm–loewner evolutions and conformal field theory,” Journal of Physics A: Mathematical and General, vol. 39, no. 41, p. 12601, 2006. (Cited on page 12.)
- [15] D. Bernard, G. Boffetta, A. Celani, and G. Falkovich, “Inverse turbulent cascades and conformally invariant curves,” Physical review letters, vol. 98, no. 2, p. 024501, 2007. (Cited on pages 13, 21, 63, 67, 72 and 73.)
- [16] P. Klein, B. L. Hua, G. Lapeyre, X. Capet, S. Le Gentil, and H. Sasaki, “Upper ocean turbulence from high-resolution 3d simulations,” Journal of Physical Oceanography, vol. 38, no. 8, pp. 1748–1763, 2008. (Cited on page 17.)
- [17] A. Bertrand, D. Grados, F. Colas, X. Capet, A. Mousseigne, R. Fablet, A. Chaigneau, and S. Bertrand, “Broad impacts of fine-scale dynamics on seascape structure from zooplankton to seabirds,” Nature communications, vol. 5, pp. Art.nÂ°5239–, Oct 2014, publiÃ© en ligne 15 octobre 2014. (Cited on page 17.)
- [18] X. Capet, J. C. McWilliams, M. J. Molemaker, and A. F. Shchepetkin, “Mesoscale to submesoscale transition in the california current system. part i: Flow structure, eddy flux, and observational tests,” Journal of Physical Oceanography, vol. 38, no. 1, pp. 29–43, 2008. [Online]. Available: <http://dx.doi.org/10.1175/2007JPO3671.1> (Cited on page 17.)
- [19] S. R. Keating and K. S. Smith, “Upper ocean flow statistics estimated from superresolved sea-surface temperature images,” Journal of Geophysical Research: Oceans, vol. 120, no. 2, pp. 1197–1214, 2015. [Online]. Available: <http://dx.doi.org/10.1002/2014JC010357> (Cited on page 17.)
- [20] O. Yelekci, G. Charria, D. Mawren, X. Capet, G. Reverdin, F. Gohin, J. Sudre, and H. Yahia, “Observing submesoscale activity in the bay of biscay with satellite-derived sst and chlorophyll concentration,” in European Geosciences Union General Assembly 2014, 2014. (Cited on page 18.)

- [21] F. J. Wentz, C. Gentemann, D. Smith, and D. Chelton, "Satellite measurements of sea surface temperature through clouds," Science, vol. 288, no. 5467, pp. 847–850, 2000. [Online]. Available: <http://www.sciencemag.org/content/288/5467/847.abstract> (Cited on page 18.)
- [22] M. Lévy, R. Ferrari, P. J. Franks, A. P. Martin, and P. Rivière, "Bringing physics to life at the submesoscale," Geophysical Research Letters, vol. 39, no. 14, 2012. (Cited on page 21.)
- [23] F. Lindgren, H. Rue, and J. Lindström, "An explicit link between gaussian fields and gaussian markov random fields: the stochastic partial differential equation approach," Journal of the Royal Statistical Society: Series B (Statistical Methodology), vol. 73, no. 4, pp. 423–498, 2011. (Cited on page 23.)
- [24] D. Bolin and F. Lindgren, "Spatial models generated by nested stochastic partial differential equations, with an application to global ozone mapping," The Annals of Applied Statistics, vol. 5, no. 1, pp. 523–550, 2011. (Cited on page 23.)
- [25] G.-A. Fuglstad, F. Lindgren, D. Simpson, and H. Rue, "Exploring a new class of non-stationary spatial gaussian random fields with varying local anisotropy," arXiv preprint arXiv:1304.6949, 2013. (Cited on page 23.)
- [26] D. Bolin, "Spatial matérn fields driven by non-gaussian noise," Scandinavian Journal of Statistics, vol. 41, no. 3, pp. 557–579, 2014. (Cited on page 23.)
- [27] X. Hu, D. Simpson, F. Lindgren, and H. Rue, "Multivariate gaussian random fields using systems of stochastic partial differential equations," arXiv preprint arXiv:1307.1379, 2013. (Cited on pages 23, 35 and 47.)
- [28] B. Boussidi, R. Fablet, B. Chapron, and E. Autret, "Stochastic super-resolution of satellite-based sea surface temperature using conditional spde models," in 2014 IEEE Geoscience and Remote Sensing Symposium, July 2014, pp. 3077–3080. (Cited on pages 23 and 47.)
- [29] A. V. Oppenheim and J. S. Lim, "The Importance of Phase in Signals," Proceedings of the IEEE, vol. 69, no. 5, pp. 529–541, May 1981. (Cited on pages 24, 52 and 100.)
- [30] A. Materka, M. Strzelecki et al., "Texture analysis methods—a review," Technical university of lodz, institute of electronics, COST B11 report, Brussels, pp. 9–11, 1998. (Cited on page 30.)
- [31] L.-Y. Wei, S. Lefebvre, V. Kwatra, and G. Turk, "State of the art in example-based texture synthesis," in Eurographics 2009, State of the Art Report, EG-STAR. Eurographics Association, 2009, pp. 93–117. (Cited on page 30.)
- [32] A. A. Efros and T. K. Leung, "Texture synthesis by non-parametric sampling," in IEEE International Conference on Computer Vision (ICCV), 1999, vol. 2. Ieee, 1999, pp. 1033–1038. (Cited on page 30.)

- [33] G. Gimel farb, Image textures and Gibbs random fields. (Cited on page 30.)
- [34] S. C. Zhu, Y. Wu, and D. Mumford, “Filters, random fields and maximum entropy (frame): Towards a unified theory for texture modeling,” International Journal of Computer Vision, vol. 27, no. 2, pp. 107–126, 1998. (Cited on page 30.)
- [35] D. J. Heeger and J. R. Bergen, “Pyramid-based texture analysis/synthesis,” in Proceedings of the 22Nd Annual Conference on Computer Graphics and Interactive Techniques, ser. SIGGRAPH '95. New York, NY, USA: ACM, 1995, pp. 229–238. [Online]. Available: <http://doi.acm.org/10.1145/218380.218446> (Cited on page 30.)
- [36] A. A. Efros and W. T. Freeman, “Image quilting for texture synthesis and transfer,” in Proceedings of the 28th annual conference on Computer graphics and interactive techniques. ACM, 2001, pp. 341–346. (Cited on page 30.)
- [37] R. Fablet and F. Rousseau, “Missing data super-resolution using non-local and statistical priors,” in Image Processing (ICIP), 2015 IEEE International Conference on. IEEE, 2015, pp. 676–680. (Cited on pages 30 and 31.)
- [38] L. Lorenzi, F. Melgani, and G. Mercier, “Inpainting strategies for reconstruction of missing data in vhr images,” IEEE Geoscience and Remote Sensing Letters, vol. 8, no. 5, pp. 914–918, Sept 2011. (Cited on page 30.)
- [39] G. R. Cross and A. K. Jain, “Markov random field texture models,” IEEE Trans. Pattern Anal. Mach. Intell., vol. 5, no. 1, pp. 25–39, Jan. 1983. [Online]. Available: <http://dx.doi.org/10.1109/TPAMI.1983.4767341> (Cited on page 30.)
- [40] G. Tartavel, Y. Gousseau, and G. Peyré, “Variational texture synthesis with sparsity and spectrum constraints,” Journal of Mathematical Imaging and Vision, vol. 52, no. 1, pp. 124–144, 2015. [Online]. Available: <http://dx.doi.org/10.1007/s10851-014-0547-7> (Cited on page 31.)
- [41] L. A. Gatys, A. S. Ecker, and M. Bethge, “Texture synthesis using convolutional neural networks,” in Advances in Neural Information Processing Systems 28, May 2015. [Online]. Available: <http://arxiv.org/abs/1505.07376> (Cited on page 31.)
- [42] J. Rice, “On generalized shot noise,” Advances in Applied Probability, vol. 9, no. 3, pp. 553–565, 1977. [Online]. Available: <http://www.jstor.org/stable/1426114> (Cited on page 31.)
- [43] V. S. Lothar Heinrich, “Normal convergence of multidimensional shot noise and rates of this convergence,” Advances in Applied Probability, vol. 17, no. 4, pp. 709–730, 1985. [Online]. Available: <http://www.jstor.org/stable/1427084> (Cited on page 32.)

- [44] J. J. van Wijk, "Spot noise texture synthesis for data visualization," SIGGRAPH Comput. Graph., vol. 25, no. 4, pp. 309–318, Jul. 1991. [Online]. Available: <http://doi.acm.org/10.1145/127719.122751> (Cited on page 33.)
- [45] J.-P. Lewis, "Texture synthesis for digital painting," in Proceedings of the 11th Annual Conference on Computer Graphics and Interactive Techniques, ser. SIGGRAPH '84. New York, NY, USA: ACM, 1984, pp. 245–252. [Online]. Available: <http://doi.acm.org/10.1145/800031.808605> (Cited on page 33.)
- [46] A. Desolneux, L. Moisan, and S. Ronsin, "A compact representation of random phase and gaussian textures," in Acoustics, Speech and Signal Processing (ICASSP), 2012 IEEE International Conference on. IEEE, 2012, pp. 1381–1384. (Cited on page 35.)
- [47] B. Galerne, A. Leclaire, L. Moisan et al., "A texton for fast and flexible gaussian texture synthesis," 2014. (Cited on page 35.)
- [48] T. G. Peter Guttorp, "Studies in the history of probability and statistics xlix on the matÅ©rn correlation family," Biometrika, vol. 93, no. 4, pp. 989–995, 2006. [Online]. Available: <http://www.jstor.org/stable/20441340> (Cited on page 44.)
- [49] P. WHITTLE, "On stationary processes in the plane," Biometrika, vol. 41, no. 3-4, pp. 434–449, 1954. [Online]. Available: <http://biomet.oxfordjournals.org/content/41/3-4/434.short> (Cited on page 44.)
- [50] S. G. Samko, A. A. Kilbas, O. I. Marichev et al., "Fractional integrals and derivatives," Theory and Applications, Gordon and Breach, Yverdon, vol. 1993, 1993. (Cited on pages 44 and 45.)
- [51] A. Chorti and D. T. Hristopulos, "Nonparametric identification of anisotropic (elliptic) correlations in spatially distributed data sets," IEEE Transactions on Signal Processing, vol. 56, no. 10, pp. 4738–4751, Oct 2008. (Cited on page 45.)
- [52] P. Swerling, "Statistical properties of the contours of random surfaces," IRE Transactions on Information Theory, vol. 8, no. 4, pp. 315–321, 1962. (Cited on page 46.)
- [53] D. Glasner, S. Bagon, and M. Irani, "Super-resolution from a single image," in Computer Vision, 2009 IEEE 12th International Conference on, Sept 2009, pp. 349–356. (Cited on page 50.)
- [54] W. Freeman, T. Jones, and E. Pasztor, "Example-based super-resolution," Computer Graphics and Applications, IEEE, vol. 22, no. 2, pp. 56–65, Mar 2002. (Cited on page 50.)
- [55] J. Sun, J. Sun, Z. Xu, and H.-Y. Shum, "Image super-resolution using gradient profile prior," in Computer Vision and Pattern Recognition, 2008. CVPR 2008. IEEE Conference on, June 2008, pp. 1–8. (Cited on page 50.)

- [56] X. Li and M. T. Orchard, "New edge-directed interpolation," IEEE transactions on image processing, vol. 10, no. 10, pp. 1521–1527, 2001. (Cited on page 50.)
- [57] R. Fattal, "Image upsampling via imposed edge statistics," in ACM Transactions on Graphics (TOG), vol. 26, no. 3. ACM, 2007, p. 95. (Cited on page 50.)
- [58] P. Chainais, E. Koenig, V. Delouille, and J.-F. Hochedez, "Virtual super resolution of scale invariant textured images using multifractal stochastic processes," Journal of Mathematical Imaging and Vision, vol. 39, no. 1, pp. 28–44, 2011. [Online]. Available: <http://dx.doi.org/10.1007/s10851-010-0222-6> (Cited on page 50.)
- [59] J. Barral and B. B. Mandelbrot, "Multifractal products of cylindrical pulses," Probability Theory and Related Fields, vol. 124, no. 3, pp. 409–430, 2002. (Cited on page 50.)
- [60] L. Moisan, "Periodic plus smooth image decomposition," Journal of Mathematical Imaging and Vision, vol. 39, no. 2, pp. 161–179, 2011. [Online]. Available: <http://dx.doi.org/10.1007/s10851-010-0227-1> (Cited on page 52.)
- [61] I. Zachevsky and Y. Y. Zeevi, "On the statistics of natural stochastic textures and their application in image processing," in 2014 IEEE International Conference on Acoustics, Speech and Signal Processing (ICASSP). IEEE, 2014, pp. 5829–5833. (Cited on page 52.)
- [62] P. Stoica and R. L. Moses, Introduction to spectral analysis. Prentice hall Upper Saddle River, 1997, vol. 1. (Cited on page 53.)
- [63] L. Moisan, "Periodic plus smooth image decomposition," Journal of Mathematical Imaging and Vision, vol. 39, no. 2, pp. 161–179, 2011. (Cited on page 53.)
- [64] R. Fablet, B. Boussidi, E. Autret, and B. Chapron, "Random walk models for geometry-driven image super-resolution," in Acoustics, Speech and Signal Processing (ICASSP), 2013 IEEE International Conference on, May 2013, pp. 2207–2211. (Cited on page 54.)
- [65] G. Mallat, "A theory for multiresolution signal decomposition : the wavelet representation," IEEE Transaction on Pattern Analysis and Machine Intelligence, 1989. (Cited on page 58.)
- [66] M. Lesieur, "Satellite-sensed turbulent ocean structure," nature, vol. 294, p. 673, 1981. (Cited on page 62.)
- [67] I. M. Held, R. T. Pierrehumbert, S. T. Garner, and K. L. Swanson, "Surface quasi-geostrophic dynamics," Journal of Fluid Mechanics, vol. 282, pp. 1–20, 1995. (Cited on page 62.)

- [68] W. Krauss, R. Doscher, A. Lehmann, and T. Viehoff, "On eddy scales in the eastern and northern north atlantic ocean as a function of latitude," Journal of Geophysical Research: Oceans, vol. 95, no. C10, pp. 18 049–18 056, 1990. [Online]. Available: <http://dx.doi.org/10.1029/JC095iC10p18049> (Cited on page 62.)
- [69] L. Armi and P. Flament, "Cautionary remarks on the spectral interpretation of turbulent flows," Journal of Geophysical Research: Oceans, vol. 90, no. C6, pp. 11 779–11 782, 1985. [Online]. Available: <http://dx.doi.org/10.1029/JC090iC06p11779> (Cited on page 62.)
- [70] J.-L. Thiffeault, "Stretching and curvature of material lines in chaotic flows," Physica D: Nonlinear Phenomena, vol. 198, no. 3, pp. 169–181, 2004. (Cited on page 62.)
- [71] S. O. Ba, E. Autret, B. Chapron, and R. Fablet, "Statistical descriptors of ocean regimes from the geometric regularity of sst observations," IEEE Geoscience and Remote Sensing Letters, vol. 9, no. 5, pp. 851–855, Sept 2012. (Cited on pages 62 and 72.)
- [72] J. Storey, M. Choate, and D. Moe, "Landsat 8 thermal infrared sensor geometric characterization and calibration," Remote Sensing, vol. 6, no. 11, p. 11153, 2014. [Online]. Available: <http://www.mdpi.com/2072-4292/6/11/11153> (Cited on page 63.)
- [73] G. Boffetta, D. Bernard, A. Celani, and G. Falkovich, "Conformal invariance in two-dimensional turbulence," in Advances in Turbulence XI. Springer Berlin Heidelberg, 2007, pp. 164–166. (Cited on pages 63 and 70.)
- [74] M. Vucelja, G. Falkovich, and K. Turitsyn, "Fractal contours of scalar in smooth flows," in APS March Meeting Abstracts, vol. 1, 2012, p. 1334. (Cited on page 63.)
- [75] B. Duplantier and H. Saleur, "Winding-angle distributions of two-dimensional self-avoiding walks from conformal invariance," Physical review letters, vol. 60, no. 23, p. 2343, 1988. (Cited on page 65.)
- [76] V. Beffara, "The dimension of the sle curves," The Annals of Probability, pp. 1421–1452, 2008. (Cited on page 65.)
- [77] T. Kennedy, "Numerical computations for the schramm-loewner evolution," Journal of Statistical Physics, vol. 137, no. 5, pp. 839–856, 2009. (Cited on pages 66 and 72.)
- [78] O. Schramm and S. Sheffield, "Contour lines of the two-dimensional discrete gaussian free field," Acta mathematica, vol. 202, no. 1, p. 21, 2009. (Cited on page 66.)

- [79] M. Storath, A. Weinmann, and L. Demaret, “Jump-sparse and sparse recovery using potts functionals,” IEEE Trans. Signal Processing, vol. 62, no. 14, pp. 3654–3666, 2014. [Online]. Available: <http://dx.doi.org/10.1109/TSP.2014.2329263> (Cited on page 70.)
- [80] D. Chae, P. Constantin, and J. Wu, “Deformation and symmetry in the inviscid sqg and the 3d euler equations,” Journal of nonlinear science, vol. 22, no. 5, pp. 665–688, 2012. (Cited on page 73.)
- [81] J. J. Simpson and S. R. Yhann, “Reduction of noise in avhrr channel 3 data with minimum distortion,” IEEE Transactions on Geoscience and Remote Sensing, vol. 32, no. 2, pp. 315–328, Mar 1994. (Cited on page 76.)
- [82] M. Bouali and S. Ladjal, “Toward optimal destriping of modis data using a uni-directional variational model,” IEEE Transactions on Geoscience and Remote Sensing, vol. 49, no. 8, pp. 2924–2935, Aug 2011. (Cited on page 76.)
- [83] M. Bouali and A. Ignatov, “A comparative study of stripe noise on modis and viirs thermal emissive bands,” pp. 85 1000–85 1000–13, 2012. [Online]. Available: <http://dx.doi.org/10.1117/12.928864> (Cited on page 76.)
- [84] C.-B. Schonlieb, Partial Differential Equation Methods for Image Inpainting. Cambridge University Press, November 2015. (Cited on page 81.)
- [85] J.-F. Cayula and P. Cornillon, “Edge detection algorithm for sst images,” Journal of Atmospheric and Oceanic Technology, vol. 9, no. 1, pp. 67–80, 1992. (Cited on page 87.)
- [86] D. B. Chelton and F. J. Wentz, “Global microwave satellite observations of sea surface temperature for numerical weather prediction and climate research,” Bulletin of the American Meteorological Society, vol. 86, no. 8, p. 1097, 2005. (Cited on page 96.)
- [87] E. Autret, “Analyse des champs de température de surface de la mer à partir des observations satellite multi-source,” Ph.D. dissertation, TelecomBretagne, 2014. (Cited on page 98.)
- [88] P. Tandeo, E. Autret, B. Chapron, R. Fablet, and R. Garrello, “Sst spatial anisotropic covariances from metop-avhrr data,” Remote Sensing of Environment, vol. 141, pp. 144–148, 2014. (Cited on page 98.)
- [89] Z.-S. She, “Intermittency and non-gaussian statistics in turbulence,” Fluid Dynamics Research, vol. 8, no. 1-4, p. 143, 1991. [Online]. Available: <http://iopscience.iop.org/1873-7005/8/1-4/A14> (Cited on page 98.)
- [90] A. Srivastava, A. Lee, E. Simoncelli, and S.-C. Zhu, “On advances in statistical modeling of natural images,” Journal of Mathematical Imaging and Vision, vol. 18, no. 1, pp. 17–33, 2003. [Online]. Available: <http://dx.doi.org/10.1023/A:1021889010444> (Cited on page 98.)

-
- [91] A. S. Lewis and G. Knowles, "Image compression using the 2-d wavelet transform," IEEE Transactions on Image Processing, vol. 1, no. 2, pp. 244–250, Apr 1992. (Cited on page 98.)
- [92] E. P. Simoncelli and J. Portilla, "Texture characterization via joint statistics of wavelet coefficient magnitudes," in Image Processing, 1998. ICIP 98. Proceedings. 1998 International Conference on, vol. 1. IEEE, 1998, pp. 62–66. (Cited on page 98.)
- [93] M. Farge, "Wavelet transforms and their applications to turbulence," Annual Review of Fluid Mechanics, vol. 24, no. 1, pp. 395–458, 1992. [Online]. Available: <http://dx.doi.org/10.1146/annurev.fl.24.010192.002143> (Cited on page 98.)
- [94] I. Daubechies, Ten Lectures on Wavelets. Philadelphia, PA, USA: Society for Industrial and Applied Mathematics, 1992. (Cited on page 104.)
- [95] J. Larsen, "Correlation functions and power spectra," Section for Cognitive Systems, Informatics and Mathematical Modelling, Technical University of Denmark, 2009. (Cited on page 108.)
- [96] W. H. Press, B. P. Flannery, S. A. Teukolsky, W. T. Vetterling, and P. B. Kramer, "Numerical recipes: the art of scientific computing," 1987. (Cited on page 108.)

Résumé

La caractérisation des dynamiques de sous-mésoéchelle (<10km) à la surface de l'océan et leurs impacts sur les processus océaniques globaux sont des enjeux scientifiques majeurs. L'imagerie satellitaire est un outil essentiel dans ce contexte, qui présente toutefois des limitations liées aux instruments de télédétection. Dans le cas des images de température de surface des océans (SST), les mesures satellitaires des structures océaniques sont limitées par la résolution grossière des capteurs micro-ondes (~50km) d'une part, et par la sensibilité aux conditions climatiques (e.g., couverture nuageuse) des instruments de mesure infrarouge haute-résolution. Dans cette thèse, nous nous intéressons à l'analyse, la modélisation et la reconstruction des structures turbulentes haute-résolution capturées par imagerie satellitaire de SST, et proposons quatre contributions principales. Dans un premier temps, nous développons une méthode de filtrage conjointe Fourier-ondelettes pour le prétraitement d'artefacts géométriques dans les observations satellitaires infrarouges. Dans un deuxième temps, nous nous focalisons sur la caractérisation de la variabilité géométrique de champs de température de surface (SST) en utilisant des modèles de marches aléatoires appliqués aux lignes de niveaux. En particulier, nous considérons des processus aléatoires de type schramm Loewner (SLE). Nous nous intéressons ensuite à la modélisation stochastique des variabilités inter-échelles de champs de SST. Des modèles stochastiques de textures multivariées sont introduits. Ces modèles permettent de reproduire des propriétés statistiques et spectrales similaires à celles des données ayant servi à les calibrer. Nous développons ensuite des méthodes de super-résolution de champs de SST conditionnellement à une observation basse-résolution. Nous utilisons des modèles multivariés de textures formulés dans le domaine des ondelettes, en exploitant l'apprentissage d'à priori statistiques (i.e., covariances et covariances croisées) des différentes sous-bandes à partir d'images haute-résolution. Des contraintes supplémentaires imposées sur la phase de Fourier des différentes sous-bandes simulées permettent la reconstruction de structures géométriques marquées tels que les fronts. Nous démontrons la pertinence de la méthode proposée sur des images satellitaires de SST obtenues à partir du capteur Modis/Aqua.

Mots-clés : Télédétection des océans, Température de surface des océans, Turbulence océanique, Destriping, super-résolution, Synthèse de textures, Processus SLE

Abstract

The characterization of sub-mesoscale dynamics (<10 km) in the ocean surface and their impact on global ocean processes are major scientific issues. Satellite imagery is an essential tool within this framework. However, the use of remote sensing techniques still raise challenging. For instance, regarding Sea Surface Temperature (SST) images, satellite measurements of oceanic structures are limited by the coarse resolution of microwave sensors (~50km) on one hand, and by sensitivity to climatic conditions (eg., Cloud cover) of high-resolution infrared instruments on the other hand. In this thesis, we are interested in analysis, modeling and reconstruction of high-resolution turbulent structures captured by satellite SST imagery. In this context, we propose four main contributions. First, we develop a joint Fourier-Wavelet filtering method for the pre-processing of geometrical noises in satellite-based infrared observations, namely the striping noises. Secondly, we focus on the characterization of the geometric variability of sea surface temperature (SST) fields using random walk models applied to SST isolines. In particular, we consider the class of Schramm Loewner evolution curves (SLE). We then focus on the stochastic modeling of the cross-scale variabilities of SST fields. Stochastic multivariate texture-based models are introduced. These models are designed to reproduce several statistics and spectral properties that are observed on the data that are used to calibrate the model. We then develop our framework for stochastic super-resolution of SST fields conditionally to low-resolution observations. We use multivariate texture-based models formulated in the wavelet domain. These models exploit the formulation of statistical and spectral priors (i.e., covariances and cross-covariances) on wavelet subbands. These priors are directly learned from exemplar high-resolution images. Additional constraints imposed on the Fourier-phase of the different simulated subbands allow the reconstruction of coherent geometric structures such as the edge information. Our method is tested and validated using infrared high-resolution satellite SST images provided by Aqua Modis sensor.

Keywords : Ocean remote sensing, sea surface temperature, ocean turbulence, Destriping, super-resolution, Texture synthesis, SLE process.



n° d'ordre : 2016telb0404

Télécom Bretagne

Technopôle Brest-Iroise - CS 83818 - 29238 Brest Cedex 3

Tél : + 33(0) 29 00 11 11 - Fax : + 33(0) 29 00 10 00